

May 2016

Development and implementation of efficient noise suppression methods for emission computed tomography

Jiahan Zhang
Syracuse University

Follow this and additional works at: <https://surface.syr.edu/etd>



Part of the [Physical Sciences and Mathematics Commons](#)

Recommended Citation

Zhang, Jiahan, "Development and implementation of efficient noise suppression methods for emission computed tomography" (2016). *Dissertations - ALL*. 464.
<https://surface.syr.edu/etd/464>

This Dissertation is brought to you for free and open access by the SURFACE at SURFACE. It has been accepted for inclusion in Dissertations - ALL by an authorized administrator of SURFACE. For more information, please contact surface@syr.edu.

Abstract

In PET and SPECT imaging, iterative reconstruction is now widely used due to its capability of incorporating into the reconstruction process a physics model and Bayesian statistics involved in photon detection. Iterative reconstruction methods rely on regularization terms to suppress image noise and render radiotracer distribution with good image quality. The choice of regularization method substantially affects the appearances of reconstructed images, and is thus a critical aspect of the reconstruction process. Major contributions of this work include implementation and evaluation of various new regularization methods. Previously, our group developed a preconditioned alternating projection algorithm (PAPA) to optimize the emission computed tomography (ECT) objective function with the non-differentiable total variation (TV) regularizer. The algorithm was modified to optimize the proposed reconstruction objective functions.

First, two novel TV-based regularizers—high-order total variation (HOTV) and infimal convolution total variation (ICTV)—were proposed as alternative choices to the customary TV regularizer in SPECT reconstruction, to reduce “staircase” artifacts produced by TV. We have evaluated both proposed reconstruction methods (HOTV-PAPA and ICTV-PAPA), and compared them with the TV regularized reconstruction (TV-PAPA) and the clinical standard, Gaussian post-filtered, expectation-maximization reconstruction method (GPF-EM) using both Monte Carlo-simulated data and anonymized clinical data. Model-observer studies using Monte Carlo-simulated data indicate that ICTV-PAPA is able to reconstruct images with similar or better lesion detectability, compared with clinical standard GPF-EM methods, but at lower

detected count levels. This implies that switching from GPF-EM to ICTV-PAPA can reduce patient dose while maintaining image quality for diagnostic use.

Second, the ℓ_1 norm of discrete cosine transform (DCT)-induced framelet regularization was studied. We decomposed the image into high and low spatial-frequency components, and then preferentially penalized the high spatial-frequency components. The DCT-induced framelet transform of the natural radiotracer distribution image is sparse. By using this property, we were able to effectively suppress image noise without overly compromising spatial resolution or image contrast.

Finally, the fractional norm of the first-order spatial gradient was introduced as a regularizer. We implemented $\ell_{2/3}$ and $\ell_{1/2}$ norms to suppress image spatial variability. Due to the strong penalty of small differences between neighboring pixels, fractional-norm regularizers suffer from similar cartoon-like artifacts as with the TV regularizer. However, when penalty weights are properly selected, fractional-norm regularizers outperform TV in terms of noise suppression and contrast recovery.

**Development and Implementation of Efficient Noise Suppression Methods for
Emission Computed Tomography**

By

Jiahan Zhang

B.S., Nankai University, 2011

Dissertation

Submitted in partial fulfillment of the requirements for the degree of
Doctor of Philosophy in Physics.

Syracuse University

May 2016

Copyright © Jiahan Zhang 2016
All Rights Reserved

Table of Contents

Abstract	i
Table of Contents	v
List of Tables	ix
List of Figures	x
List of Acronyms	xvi
Acknowledgements	xviii
Chapter 1. Introduction	1
1.1. SPECT imaging	1
1.1.1 Anger camera.....	1
1.1.2 Tomographic imaging.....	5
1.1.3 Clinical applications and radiation dose considerations.....	5
1.2. Objectives	6
1.3. Overview of dissertation.....	7
1.4. Publications on and presentations of this dissertation work.....	7
Chapter 2. Principles of SPECT imaging	9
2.1 SPECT imaging model	9
2.1.1 Notations.....	9
2.1.2 Modeling the detection of gamma photons	11
2.1.3 System matrix A	16

2.2	Iterative image reconstruction	18	
2.2.1	Maximum-likelihood reconstruction criteria	18	
2.2.2	Maximum-likelihood expectation-maximization (ML-EM) algorithm	19	
2.2.3	Maximum <i>a posteriori</i> (MAP) reconstruction criteria	23	
2.2.4	Preconditioned alternating projection algorithm (PAPA)	24	
Chapter 3.	Experimental design	32	
3.1	Monte Carlo simulated projection data.....	32	
3.2	Characterizing collimator-detector response function using experimental data		34
3.2.1	Experimental design	34	
3.2.2	Data analysis	35	
3.3	Standard image quality metrics.....	36	
3.3.1	Spatial variability	37	
3.3.2	Uniformity	37	
3.3.3	Local NPS.....	38	
3.3.4	Spatial resolution	38	
3.3.5	Bias	39	
3.3.6	Contrast recovery coefficient.....	40	
3.3.7	Mean-squared error.....	40	
3.4	Model observers.....	40	
3.4.1	Channelized Hotelling observer	41	
3.4.2	Channel selection.....	43	
3.4.3	Internal noise	45	

3.4.4 CHO lesion detectability.....	46
-------------------------------------	----

Chapter 4. Implementation and evaluation of various regularization methods for

iterative reconstruction	47
4.1 Post filtering.....	47
4.2 Iterative regularization methods	47
4.3 Total variation-based regularization methods.....	48
4.3.1 Total variation.....	49
4.3.2 High order total variation	52
4.3.3 Infimal-convolution total variation.....	53
4.3.4 Experimental design	55
4.3.5 Results and discussion	58
4.3.6 Conclusions	76
4.4 DCT-induced framelet regularization.....	78
4.4.1 Numerical experiment results and discussion.....	80
4.4.2 Conclusions	83
4.5 Fractional norm.....	83
4.5.1 Motivation	84
4.5.2 Implementation of fractional norm regularized SPECT reconstruction	85
4.5.3 Experimental design	86
4.5.4 Results and discussion	87
4.5.5 Conclusions	93

Chapter 5. Conclusions and future work	95
Appendix A. Iteration scheme of TV-PAPA, HOTV-PAPA, and ICTV-PAPA98	
Appendix B. Protocol for CDRF-modelling experiments	102
Reference	104
VITA	114

List of Tables

Table 3.1. Resolution response (Gaussian radius) as function of point-source distance d (cm) from collimator and ρ (cm) from central axis.	36
Table 3.2. Sensitivity as function of point-source distance d (cm) from collimator and ρ (cm) from central axis.	36
Table 4.1. Regularizers TV, HOTV, and ICTV. Here ∇ represents first-order difference matrix.	54
Table 4.2. Mean and maximum amplitudes of LNPS obtained for the simulated SPECT data with 120 kc/view	69

List of Figures

Fig. 1.2. Schematic figure of an Anger camera.	2
Fig. 1.3. NaI scintillation crystal. [3].....	3
Fig. 1.4. Collimators with (a) parallel beam design and (b) fan beam design. [4]	4
Fig. 2.1. Example of 1D collimator detector response functions for point sources at two distances from the collimator.	12
Fig. 2.2. Photons emitted from patients and detected by gamma camera or absorbed by collimator. Trajectories of gamma photons are shown. (a) Photon passes through the collimator directly and is detected. (b) Photon penetrates collimator septum and is detected. (c) Photon is absorbed by collimator septum. (d) Photon is scattered once within patient body and is detected. (e) Photon is scattered once within patient body and is absorbed by collimator. (f) Photon scatters multiple times within patient body and is detected. [12].....	15
Fig. 2.3. Schematic figure of voxel j , pixel i , and system matrix element A_{ij}	17
Fig. 3.1. Sample images of phantom and Monte Carlo simulated projection data. (a) Transaxial cross-section of a digital phantom, with six spheres of various sizes (b) Monte Carlo-simulated “noiseless” projection, and (c) Simulated projection with added Poisson noise.	33
Fig. 3.2. Experiment setup for (a) Siemens e.cam dual-head camera with LEHR parallel beam collimators, and (b) Trionix Triad triple-head camera with LEHR fan beam collimators. Courtesy of SUNY Upstate University Hospital.....	35
Table 3.1. Resolution response (Gaussian radius) as function of point-source distance d (cm) from collimator and ρ (cm) from central axis.	36

Table 3.2. Sensitivity as function of point-source distance d (cm) from collimator and ρ (cm) from central axis.	36
Fig. 3.3. CHO bands in frequency domain: (a) SQR (b) S-DOG (c) D-DOG. See text for frequency selections.....	44
Fig. 4.1. Comparison of TV regularization term with Huber and quadratic regularization functions.....	51
Table 4.1. Regularizers TV, HOTV, and ICTV. Here ∇ represents first-order difference matrix.	54
Fig. 4.2. Trans-axial cross-sections of a phantom with: (a) 6 cold (no activity) piecewise-constant spheres with radii of 4, 5, 6, 7, 8, and 9 mm, (b) 8 point sources with maximum-activity-to-mean-background ratio of 100:1 at different radial distances from the central axis of the phantom, (c) 6 hot Gaussian blobs with radii (FWHM) of 4, 5, 6, 7, 8, and 9 mm with maximum-activity-to-mean-background ratio of 3:1 and (d), (e), (f) reference phantom containing warm Gaussian blobs only. Both phantoms were of the size $128 \times 128 \times 128$ voxels, with voxel size set to $2.2 \times 2.2 \times 2.2$ mm ³	56
Fig. 4.3. Transaxial cross-sections of images for Monte Carlo-simulated SPECT data for phantom shown in Fig. 4.2, reconstructed by: (a) ICTV-PAPA for 40 kc/view data, $\lambda_1 = 0.4$, $\lambda_2 = 0.4$; (b) ICTV-PAPA for 80 kc/view data, $\lambda_1 = 0.3$, $\lambda_2 = 0.3$; (c) ICTV-PAPA for 120 kc/view data, $\lambda_1 = 0.2$, $\lambda_2 = 0.2$; (d) HOTV-PAPA for 120 kc/view data, $\lambda_1 = 0.1$ $\lambda_2 = 0.1$; (e) TV-PAPA for 120 kc/view data, $\lambda = 0.2$; and (f) GPF-MLEM using 120 kc/view data, FWHM = 7.3 mm. For all images, the reconstruction was stopped at 100 iterations. Left column: hot spheres with Gaussian activity distribution (see text). Right column: cold spheres with zero activity.....	60

Fig. 4.4. Components of ICTV-PAPA reconstructed images obtained at 100 iterations for simulated SPECT data with 120 kc/view, $\lambda_1 = 0.2$, and $\lambda_2 = 0.2$: (a) f_1 component, (b) f_2 component, and (c) final combined image ($f=f_1 + f_2$). Top row: cold spheres with zero activity. Bottom row: hot spheres with Gaussian activity distribution (see Fig. 4.2 and text). 61

Fig. 4.5. Surface plots of: (a) ICTV-PAPA for 40k/view, $\lambda_1 = 0.4$ $\lambda_2 = 0.4$; (b) ICTV-PAPA for 80k/view, $\lambda_1 = 0.3$ $\lambda_2 = 0.3$; (c) ICTV-PAPA for 120k/view, $\lambda_1 = 0.2$ $\lambda_2 = 0.2$; (d) HOTV-PAPA for 120k/view, $\lambda_1 = 0.1$ $\lambda_2 = 0.1$; (e) TV-PAPA for 120k/view, $\lambda = 0.2$; (f) GPF-MLEM for 120k/view, FWHM = 7.3 mm; and (g) ground truth. Left column: hot spheres with Gaussian activity distribution (see text). Right column: cold spheres with zero activity shown in inverted scale..... 64

Fig. 4.6. (a) Mean CRC vs. background variability for hot spheres; (b) Mean CRC vs. background variability for cold spheres; (c) Mean CRC vs. bias for hot spheres; (d) Mean CRC vs. bias for cold spheres; (e) Bias vs. background variability for hot spheres; (f) Bias vs. background variability for cold spheres. Each point on the curves was calculated for penalty parameters selected in the 0.01-200 range for TV-based algorithms and Gaussian post-filter radii in the 1.1-7.1 mm range for GPF-EM. Only the four largest spheres were considered among cold spheres. The limiting background spatial variability for selected ROIs is 17.6% for the background in the cross-section with hot spheres, and 22.7% for the cross-section with cold spheres due to the lumpy background. The ideal values of background spatial variability are indicated by solid diamonds and dashed lines. 66

Fig. 4.7. Local noise power spectra (LNPS) obtained for the central location of small ROI: (a) GPF-EM; (b) TV-PAPA; (c) HOTV-PAPA; and (d) ICTV-PAPA all obtained for simulated

SPECT data with 120 kc/view. Noise variance values of the selected ROI and penalty parameters are displayed at the bottom of each image..... 68

Fig. 4.8. Average radial profiles for local noise power spectra shown in Fig. 4.7. The profiles were obtained by averaging the data every 10° 69

Table 4.2. Mean and maximum amplitudes of LNPS obtained for the simulated SPECT data with 120 kc/view..... 69

Fig. 4.9. CHO detectability indices of: (a) hot; and (b) cold spheres vs. cross-sectional area of the spheres and vs. number of counts per view in the simulated SPECT data. ICTV-PAPA for 40 kc/view data, $\lambda_1 = 0.4, \lambda_2 = 0.4$; ICTV-PAPA for 80kc/view data, $\lambda_1 = 0.3, \lambda_2 = 0.3$; ICTV-PAPA for 120kc/view data, $\lambda_1 = 0.2, \lambda_2 = 0.2$; HOTV-PAPA for 120kc/view data, $\lambda_1 = 0.1 \lambda_2 = 0.1$; TV-PAPA for 120kc/view data, $\lambda = 0.2$; and GPF-MLEM using 120kc/view data, FWHM = 7.3 mm. The reconstructions were stopped at 100 iterations. The solid lines connecting the data points are provided as a visual guide only..... 70

Fig. 4.10. CHO detectability estimated (solid circles) for the fourth largest sphere (1.4 cm^2 cross-sectional area) for images reconstructed with three photon levels (40, 80 and 120 kc/view) using ICTV-PAPA and GPF-EM (solid squares) at 120 kc/view level. 71

Fig. 4.11. (a) Radial (r) full width at half maximum (FWHM) and (b) tangential (t) FWHM of trans-axial local point spread function (LPSF) as function of radial positions of point sources. The SPECT data were simulated for 120 kc/view. Reconstructions were performed with the following penalty parameters: ICTV-PAPA for 40 kc/view data, $\lambda_1 = 0.4, \lambda_2 = 0.4$; ICTV-PAPA for 80kc/view data, $\lambda_1 = 0.3, \lambda_2 = 0.3$; ICTV-PAPA for 120kc/view data, $\lambda_1 = 0.2, \lambda_2 = 0.2$; HOTV-PAPA for 120kc/view data, $\lambda_1 = 0.1 \lambda_2 = 0.1$; TV-PAPA for 120kc/view data, $\lambda = 0.2$; and

GPF-EM using 120kc/view data, FWHM = 7.3 mm. Reconstructions were stopped at 100 iterations. The solid lines are linear regression fits..... 72

Fig. 4.12. Trans-axial views of reconstructed images obtained for clinical Tc-99m Sestamibi SPECT parathyroid, late-phase study: Clinical Hermes HOSEM algorithm (a); EM-GPF (b); TV (c, d); HOTV-PAPA (e, f); and ICTV-PAPA (g, h), each with two sets of penalty parameters.. 74

Fig. 4.13. Coronal views of reconstructed images obtained for clinical Tc-99m Sestamibi SPECT parathyroid late-phase study: Clinical Hermes HOSEM algorithm (a); EM-GPF (b); TV (c, d); HOTV-PAPA (e, f); and ICTV-PAPA (g, h), each with two sets of penalty parameters..... 75

Fig. 4.14. One-channel-wide line profiles through reconstructed transaxial images from the clinical Tc-99m Sestamibi parathyroid scan image shown in Fig. 4.12. The location of the profile is shown in the inset. Penalty weights were set as: TV-PAPA $\lambda = 2$, HOTV-PAPA $\lambda_1 = 1 \lambda_2 = 1$, ICTV-PAPA: $\lambda_1 = 2 \lambda_2 = 2$ 76

Fig. 4.15. Transaxial cross-section through the synthetic phantom with warm lumpy background and Gaussian blobs as hot lesions ($\sigma = 4, 5, 6, 7, 8,$ and 9 mm; 4:1 activity ratio)..... 80

Fig. 4.16. Transaxial cross-section through the reconstructed images with various parameters obtained at 100 iterations. Top four rows are images reconstructed using PAPA-DCT; bottom row are images reconstructed using EM with Gaussian post-filters..... 82

Fig. 4.17. Mean squared error (MSE) curves obtained for images reconstructed using proposed DCT-PAPA method and EM Gaussian post filter (GPF-EM)..... 82

Fig. 4.18. Comparison of $\varphi(z)$ for $\ell_0, \ell_{1/2}, \ell_{2/3},$ and ℓ_1 norm (TV). 84

Fig. 4.19. 2D Phantoms used for evaluation of fractional norm-regularized SPECT reconstruction methods: (a) Hoffman brain phantom, (b) Cylindrical phantom with lumpy background and hot spherical “lesions”.....	87
Fig. 4.20. Transaxial cross-section of Hoffman phantom reconstructed by PAPA with $\ell_{1/2}$ norm, $\ell_{2/3}$ norm, and ℓ_1 -norm (TV).	89
Fig. 4.21. Image profiles of the phantom and reconstructed images with optimal penalty weights. The image profiles were taken horizontally through the center of the image, as indicated by the yellow line in the figure.	90
Fig. 4.22. (a) RMSE and (b) bias of reconstructed images of the lumpy phantom with optimal penalty weights selected for each reconstruction methods.	91
Fig. 4.23. Contrast recovery coefficients of reconstructed hot spheres in the lumpy phantom with optimal penalty weights selected for each reconstruction methods.....	91
Fig. 4.24. Transaxial cross-section of Hoffman phantom reconstructed by PAPA with $\ell_{1/2}$ norm, $\ell_{2/3}$ norm, and ℓ_1 norm (TV).....	93

List of Acronyms

SPECT	<i>single photon emission computed tomography</i>
PMT	<i>photomultiplier tube</i>
LEHR	<i>low energy high resolution</i>
DRF	<i>detector response function</i>
GRF	<i>geometry response function</i>
CDRF	<i>collimator-detector response function</i>
TEW	<i>triple energy window</i>
FBP	<i>filtered backprojection</i>
ML	<i>maximum likelihood</i>
EM	<i>expectation maximization</i>
MAP	<i>maximum a posteriori</i>
PL	<i>penalized maximum likelihood</i>
PAPA	<i>preconditioned alternating projection algorithm</i>
TV	<i>total variation</i>
ICTV	<i>infimal convolution total variation</i>
HOTV	<i>high-order total variation</i>
DCT	<i>discrete cosine transform</i>
MPI	<i>message passing interface</i>
CPU	<i>central processing unit</i>
GPU	<i>graphical processing unit</i>

SNR	<i>signal-to-noise ratio</i>
FWHM	<i>full width at half maximum</i>
NPS	<i>noise power spectrum</i>
CRC	<i>contrast recovery coefficient</i>
CHO	<i>channelized Hotelling observer</i>
ROC	<i>receiver operating characteristic</i>
AUC	<i>area under the ROC curve</i>
ESF	<i>edge spread function</i>
PSF	<i>point spread function</i>
ROR	<i>radius of rotation</i>
RMSE	<i>root mean square error</i>
VOI	<i>volume of interest</i>

Acknowledgements

First of all, I would like to thank my two advisors, Dr. Edward Lipson and Dr. Andrzej Krol, for their continuous guidance and encouragement during the course of this work.

Dr. Lipson has not only given me great mentorship in my research, but also inspired me to be a better person in life. Dr. Krol has worked with me on daily basis in the past few years, and his experience and leadership are indispensable to our work. I would also like to express my appreciation for Dr. Yuesheng Xu and Dr. Lixin Shen for their mathematics expertise and creativity, which inspired our research projects.

Thank you to my friends and colleagues for their tremendous help in the past five years: Dr. Si Li for his outstanding work on developing the reconstruction algorithm; Dr. Levon Vogelsang for his SPECT reconstruction program, which introduced me to the world of tomographic imaging; Dr. Hongwei Ye and Dr. Russell Kincaid for their career advice that helped me design my career path; and Zhifeng Wu and Wei Zheng for our many thoughtful discussions throughout the years.

I would also like to take this opportunity to thank my defense committee for their time devoted to helping me improve my work: Dr. Lixin Shen, Dr. Liviu Movileanu, Dr. Jennifer Schwarz, and Dr. John Laiho.

Finally, I would like to thank my parents, Shaoyan Liu and Ge Zhang, for their faith in me. I would also like to thank my fiancé, Wenli Tang, for her unconditional love and optimism. Without all your support throughout these years, getting a PhD would have been an insurmountable task.

Chapter 1. Introduction

1.1. SPECT imaging

Single photon emission computed tomography (SPECT) is a commonly used nuclear medicine imaging modality [1, 2]. In SPECT imaging, a radioactive tracer, often a surrogate of a substance involved in biological processes of clinical interest, is administered to the patient. After uptake time, to allow the radiotracer to be absorbed and distributed, the patient is placed on the bed of a SPECT scanner. Gamma cameras are used to detect gamma photons emitted by the radiotracer within the patient's body. In the imaging process, one or more gamma cameras orbit around the patient and acquire a sequence of gamma-ray projection images. The process of image reconstruction produces an estimate of 3D activity distribution in the patient from a set of 2D projections detected from a large number of angles. The 3D image, reflecting the function of certain organs or tissues, is used by radiologists to examine if there are functional abnormalities.

1.1.1 Anger camera

Initially introduced by Anger in the 1950s [3], scintillation cameras, also known as Anger cameras, have seen significant improvements in recent decades [4]. As shown in Fig.1.2, a conventional Anger camera consists of a collimator, a large continuous crystal scintillator, an array of photomultiplier tubes (PMTs), and a logic circuit behind the PMTs.

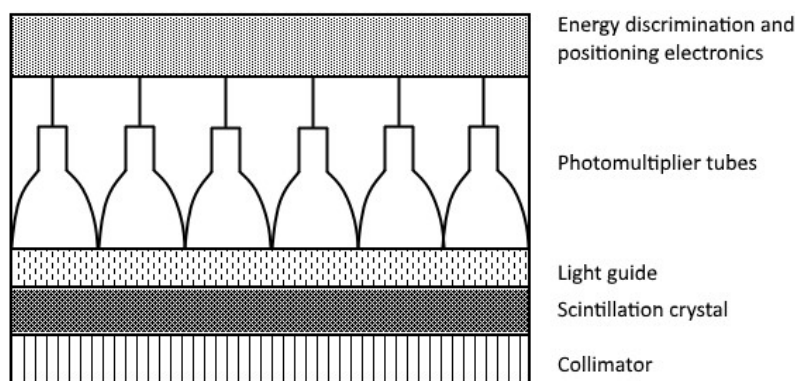


Fig. 1.1. Schematic figure of an Anger camera.

The process of detecting a gamma photon is as follows. First, the photon with an appropriate incident angle passes through collimator. The photon then deposits its energy in the scintillation crystal, after which visible light photons are emitted in the crystal. The light pulse passes through the light guide and reaches the photocathode of photomultiplier tubes (PMTs), in which photon pulses are converted to electric current. The magnitude of photocurrent generated in the PMTs is proportional to the number of visible photons, and thus proportional to the energy deposited in scintillation crystal by the incident gamma photon. The electronic circuitry behind the PMTs estimates the incident energy and position of the photon. The location of the photon is binned into an imaginary detector element, the index of which is recorded. After the acquisition, the number of gamma photon counts within the selected energy window detected by each detector element is stored in the computer system of the SPECT scanner.



Fig. 1.2. NaI scintillation crystal. [5]

A sodium iodide (NaI) crystal (Fig. 1.2), is often used as the scintillator; its many advantages include high light output and relatively low cost. Compared with semiconductor detectors, its key weaknesses are longer dead time and lower energy resolution. For use in SPECT gamma cameras, the cost effectiveness outweighs those disadvantages.

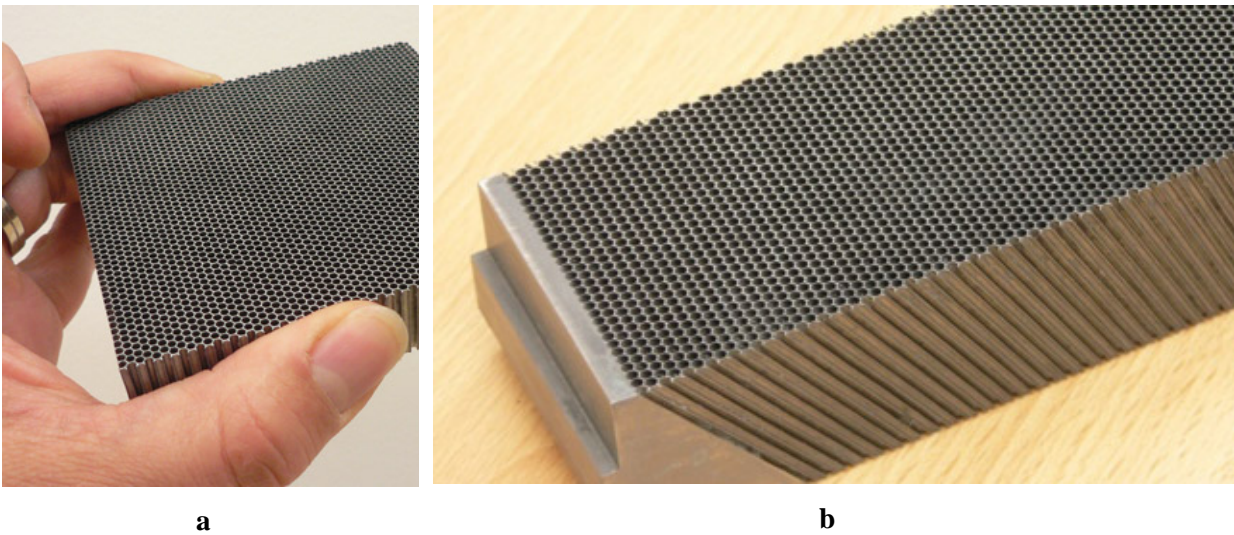


Fig. 1.3. Collimators with (a) parallel beam design and (b) fan beam design. [6]

Collimators are used to retain photons from a region of interest with defined incident angles and absorb photons from other directions. Proper collimators must be selected for gamma rays of different energies in order to optimize the sensitivity and spatial resolution tradeoff. There are two types of collimators widely used in clinical settings: parallel-beam and fan-beam (Fig. 1.3). Other types of collimators, including cone-beam and pinhole collimators, are also used for small animal studies. Fan-beam and cone-beam collimators are also known as converging collimators. The advantage of converging collimators over parallel-beam collimators is improved sensitivity, by effective use of a larger scintillator area. Considering that sensitivity is correlated with the number of photons detected by the gamma camera, the use of converging collimators can lead to better reconstructed images if the radiotracer activity within the patient and the acquisition time both remain unchanged. It has been shown that converging collimators have better image lesion detectability in certain cases [7, 8].

In our simulation and experimental studies, we used a Siemens E.Cam dual-head camera with low-energy high-resolution (LEHR) parallel-beam collimators, and a Trionix Triad triple-head camera with LEHR fan-beam collimators.

1.1.2 Tomographic imaging

A sequence of 2D projection sets are obtained in the SPECT imaging process. Three-dimensional functional information can be recovered through image reconstruction. Tomographic image reconstruction by definition is an inverse problem [9]. Carefully solving this problem and thereby accurately recovering radiotracer distribution within a patient's body is a crucial process in SPECT imaging.

As an inverse problem, image reconstruction is ill-posed, in that fluctuations of detected photon counts may significantly affect the quality of reconstructed images. Therefore, image regularization, which serves as a stabilizer of the otherwise unstable solution, is often required. Regularization methods will be discussed in Chapter 5.

1.1.3 Clinical applications and radiation dose considerations

Due to the nature of the imaging process, SPECT images yield 3D functional information, differentiating SPECT from traditional structural imaging modalities like CT. SPECT is currently widely used for thyroid studies, ventilation/perfusion studies, and whole-body-bone studies [2].

Gamma rays, as ionizing radiation, are likely to increase the stochastic risks of patients getting cancer even at low dose. According to the "linear-no-threshold" (LNT) risk model, which

is supported by recent studies [10], the cancer risk is linearly proportional to radiation dose without a threshold, and even a small radiation dose is likely to cause a slight increase in risk to the patient. The effective dose per individual in the U.S. population has increased from 3.6 mSv in the early 1980s to 6.2 mSv in 2006 [11]. The increase is mainly due to the wide use of ionizing radiation in medical exams, including fluoroscopy, x-ray computed tomography (CT), positron emission tomography (PET), and SPECT. Therefore, it is important to aggressively reduce unnecessary radiation dose to patients to assure the best patient care quality. There are increasing efforts in the medical physics community to control and reduce patient dose.

Radiation dose reduction in SPECT reconstruction is the main motivation of this study. We hope to achieve dose reduction for patients in SPECT imaging through effective noise suppression in the iterative image-reconstruction process.

1.2. Objectives

The main objective of this study is to investigate the possibility of reducing radiation dose to patients in SPECT imaging while maintaining image quality for diagnostic use. In SPECT, the photon counts detected by gamma cameras obey Poisson statistics. Therefore, lower dose, with the same image acquisition time (and same SPECT machine), corresponds to lower counts and higher noise in projection data. Effective noise suppression in an iterative reconstruction process without significantly compromising resolution or contrast recovery is our approach to achieve the objective above. Specifically, by introducing several regularization methods to SPECT image reconstruction and thoroughly evaluating their performances, we aim to prove they are viable solutions to low-dose SPECT reconstruction.

1.3. Overview of dissertation

Chapter 2 provides a brief review of the SPECT imaging model and the theoretical basis of iterative image reconstruction. In Chapter 3, we discuss numerical experiment design, and image quality metrics, followed in Chapter 4 by qualitative comparison of images reconstructed using several regularization methods. In Chapter 5, we summarize the contributions of our study, and discuss possible future work.

1.4. Publications on and presentations of this dissertation work

1. J. Zhang, S. Li, E. Lipson, D. Feiglin, Y. Xu, and A. Krol, Infimal convolution-based proximity algorithm for SPECT reconstruction, submitted.
2. S. Li, J. Zhang, C. Schmidtlein, E. Lipson, D. Feiglin, Y. Xu, and A. Krol, Comparative studies of TV-PAPA, FB-EM-TV, and beyond, submitted.
3. S. Li, J. Zhang (co-first author), A. Krol, L. Vogelsang, L. Shen, C. Schmidtlein, E. Lipson, D. Feiglin, and Y. Xu, Effective noise-suppressed reconstruction of SPECT data using a preconditioned alternating projection algorithm. *Med. Phys.* 42, 4872 (2015); <http://dx.doi.org/10.1118/1.4926846>.
4. C. Schmidtlein, J. Turner, M. Thompson, K. Mandal, I. Haggstrom, J. Zhang, J. Humm, D. Feiglin, and A. Krol, Performance modeling of a wearable brain PET (BET) camera. Proc. SPIE 9788, Medical Imaging 2016: Biomedical Applications in Molecular, Structural, and Functional Imaging, 978806 (March 29, 2016); doi:10.1117/12.2217020.

5. J. Zhang, S. Li, Y. Xu, C. Schmidtlein, E. Lipson, D. Feiglin, and A. Krol, SPECT reconstruction using DCT-induced tight framelet regularization. *Proc. SPIE 9412, Medical Imaging 2015: Physics of Medical Imaging*, 94123H (March 18, 2015); doi:10.1117/12.2082118.
6. J. Zhang, S. Li, E. Lipson, C. Schmidtlein, D. Feiglin, Y. Xu, and A. Krol, Image Quality Comparison of Reconstruction Using Total Variation-Based Regularizers. *J. Nucl. Med. Meeting Abstracts 55*: 543.
7. A. Krol, S. Li, Y. Xu, J. Zhang, L. Vogelsang, L. Shen, D. Feiglin, 2013. Semi-dynamic preconditioned alternating projection MAP ECT reconstruction from low-dose ECT. *Proc. SPIE 8668, Medical Imaging 2013: Physics of Medical Imaging*, 86685F (March 19, 2013); doi: 10.1117/12.2008153.
8. J. Zhang, A. Krol, S. Li, Z. Wu, L. Vogelsang, L. Shen, C. Schmidtlein, E. Lipson, Y. Xu, and D. Feiglin, 2014, Comparison of SPECT lesion detectability between preconditioned alternating projection algorithm (PAPA) and expectation-maximization algorithm with total variation regularizer (EM-TV) , *J. Nucl. Med. Meeting Abstracts 2014 55*:543.
9. C. Schmidtlein, S. Li, Z. Wu, J. Zhang, L. Vogelsang, L. Shen, Y. Xu, D. Feiglin, B. Beattie, J. Humm, and A. Krol, 2014. Improved Image Quality in Brain F-18 FDG PET using penalized-likelihood image reconstruction via a generalized preconditioned alternating projection algorithm: the first patient results. *Med. Phys.*, 41, 438 (2014), DOI:<http://dx.doi.org/10.1118/1.4889209>.

Chapter 2. Principles of SPECT imaging

The key strength of SPECT as a tomographic imaging modality is the ability to reveal functional information within the patient body by estimating radiotracer distribution. To accurately recover the radiotracer distribution from acquired raw data, there are two crucial aspects to be considered: the physics processes involved in image acquisitions and the methods used to solve the inverse problem known as image reconstruction.

2.1 SPECT imaging model

In this section, we briefly discuss the notations used in this dissertation, several image degrading factors involved in SPECT imaging, and the methods we use to correct and/or compensate for these factors.

2.1.1 Notations

In commonly used reconstruction models, the imaging space is discretized as small cubic volumes (voxels). Tracer distribution in the human body is then denoted as vector \mathbf{f} , with its components representing radiotracer activity contained in voxels of imaging space, i.e. f_j represents the radiation activity contained in voxel j . Similarly, a projection set is represented as a vector \mathbf{g} , and its component g_i represents the number of photons detected in detector element i . The detection process is characterized as system matrix A , whose elements A_{ij} represent the response of detector element i to voxel j . Note that the system matrix A , albeit large ($\sim 10^{12}$), is very sparse by nature. Typically, only around 1% of its elements are non-zero. In this

dissertation, for symbolic consistency, we reserve letter j for indexing voxels, and letter i for indexing detector elements.

In our SPECT imaging system with reconstruction space of size $p \times p \times q$ and projection space of size $p \times q \times s$, the relation of detector element index i and row number v , column number u , and projection angle number m is:

$$i = u + v \times p + m \times p \times q. \quad (2.1)$$

Similarly, the relation of voxel index j and row number y , column number x , and slice number z is:

$$j = x + y \times p + z \times p \times p. \quad (2.2)$$

The Kronecker tensor product, denoted by \otimes , is used to transfer a linear operation on 1D data to 3D vectorized data. Linear operators of the 3D imaging space can be described by a combination of Kronecker tensor products of unit matrices and 1D linear operators. For instance, we define a 1D convolution operation as F_p acting on a vector of size p , and it is a circulant $p \times p$ matrix. Then, the operation in the x direction of a reconstructed image can be represented by

$$B_x = I_q \otimes I_p \otimes F_p$$

where I_p and I_q are $p \times p$ and $q \times q$ unit matrices, respectively.

2.1.2 Modeling the detection of gamma photons

2.1.2.1 Sensitivity

The sensitivity of a gamma camera is defined as the total amount of photons detected per unit activity located at a given position in unit time without photon-attenuating medium.

Sensitivity depends strongly on collimator geometry: it is positively correlated with collimator hole diameter, and negatively correlated with collimator thickness and septum thickness [12].

For a gamma camera with a parallel beam collimator, sensitivity is approximately uniform across the field-of-view; for a gamma camera with a converging beam collimator (fan beam and cone beam), sensitivity depends on the distances from the source to the collimator and to the center of the mid plane (the plane that passes through the isocenter of the gantry and is perpendicular to the collimator).

2.1.2.2 Spatial resolution

The response of a gamma camera to a pencil beam perpendicular to the surface of the scintillation crystal without collimation is defined as the intrinsic detector response function (DRF), which is modeled as a Gaussian function. The FWHM of this function is determined mainly by the properties of the scintillation crystal.

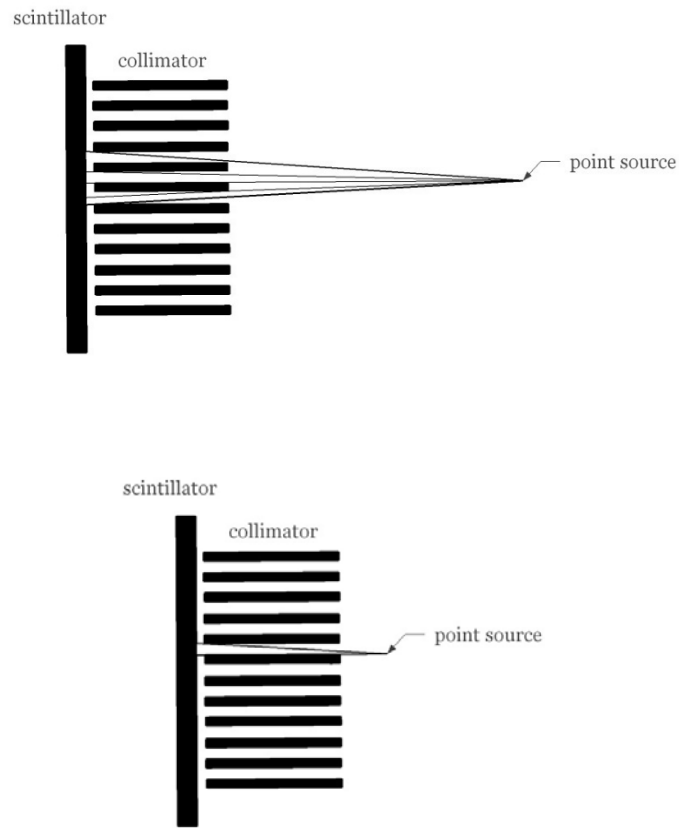


Fig. 2.1. Example of 1D collimator detector response functions for point sources at two distances from the collimator.

The collimator-detector response function (CDRF), which describes the response of a gamma camera to a point source, is the convolution of the geometry response function (GRF) and DRF. Here, GRF, defined as the response of a gamma camera with “perfect” spatial resolution to a point source, is considered as a geometric blurring factor. Since both GRF and DRF can be approximately modeled as Gaussian functions, the Gaussian radius of CDRF can be simply modeled as:

$$\sigma_{CDRF}^2 = \sigma_{DRF}^2 + \sigma_{GRF}^2$$

Note that the GRF and CDRF are not isotropic for converging collimators (fan-beam and cone-beam). CDRF is also highly depth dependent: the farther away from the collimator, the larger σ_{CDRF} is (Fig.2.1). Therefore, to achieve the best reconstruction results, CDRF needs to be carefully modeled and corrected. The depth dependence of CDRF contributes to the non-stationary nature of SPECT reconstruction. In our reconstruction program, the Gaussian radius of CDRF was obtained as a function of the distances from the source to the collimator and to the mid-plane of the collimator. We used Monte Carlo simulated point sources and experimental data to configure the function as described in detail in Chapter 3.

2.1.2.3 Attenuation and scatter

Attenuation refers to gamma photons scattered or absorbed before reaching the gamma camera. The linear attenuation coefficient μ is defined as the fraction of photons that interact with matter and are thereby removed from the beam:

$$dn = -\mu(x)ndx,$$

where dn represents the change of photon counts after passing through distance dx . Hence, the number of photons traveling through a certain path will be attenuated exponentially as:

$$n = n_0 e^{-\int \mu(x) dx},$$

where dx is an infinitesimal distance along the path and $\mu(x)$ is the attenuation coefficient at that location.

In the photon energy range of nuclear medicine imaging (100-511 keV), photoelectric effects and Compton scattering are the two main mechanisms of photon interactions with matter.

Therefore, μ can be written as:

$$\mu = \sigma + \tau,$$

where τ represents the photoelectric-effect contribution, and σ represents the Compton-scatter contribution.

Some Compton scattered photons can still reach the detector. As shown in Fig. 2.2, scattered photons are detected a random distance away from the expected detection position. The results of scatter in SPECT imaging are reduced spatial resolution and reduced image contrast. Therefore, it is important to model and correct for scattered photons. The majority of scattered photons are discriminated by the energy deposited in the scintillator: only photons within a selected energy range (energy window) are recorded. Ideally, all scattered photons lose enough energy to electrons, and would not be recorded. However, due to the limited energy resolution of the gamma camera, a 10-20% energy window is often used to collect more primary photons, and scattered photons still contribute significantly to that energy window.

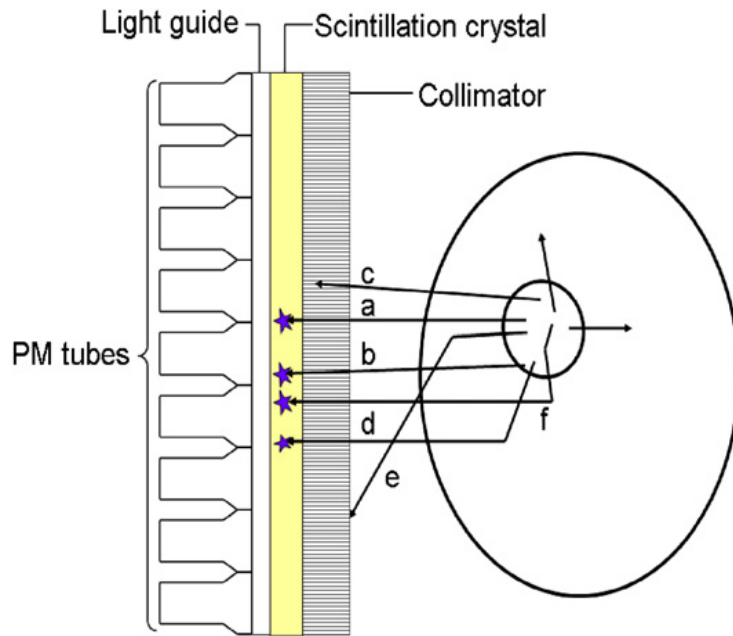


Fig. 2.2. Photons emitted from patients and detected by gamma camera or absorbed by collimator. Trajectories of gamma photons are shown. (a) Photon passes through the collimator directly and is detected. (b) Photon penetrates collimator septum and is detected. (c) Photon is absorbed by collimator septum. (d) Photon is scattered once within patient body and is detected. (e) Photon is scattered once within patient body and is absorbed by collimator. (f) Photon scatters multiple times within patient body and is detected. [13]

One popular method of scatter correction in SPECT is triple energy window (TEW) scatter correction [14]. It uses photon counts that falls in two narrow energy windows above and below the photopeak window to estimate the counts contributed by scattered photons. The scatter estimate for detector element i is:

$$s_i = \left(\frac{(g_{low})_i}{W_{low}} + \frac{(g_{high})_i}{W_{high}} \right) \times \frac{W_p}{2},$$

where $(g_{low})_i$ and $(g_{high})_i$ are the number of photons recorded in the predefined lower and higher energy windows W_{low} and W_{high} , respectively; and W_p is the width of the photopeak window.

The TEW method is commonly used to distinguish the desirable photon peak for radio isotopes with multiple photopeaks or multiple radiotracers. Our simulations and experiments were done using Tc-99m, the decay scheme of which only involves one photopeak, so we only used dual energy window (DEW) with a lower energy window for estimating scattered photon counts.

We added the scatter estimate obtained in the lower energy window to the estimated projection data in the iterative reconstruction process to avoid negative values. It has been shown that this method can reduce the root mean square error (RMSE) of reconstructed images, compared with the direct subtraction method [15].

It has been argued that this method is problematic in theory because at 140keV (the energy of photons emitted by Tc-99m, the most commonly used isotope in SPECT), even a 10% energy difference means a scatter angle of 53° . More sophisticated model-based methods have been proposed, including transmission dependent convolution subtraction (TDCS) [16], effective scatter source estimation (ESSE) [17], and full Monte Carlo-based scatter correction methods with variance reduction techniques [18-20]. These methods have shown some advantages compared with traditional energy-window based methods.

2.1.3 System matrix A

In this dissertation, we use A_{ij} to denote the response of detector element i to a point source with unit activity in voxel j (Fig. 2.3.). The so-called system matrix A contains information necessary for image reconstruction, including sensitivity, spatial resolution, scatter, and attenuation. A row of matrix A represents the response of one detector element to all voxels

in the reconstruction space; a column of A represents the expected number of photons contributed by one voxel with unit activity to all detector elements. Therefore, the deterministic (noise-free) approximation of the detection process is:

$$\mathbf{g} = A\mathbf{f}. \quad (2.3)$$

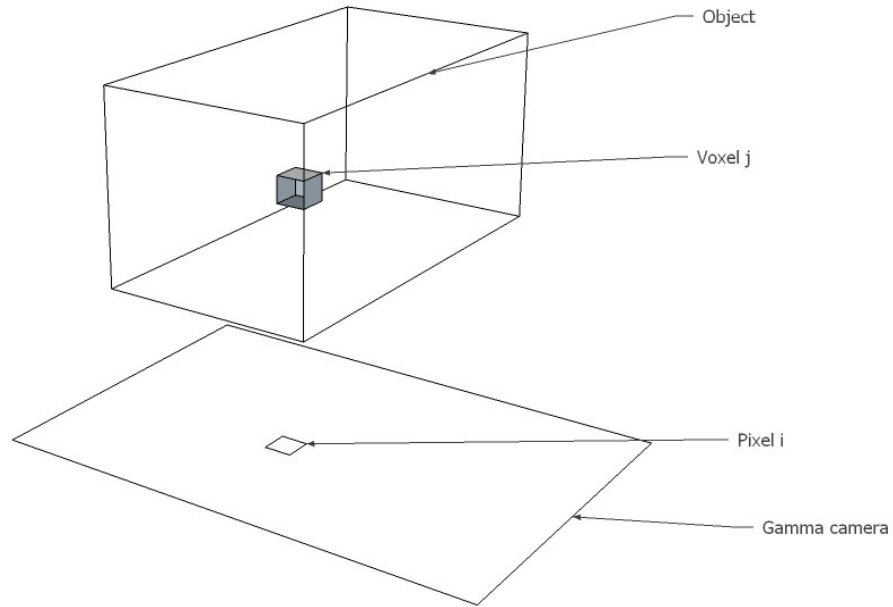


Fig. 2.3. Schematic figure of voxel j , pixel i , and system matrix element A_{ij} .

When acting on the current estimate \mathbf{f} , the system matrix converts it to the projection domain, which, in turn, can be compared to the measured data \mathbf{g} . Note that A^T is known as the back projection operation used in iterative reconstruction to convert projection data back to reconstruction space.

2.2 Iterative image reconstruction

It used to be common practice to reconstruct SPECT images using analytical methods known as filtered back projection (FBP) [21]. FBP is based on the central-slice theorem (or projection slice theorem), which states that the 1D Fourier transform (FT) of a line of pixel values is equal to the 2D FT of the central line of voxels facing the same direction. Therefore, with good angle sampling, the full 2D Fourier domain information can be obtained, and the reconstruction images can simply be obtained by an inverse Fourier transform. This process is known as the backprojection. The backprojected images are blurry, and high-pass filters are used to reduce blurring.

FBP can produce images with decent quality at very low computational cost. However, it does not allow incorporation of a sophisticated collimator-detector response function (CDRF), model-based attenuation correction, or statistical modeling. As a result, FBP-reconstructed images are often degraded by artifacts, and do not preserve spatial resolution well. Therefore, iterative reconstruction methods have been developed.

2.2.1 Maximum-likelihood reconstruction criteria

Maximum likelihood (ML) [22, 23] is a reconstruction criterion commonly used in emission tomography image reconstruction. It is based on the assumption that the numbers of radiotracer photons emitted from voxels are independent Poisson random variables, and thus photon counts at detector elements are independent Poisson random variables as well.

Subsequently, the objective is to maximize the likelihood of measured projection data \mathbf{g} with radiotracer distribution \mathbf{f} . The likelihood function can be written as:

$$P(\mathbf{g} | \mathbf{f}) = \prod_i \frac{\left(\left(\sum_j A_{ij} f_j \right)^{g_i} e^{-\sum_j A_{ij} f_j} \right)}{g_i!}, \quad (2.4)$$

where f_j is the total activity of voxel j in reconstruction space; and g_i is the photon count at pixel i . This function is very complicated and hard to evaluate. Fortunately, we can maximize the natural logarithm of this function instead, since logarithm is a monotonic function. The log-likelihood function is then:

$$\ln[P(\mathbf{g} | \mathbf{f})] = \sum_i \left[g_i \ln \left(\sum_j A_{ij} f_j \right) - \sum_j A_{ij} f_j - \ln(g_i!) \right]. \quad (2.5)$$

Therefore, the maximum likelihood criterion is:

$$\begin{aligned} \hat{\mathbf{f}}_{ML} &= \arg \max_f \ln[P(\mathbf{g} | \mathbf{f})] \\ &= \arg \max_f \left[\sum_i g_i \ln \left(\sum_j A_{ij} f_j \right) - \sum_i \sum_j A_{ij} f_j - \ln(g_i!) \right] \\ &= \arg \max_f \left[\sum_i g_i \ln \left(\sum_j A_{ij} f_j \right) - \sum_i \sum_j A_{ij} f_j \right] \end{aligned} \quad (2.6)$$

2.2.2 Maximum-likelihood expectation-maximization (ML-EM) algorithm

The expectation maximization (EM) algorithm was first proposed as a general algorithm by Dempster [24], and later was used in tomographic image reconstruction by Lange and Carson [23], and Shepp and Vardi [22]. The EM algorithm and its variants have since been the most popular algorithms of image reconstruction in emission tomography.

The idea of ML-EM is to convert the optimization problem (2.4) to an easier one, and solve it via iteration. Assuming c_{ij} is the number of photons emitted within voxel j and detected by detector element i , we have

$$g_i = \sum_j c_{ij} \quad (2.7)$$

$$\begin{aligned} \hat{\mathbf{f}} &= \arg \max_f \ln [P(\mathbf{g} | \mathbf{f})] \\ &= \arg \max_f \ln \frac{P(\mathbf{g} | \mathbf{c}, \mathbf{f}) P(\mathbf{c} | \mathbf{f})}{P(\mathbf{c} | \mathbf{g}, \mathbf{f})} \end{aligned} \quad (2.8)$$

Since $P(\mathbf{g} | \mathbf{c}, \mathbf{f}) = 1$, the equation above reduces to:

$$\hat{\mathbf{f}} = \arg \max_f \left\{ \ln [P(\mathbf{c} | \mathbf{f})] - \ln [P(\mathbf{c} | \mathbf{g}, \mathbf{f})] \right\} \quad (2.9)$$

Next, take the expectation of c_{ij} conditioned on the current estimate of radiotracer distribution f^n , and detected data \mathbf{g} :

$$\hat{\mathbf{f}} = \arg \max_f \left\{ Q(\mathbf{f} | \mathbf{f}^n) + H(\mathbf{f} | \mathbf{f}^n) \right\}, \quad (2.10)$$

where

$$H(\mathbf{f} | \mathbf{f}^n) = E \left\{ -\ln [P(\mathbf{c} | \mathbf{g}, \mathbf{f})] | \mathbf{g}, \mathbf{f}^n \right\} \quad (2.11)$$

$$Q(\mathbf{f} | \mathbf{f}^n) = E \left\{ \ln [P(\mathbf{c} | \mathbf{f})] | \mathbf{f}^n, \mathbf{g} \right\} \quad (2.12)$$

Due to Jensen's inequality and the fact that the natural logarithm is a concave function, $H(\mathbf{f} | \mathbf{f}^n)$ achieves its minimum when $\mathbf{f} = \mathbf{f}^n$. Additionally, assuming the c_{ij} elements are independent Poisson random variables,

$$P(\mathbf{c} | \mathbf{f}) = \prod_{i,j} \frac{(A_{ij} f_j)^{c_{ij}} e^{-A_{ij} f_j}}{c_{ij}!} \quad (2.13)$$

where A_{ij} is the expected value of c_{ij} . Therefore,

$$\ln[P(\mathbf{c} | \mathbf{f})] = \sum_{i,j} [c_{ij} \ln(A_{ij} f_j) - A_{ij} f_j - \ln(c_{ij}!)] \quad (2.14)$$

Then the maximization problem can be formularized as:

$$\begin{aligned} \hat{\mathbf{f}} &= \arg \max_{\mathbf{f}} Q(\mathbf{f} | \mathbf{f}^n) \\ &= \arg \max_{\mathbf{f}} E \{ \ln [P(\mathbf{c} | \mathbf{f})] | \mathbf{f}^n, \mathbf{g} \} \\ &= \arg \max_{\mathbf{f}} E \left\{ \sum_{i,j} [c_{ij} \ln(A_{ij} f_j) - A_{ij} f_j - \ln(c_{ij}!)] | \mathbf{f}^n, \mathbf{g} \right\} \\ &= \arg \max_{\mathbf{f}} E \left\{ \sum_{i,j} [c_{ij} \ln f_j - A_{ij} f_j] | \mathbf{f}^n, \mathbf{g} \right\} \\ &= \arg \max_{\mathbf{f}} \sum_{i,j} [E(c_{ij} | \mathbf{f}^n, \mathbf{g}) \ln f_j - A_{ij} f_j] \end{aligned} \quad (2.15)$$

where

$$E(c_{ij} | \mathbf{f}^n, \mathbf{g}) = \frac{A_{ij} f_j^n g_i}{\sum_{j'} A_{ij'} f_{j'}^n} \quad (2.16)$$

After taking the partial derivative of $Q(\mathbf{f} | \mathbf{f}^n)$ with respect to f_j , we have

$$\frac{\partial Q(\mathbf{f} | \mathbf{f}^n)}{\partial f_j} = \sum_i \left(\frac{A_{ij} f_j^n g_i}{\sum_{j'} A_{ij'} f_{j'}^n} \frac{1}{f_j} - A_{ij} \right) \quad (2.17)$$

It is easy to verify that the second order derivative is negative, hence the solution to the equation is the maximizer of $Q(\mathbf{f} | \mathbf{f}^n)$ with respect to \mathbf{f} . We set the first order derivative to zero and let f_j be the $(n+1)^{\text{th}}$ iteration.

$$f_j^{n+1} = \frac{f_j^n}{\sum_i A_{ij}} \sum_{i'} \frac{A_{i'j} g_{i'}}{\sum_{j'} A_{i'j'} f_{j'}^n} \quad (2.18)$$

This iteration scheme ensures that the value of log likelihood increases monotonically with the number of iterations. It has also been pointed out that the EM algorithm can be simply viewed from an optimization-transfer perspective [25]: a properly selected surrogate function can reduce the difficulty of solving the original problem directly.

Accelerated versions of ML-EM have been developed to speed up the reconstruction process. The most popular one is the ordered-subset variant of EM algorithm (OS-EM) [26], which is the most widely used iterative reconstruction algorithm in clinical settings. The idea of OS-EM is to divide the projection data \mathbf{g} into several subsets based-on the projection views, and use only one subset during the forward/backward projection routine in the ML-EM algorithm to update the radiotracer estimate \mathbf{f} . Note that the most computationally heavy step of reconstruction is the projection/backprojection routine. The OS version requires a lot less time per image update. The convergence of OS-EM has not been proven, and the reconstructed results tend to oscillate with subsets after a number of iterations. In contrast, rescaled block iterative-EM (RBI-EM) [27] has proven full convergence. When the views are “balanced” in subsets of OS-EM, then RBI-EM would reduce to OS-EM. Therefore, OS-EM converges well under such conditions.

In practice, however, reconstructions without iterative regularization are often stopped before full convergence to avoid excessive noise, and OS-EM often provides reliable image quality when stopped early.

2.2.3 Maximum *a posteriori* (MAP) reconstruction criteria

Reconstruction as an inverse problem is ill-conditioned, which means the photon count fluctuations often translate to significant noise variance in reconstructed images. In clinical practice, this problem is usually avoided by stopping before full convergence, and applying post reconstruction smoothing.

In comparison, iterative regularization methods incorporate regularization methods in the reconstruction criterion and solve the modified problem via iterations. Compared with common clinical practice, iterative regularization methods are usually advantageous because they allow incorporation of prior knowledge of activity distribution, such as low spatial gradient and anatomical boundary information.

According to Bayesian statistics, the *a posteriori* probability is related to likelihood as follows:

$$P(\mathbf{f} | \mathbf{g}) = \frac{P(\mathbf{g} | \mathbf{f})P(\mathbf{f})}{P(\mathbf{g})}. \quad (2.19)$$

The maximum *a posteriori* (MAP) reconstruction criterion uses the natural log of *a posteriori* probability $\ln P(\mathbf{f} | \mathbf{g})$ as the objective function instead of the log-likelihood $\ln P(\mathbf{g} | \mathbf{f})$. The MAP criterion can thus be written as:

$$\begin{aligned} \hat{\mathbf{f}}_{MAP} &= \arg \max_f \ln P(\mathbf{f} | \mathbf{g}) \\ &= \arg \max_f [\ln P(\mathbf{g} | \mathbf{f}) + \ln P(\mathbf{f}) - \ln P(\mathbf{g})] \\ &= \arg \max_f [\ln P(\mathbf{g} | \mathbf{f}) + \ln P(\mathbf{f})] \end{aligned} \quad (2.20)$$

where $P(\mathbf{f})$ represents prior knowledge of radiotracer distribution within human body. The Gibbs prior [28, 29] is commonly used:

$$P(\mathbf{f}) = Ce^{-\lambda U(\mathbf{f})} \quad (2.21)$$

With the Gibbs prior, the MAP reconstruction can be re-formularized as:

$$\hat{\mathbf{f}}_{MAP} = \arg \max_{\mathbf{f}} \left[\sum_{i,j} [g_i \ln(A_{ij}f_j) - A_{ij}f_j] - \lambda U(\mathbf{f}) \right]. \quad (2.22)$$

Alternatively, this objective function can be interpreted as the Kullback-Leibler (KL)-divergence [30] term which is derived from the Poisson model, plus a noise-suppressing penalty term [31]. Solutions with noise fluctuations are penalized, resulting in smooth reconstructed images. Therefore, the MAP reconstruction criterion is also called the penalized maximum likelihood (PL) criterion.

There have been many methods proposed for solving the PL model, including EM-type methods [32-34], projected quasi-Newton methods [35-37], primal-dual methods [38-40], and fixed-point proximity methods [41, 42]. The selection of the regularization term $U(\mathbf{f})$ greatly affects the appearances of reconstructed images. Detailed discussion regarding this topic can be found in Chapter 5.

2.2.4 Preconditioned alternating projection algorithm (PAPA)

PAPA was developed by Krol *et al* [41] on the basis of an earlier study [43], with an added EM-inspired preconditioning matrix [44, 45]. The basic idea of PAPA is to utilize a subdifferential operator to represent the optimal condition of the reconstruction problem, and then characterize the problem using proximity operators, which is subsequently used to derive fixed point iterative reconstruction algorithm.

Other alternative algorithms for solving the MAP model include the one-step-late method (OSL) [46], and the forward-backward splitting method (FB-EM) [33]. Compared with other methods, the advantages of PAPA are its solid convergence proof and its versatility. The convergence proof given in [41] applies for any regularization function that can be written as a composite function of convex function φ and a linear operator B . Therefore, PAPA can be easily modified to solve other regularization models as long as the proximity operator of φ can be written in closed form.

The PAPA algorithm is used for most reconstructions done in this dissertation. Detailed pseudo code of this algorithm applied to multiple regularization functions can be found in Appendix A.

2.2.4.1 Notations and concepts involved in PAPA

Before introducing PAPA, we shall introduce several concepts and notations involved in the derivation and the iteration scheme. First, the proximity operator is defined as:

$$prox_{\varphi}(\mathbf{x}) = \arg \min \left\{ \frac{1}{2} \|\mathbf{u} - \mathbf{x}\|_2^2 + \varphi(\mathbf{u}) : \mathbf{u} \in H \right\}, \quad (2.23)$$

where $\|\cdot\|_2$ is the ℓ_2 norm, and H denotes an Euclidian space. Basically, for a convex function φ , the function $prox_{\varphi}(\mathbf{x})$ moves from \mathbf{x} in the direction of $-\nabla \varphi(\mathbf{x})$, provided $\varphi(\mathbf{x})$ exists, and is differentiable in that region.

Second, the subdifferential of a function $\varphi(\mathbf{x})$ is defined as:

$$\partial \varphi(\mathbf{x}) = \{ \mathbf{y} : \mathbf{y} \in H \text{ and } \varphi(\mathbf{z}) \geq \varphi(\mathbf{x}) + \langle \mathbf{y}, \mathbf{z} - \mathbf{x} \rangle, \forall \mathbf{z} \in H \}, \quad (2.24)$$

The elements of the subdifferential are called subgradients. The concept of subgradient is considered an extension of gradient, and it is often implemented to deal with functions that cannot be directly differentiated. If the function $\varphi(\mathbf{x})$ is differentiable at x , then the only subgradient of $\varphi(\mathbf{x})$ is the gradient itself. For \mathbf{x} in the domain of $\varphi(\mathbf{x})$ and $\mathbf{y} \in H$, the subgradient $\partial\varphi(\mathbf{x})$ can be related to the proximity operator:

$$\mathbf{y} \in \partial\varphi(\mathbf{x}) \Leftrightarrow \mathbf{x} = \text{prox}_{\varphi}(\mathbf{x} + \mathbf{y}). \quad (2.25)$$

Finally, the indicator function of a closed convex set C in H is defined as:

$$I_C(u) = \begin{cases} 0, & u \in C \\ +\infty, & u \notin C \end{cases}. \quad (2.26)$$

2.2.4.2 Re-formulation of ℓ_1 norm and hybrid norm regularization terms

With the use of inner product, denoted as $\langle \cdot, \cdot \rangle$, the negative MAP objective function (2.22) can be rewritten as:

$$F(\mathbf{f}) = \langle A\mathbf{f}, \mathbf{1} \rangle - \langle \ln(A\mathbf{f} + \gamma), \mathbf{g} \rangle + \lambda\varphi(B\mathbf{f}), \quad (2.27)$$

where \mathbf{f} is a vector of size $M = p \times p \times q$ that denotes the radiotracer distribution within M voxels; \mathbf{g} is a vector of size $N = p \times q \times o$ that denotes the measured counts in N total detector elements; B is a matrix of size $KM \times M$ that exploits certain features of true radiotracer distribution f^* (e.g. difference of neighbor voxels in certain directions); γ is a vector with a very small constant value that represents the expected number of counts due to background scattering. Usually, the vector $B\mathbf{f}$ is expected to be sparse, and thus penalizing $\varphi(B\mathbf{f})$ is effectively

penalizing reconstructions with unlikely features produced by fluctuations of measured data. In SPECT imaging, the radiotracer is expected to have a mostly continuous distribution with some edges at anatomical boundaries, and it can be approximately characterized as local spatial variability. The regularization term is thus usually used to represent noise in reconstructed images and can be easily penalized.

In this dissertation, the penalty terms involved are mainly ℓ_1 norm of Bf , or ℓ_1 norm combined with ℓ_2 norm locally at each voxel. The ℓ_1 norm of Bf is defined as:

$$\varphi_{\ell_1}(Bf) = \sum_{m=1}^M \left\| \left[(Bf)_m, (Bf)_{m+M}, (Bf)_{m+2M}, \dots, (Bf)_{m+(K-1)M} \right]^T \right\|_1, \quad (2.28)$$

and the hybrid norm of Bf is defined as:

$$\varphi_{\text{hybrid}}(Bf) = \sum_{m=1}^M \left\| \left[(Bf)_m, (Bf)_{m+M}, (Bf)_{m+2M}, \dots, (Bf)_{m+(K-1)M} \right]^T \right\|_2. \quad (2.29)$$

Considering $\|\mathbf{a}\|_1 = \max_{\|\mathbf{b}\|_\infty \leq 1} \langle \mathbf{b}, \mathbf{a} \rangle$ and $\|\mathbf{a}\|_2 = \max_{\|\mathbf{b}\|_2 \leq 1} \langle \mathbf{b}, \mathbf{a} \rangle$, the functions $\varphi_{\ell_1}(Bf)$ and $\varphi_{\text{hybrid}}(Bf)$ in equation (2.28) and (2.29) can be re-written as:

$$\varphi_{\ell_1}(Bf) = \max_{\|\mathbf{b}\|_\infty \leq 1} \langle \mathbf{b}, Bf \rangle \quad (2.30)$$

and

$$\varphi_{\text{hybrid}}(Bf) = \max_{\|\mathbf{b}\|_2 \leq 1} \langle \mathbf{b}, Bf \rangle, \quad (2.31)$$

where \mathbf{b} is a vector of the size of KM . Since φ_{hybrid} is a convex function, we have

$$\begin{aligned} \varphi_{\text{hybrid}}(Bf_1) - \varphi_{\text{hybrid}}(Bf_2) &\geq \varphi_{\text{hybrid}}(Bf_1 - Bf_2) \\ &\geq \langle \mathbf{b}, Bf_1 - Bf_2 \rangle; \quad \|\mathbf{b}\|_2 \leq 1, \end{aligned} \quad (2.32)$$

which can then be rearranged as

$$\varphi_{\text{hybrid}}(\mathbf{B}\mathbf{f}_1) \geq \varphi_{\text{hybrid}}(\mathbf{B}\mathbf{f}_2) + \langle \mathbf{b}, \mathbf{B}\mathbf{f}_1 - \mathbf{B}\mathbf{f}_2 \rangle; \quad \|\mathbf{b}\|_2 \leq 1. \quad (2.33)$$

Based on the definition of subgradient (Eq. 2.24), the maximizer \mathbf{b} for equations (2.31) is a subgradient of $\varphi_{\text{hybrid}}(\mathbf{B}\mathbf{f})$. Similarly, it can be shown that the maximizer \mathbf{b} for equations (2.30) is a subgradient of $\varphi_{11}(\mathbf{B}\mathbf{f})$. Therefore, in both cases, we have

$$\mathbf{b} \in \partial_f \varphi(\mathbf{B}\mathbf{f}). \quad (2.34)$$

We now define function $H(\mathbf{f}, \mathbf{b})$ as follows:

$$H(\mathbf{f}, \mathbf{b}) = \langle \mathbf{A}\mathbf{f}, \mathbf{1} \rangle - \langle \ln(\mathbf{A}\mathbf{f} + \gamma), \mathbf{g} \rangle + \lambda\mu \langle \mathbf{B}\mathbf{f}, \mathbf{b} \rangle. \quad (2.35)$$

$H(\mathbf{f}, \mathbf{b})$ is concave with respect to \mathbf{b} , and convex with respect to \mathbf{f} , and its saddle point

$\min_{\mathbf{f} \geq 0} \max_{\mathbf{b}} H(\mathbf{f}, \mathbf{b})$ is the solution to the original objective function (2.27). Note that $H(\mathbf{f}, \mathbf{b})$ is

differentiable with respect to both \mathbf{b} and \mathbf{f} . The gradient of $H(\mathbf{f}, \mathbf{b})$ with respect to \mathbf{f} and \mathbf{b} are:

$$\begin{aligned} \nabla_{\mathbf{f}} H(\mathbf{f}, \mathbf{b}) &= \mathbf{A}^T \left(\mathbf{1} - \frac{\mathbf{g}}{\mathbf{A}\mathbf{f} + \gamma} \right) + \lambda\mu \mathbf{B}^T \mathbf{b} \\ \nabla_{\mathbf{b}} H(\mathbf{f}, \mathbf{b}) &= \lambda\mu \mathbf{B}\mathbf{f} \end{aligned} \quad (2.36)$$

The optimization problem is now:

$$\min_{\mathbf{f}} \max_{\mathbf{b}} \left[H(\mathbf{f}, \mathbf{b}) + I_{\mathbb{R}_+^M}(\mathbf{f}) \right], \quad (2.37)$$

where the indicator function $I_{\mathbb{R}_+^M}(\mathbf{f})$ is used to keep the solution \mathbf{f} nonnegative in the minimization process.

2.2.4.3 Derivation of PAPA

First, applying Fermat's theorem with respect to \mathbf{f} to (2.35) yields

$$0 \in A^T \left(1 - \frac{\mathbf{g}}{A\mathbf{f} + \gamma} \right) + \lambda\mu B^T \mathbf{b} + \partial_{\mathbf{f}} \iota_{R_+^M}(\mathbf{f}). \quad (2.38)$$

To rewrite (2.37) more simply,

$$-\nabla_{\mathbf{f}} H(\mathbf{f}, \mathbf{b}) \in \partial_{\mathbf{f}} \iota_{R_+^M}(\mathbf{f}). \quad (2.39)$$

Based on (2.25) and (2.38), we have that

$$\mathbf{f} = \text{prox}_{\gamma}(\mathbf{f} - \nabla_{\mathbf{f}} H(\mathbf{f}, \mathbf{b})), \quad (2.40)$$

where γ is used to replace $\iota_{R_+^M}$ for simplicity.

Next, applying (2.25) to (2.34) and (2.36), we obtain

$$\mathbf{b} = (I - \text{prox}_{\phi})(\mathbf{b} + \nabla_{\mathbf{b}} H(\mathbf{f}, \mathbf{b})) \quad (2.41)$$

According to [41], there exists a pair (\mathbf{b}, \mathbf{f}) , which is the unique solution to the coupled fixed point equations (2.40) and (2.41).

Finally, we introduce a preconditioner S inspired by the ML-EM algorithm [23] to accelerate convergence. S is a diagonal matrix of size $M \times M$ defined as:

$$S = \text{diag} \left(\frac{\mathbf{f}^k}{A^T \mathbf{1}} \right).$$

S is multiplied into $\nabla_{\mathbf{f}} H(\mathbf{f}, \mathbf{b})$ in (2.40), as expressed below. The preconditioner effectively allows the algorithm to search for the solution in the same direction as EM. The solution can then be characterized by the following coupled equations (For simplicity, parameters λ and μ are omitted during the derivation.):

$$\begin{aligned}\mathbf{b} &= \left(I - \text{prox}_{\mu^{-1}\varphi} \right) \left(\mathbf{b} + \frac{1}{\lambda\mu} \nabla_{\mathbf{b}} H(\mathbf{f}, \mathbf{b}) \right) \\ \mathbf{f} &= \text{prox}_{\Upsilon} \left(\mathbf{f} - S \nabla_{\mathbf{f}} H(\mathbf{f}, \mathbf{b}) \right)\end{aligned}\quad (2.42)$$

2.2.4.4 Iteration scheme

Plugging Eq. (2.26) into (2.27), we obtain:

$$\begin{aligned}\mathbf{b} &= \left(I - \text{prox}_{\mu^{-1}\varphi} \right) \left(\mathbf{b} + \frac{1}{\lambda\mu} \nabla_{\mathbf{b}} H \left(\text{prox}_{\Upsilon} \left(\mathbf{f} - S \nabla_{\mathbf{f}} H(\mathbf{f}, \mathbf{b}) \right), \mathbf{b} \right) \right) \\ \mathbf{f} &= \text{prox}_{\Upsilon} \left(\mathbf{f} - S \nabla_{\mathbf{f}} H(\mathbf{f}, \mathbf{b}) \right)\end{aligned}\quad (2.43)$$

Then, fixed-point iterations are derived based on (2.28):

$$\begin{aligned}\mathbf{f}^{n+\frac{1}{2}} &= \text{prox}_{\Upsilon} \left(\mathbf{f}^n - S \nabla_{\mathbf{f}^n} H(\mathbf{f}^n, \mathbf{b}^n) \right) \\ \mathbf{b}^{n+1} &= \left(I - \text{prox}_{\mu^{-1}\varphi} \right) \left(\mathbf{b}^n + \frac{1}{\lambda\mu} \nabla_{\mathbf{b}} H(\mathbf{f}^{n+\frac{1}{2}}, \mathbf{b}^n) \right) \\ \mathbf{f}^{n+1} &= \text{prox}_{\Upsilon} \left(\mathbf{f}^{n+\frac{1}{2}} - S \nabla_{\mathbf{f}^{n+\frac{1}{2}}} H(\mathbf{f}^{n+\frac{1}{2}}, \mathbf{b}^{n+1}) \right)\end{aligned}\quad (2.44)$$

The proximity operators for functions involved in iteration scheme (2.44) are:

$$\text{prox}_{\Upsilon}(x) = \max \{x, 0\} \quad (2.45)$$

$$\begin{aligned}\left(\text{prox}_{\mu^{-1}\varphi_{\text{hybrid}}}(x) \right)_{m+kM} &= \max \left\{ \left\| \left[(Bf)_m, (Bf)_{m+M}, (Bf)_{m+2M}, \dots, (Bf)_{m+(K-1)M} \right]^T \right\|_2 - \frac{1}{\mu}, 0 \right\} \\ &\quad \bullet \frac{(Bf)_{m+kM}}{\left\| \left[(Bf)_m, (Bf)_{m+M}, (Bf)_{m+2M}, \dots, (Bf)_{m+(K-1)M} \right]^T \right\|_2}, \quad k \in [0, K-1]\end{aligned}\quad (2.46)$$

$$\left(\text{prox}_{\mu^{-1}\varphi_1}(x) \right)_{m+kM} = \max \left\{ \left\| (Bf)_{m+kM} \right\|_1 - \frac{1}{\mu}, 0 \right\} \quad (2.47)$$

Because of computational-cost considerations, the second step is usually iterated several steps in between step 1 and step 3. Note that $\mu\mathbf{b}$ is a subgradient of $\varphi(B\mathbf{f})$, and the backward first order difference of it, $\mu B^T \mathbf{b}$ is subtracted from the current iteration of \mathbf{f} . Therefore, it can be interpreted that $\varphi(B\mathbf{f})$ is minimized through driving its subgradient to zero.

Chapter 3. Experimental design

In order to evaluate the performance of our proposed reconstruction algorithms, we need an accurate system model, *i.e.* system matrix A , reproducible and quantifiable projection data, and image-quality quantification tools. First, we developed our degrading factor correction routines to model collimator-detector response function (CDRF), attenuation, and scatter. CDRF of gamma cameras were modeled based on experimental data. Second, to obtain realistic estimation of image quality, both Monte Carlo simulated data and clinical data were used in image reconstruction. Third, images reconstructed using various methods were later evaluated using both conventional quantitative image-quality metrics and task-based model observers.

3.1 Monte Carlo simulated projection data

Monte Carlo simulation is an important tool for evaluating image reconstruction methods in nuclear medicine. Commonly used Monte Carlo simulation packages in SPECT imaging include: SimSET [47], SIMIND [48], and GATE [49]. In Monte Carlo simulation, a large number of random photon trajectories are simulated based on probabilities of interactions. For our purpose, Monte Carlo simulation essentially describes the averaged behavior of radiotracer-emitted photons during image acquisition.

In the present work, we have used the SIMIND Monte Carlo simulation package [50] for generating SPECT projection data sets. SIMIND was developed by Professor Michael Ljungberg from Lund University, Sweden. It takes two discrete 3D matrices that represent gamma photon

attenuation and activity concentration information at each voxel, respectively. Other inputs include: energy window selection, collimator and detector information, and dimensions of voxels and detector elements. Voxelized phantoms (*e.g.* Fig.4.1a) are created to simulate the radiotracer spatial distribution in certain materials.

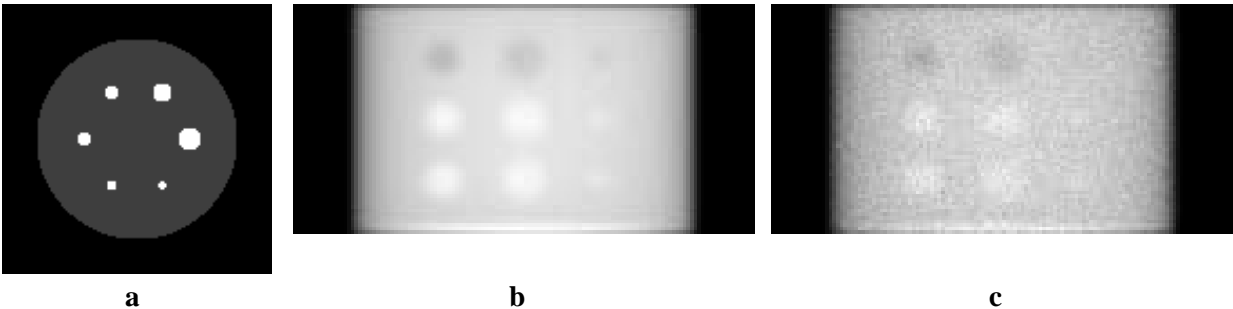


Fig. 3.1. Sample images of phantom and Monte Carlo simulated projection data. (a) Transaxial cross-section of a digital phantom, with six spheres of various sizes (b) Monte Carlo-simulated “noiseless” projection, and (c) Simulated projection with added Poisson noise.

To obtain a large number of noisy projection sets for better statistics, we simulated a sufficiently large number of photon histories ($\sim 10^9$) to make the projection data “noiseless” (*e.g.* Fig. 3.1b). We then added Poisson noise to the photon counts of each detector element to create noise realizations (*e.g.* Fig. 3.1c). In our numerical experiments in the following chapter, one hundred noise realizations were created for each noise level and each phantom projection.

3.2 Characterizing collimator-detector response function using experimental data

Experimental data were acquired for estimation of the collimator-detector response function (CDRF) of two SPECT machines. These CDRFs were later used for reconstruction of simulated data (with same configurations as these two machines) and anonymized clinical SPECT data.

3.2.1 Experimental design

A plastic phantom with 14 long grooves (10 cm length) for line sources and 7 short grooves for point sources, as shown in Fig. 3.2, was used to model CDRF of two SPECT machines in the Radiology Department of SUNY Upstate Medical University: a Siemens E.Cam and a Trionix Triad. In our experiments, both machines were modeled with their most commonly used collimators installed: low-energy high-resolution (LEHR) parallel-beam collimators for E.Cam, and low-energy high-resolution (LEHR) fan-beam collimators for Triad. Detailed protocols for the experiments are in Appendix B.



Fig. 3.2. Experiment setup for (a) Siemens e.cam dual-head camera with LEHR parallel beam collimators, and (b) Trionix Triad triple-head camera with LEHR fan beam collimators. Courtesy of SUNY Upstate University Hospital.

3.2.2 Data analysis

We characterized the CDRF as a combination of a normalized resolution-response function and a sensitivity function that determines the scaling factor at a given location. Resolution response (Table 3.1) is characterized by Gaussian functions, and the size of the Gaussian radius depends on the distances from a given point source to collimator d , and to the central axis ρ . The farther away the point source of activity lies from the detector, the worse is the spatial resolution. The sensitivity function (Table 3.2) represents the total number of photons detected by the gamma camera per unit activity at a given location. The sensitivity factor is shift dependent for a fan-beam collimator, and is modeled as a parabolic function of the distance to collimator d and the distance to the central axis ρ . For a parallel beam collimator, the sensitivity

of the gamma camera does not vary significantly with position. Therefore, the value is calculated as the average of all sensitivity measurements.

Table 3.1. Resolution response (Gaussian radius) as function of point-source distance d (cm) from collimator and ρ (cm) from central axis.

Gamma camera	Resolution function (mm)	R^2
Siemens E.Cam with LEHR parallel-beam collimator	$\sigma_u = 1.86 + 0.124 d + 0.00124 d^2$ $\sigma_v = 1.96 + 0.127 d + 0.00130 d^2$	0.999 0.999
Trionix Triad with LEHR fan-beam collimator	$\sigma_u = 2.13 - 0.245 d - 0.0819 \rho + 0.0328 d^2$ $+ 0.00970 \rho^2 + 0.00831 \rho d$ $\sigma_v = 1.79 + 0.101 d + 0.00129 d^2$	0.976 0.998

Table 3.2. Sensitivity as function of point-source distance d (cm) from collimator and ρ (cm) from central axis.

Gamma camera	Sensitivity (counts·MBq ⁻¹ ·s ⁻¹)	R^2
Siemens E.Cam with LEHR parallel-beam collimator	91.85 ± 0.44	
Trionix Triad with LEHR fan-beam collimator	$51.14 - 0.536 d + 0.393 \rho + 0.0963 d^2 + 0.0060 \rho^2$	0.94

3.3 Standard image quality metrics

In order to quantitatively evaluate the performance of various regularization methods, we implemented both standard image quality measures, and task-based model observers. Note that image quality usually cannot be fully represented by a single metric. Therefore, we carefully

took into consideration many aspects of image quality, including noise, spatial resolution, contrast, and bias.

3.3.1 Spatial variability

Spatial variability is defined as

$$\sigma = \sqrt{\frac{1}{N} \sum_{j=1}^N (f_j - \bar{f})^2} \times 100\%, \quad (3.1)$$

where N is the number of voxels inside the regions of interest, f_j is the voxel value for voxel number j , and \bar{f} is the mean value of f_j .

3.3.2 Uniformity

Uniformity is defined as

$$Uniformity = \frac{\max\{f_j\} - \min\{f_j\}}{\max\{f_j\} + \min\{f_j\}} \times 100\% \quad , \quad (3.2)$$

where j spans a subset of indices of voxels within the volume of interest. The value of uniformity is highly dependent on the original radiotracer distribution. If the voxel values within the volume of interest are supposed to be piecewise constant, then the ideal value of uniformity is zero.

Uniformity is usually evaluated in a piecewise constant background region as an indicator of maximum noise fluctuation.

3.3.3 Local NPS

In this dissertation, noise power spectrum (NPS) is defined as the squared magnitude of the Fourier transform of 2D pure image noise; specifically, we follow the approach described in the relevant ICRU report [51]. A total number of K independent realizations of the same data acquisition process are used to produce K reconstructed images. For these images, the power spectrum of the image averaged over K realizations is subtracted from the mean power spectrum of all K realizations to remove deterministic artifacts resulting from the shape of the original image:

$$W_s = W_t - W_a, \quad (3.3)$$

where W_t is the measured average power spectrum of the n images, W_a is the power spectrum of the averaged image, and the resulting W_s is the NPS of the measured images.

SPECT reconstructed images are known to be non-stationary. Therefore, NPS's are measured in regions of interest instead of the whole cross-section. We characterized the noise performance by means of the normalized LNPS. It has been used to evaluate background noise properties in SPECT [52] [53] and PET [54] iterative reconstruction methods, as well as in the context of CT reconstruction [55, 56].

3.3.4 Spatial resolution

Point spread functions (PSF) have been estimated using reconstructed images of point source projection data. PSF in both radial and tangential directions are evaluated for various algorithms. Due to the non-stationary nature of the reconstructed images, the PSF is position-dependent. Following well-established methods [52, 54, 57], we have introduced a number of

point sources—located in the same transaxial cross-section of the cylinder, but at different radial distances from its central axis—as a perturbation to the background (*i.e.*, target absent) object. We have assumed that the reconstruction operation on such objects is approximately linear. After reconstruction of the perturbed image, the reconstruction of noiseless lumpy background projection data was subtracted to provide the LPSF. Then the FWHMs of LPSFs were calculated, providing an estimate of the local spatial resolution for each SPECT reconstruction method.

3.3.5 Bias

Bias is the average value of percent difference between reconstructed images and the ground truth image. Specifically, it is defined as the ℓ_1 norm of the difference image:

$$Bias_j = \sum_{j=1}^N \left\| \frac{f_j - \hat{f}_j}{\hat{f}_j} \right\|_1 \times 100\%, \quad (3.4)$$

where N is the total number of voxels within a defined volume. An alternative definition of bias is as follows [58]:

$$Bias_j = \frac{\left(\sum_{j=1}^N f_j - \sum_{j=1}^N \hat{f}_j \right)}{\sum_{j=1}^N \hat{f}_j} \times 100\%. \quad (3.5)$$

This definition is usually employed for quantification tasks, with the region set to be a specific volume of interest (*e.g.* lesions). For our purpose of evaluating the fidelity of reconstructed images globally, the former definition is more appropriate.

3.3.6 Contrast recovery coefficient

The contrast recovery coefficient (CRC) is defined as:

$$\text{CRC} = \frac{C_{\text{recon}}}{C_{\text{ground truth}}}, \quad (3.6)$$

where $C = \frac{\bar{L} - \bar{B}}{\bar{B}}$, \bar{L} and \bar{B} represent ensemble averaged values of selected “lesion” and background region, respectively. The ideal CRC value is 1 for both hot and cold lesions.

3.3.7 Mean-squared error

The mean-squared error (MSE) is a global image-quality metric. It quantifies the difference between the activity reconstruction f and the phantom (the ground truth activity) \hat{f} in the whole object. It is defined by

$$\text{MSE} = \frac{1}{N} \sum_{j=1}^N (f_j - \hat{f}_j)^2, \quad (3.7)$$

where f_j and \hat{f}_j are activities of voxel j in the reconstructed image and the ground truth image (the phantom), respectively, and N is the total number of voxels in the reconstruction space.

3.4 Model observers

The image metrics above have been widely used to quantify image quality. However, the ultimate task of medical imaging is to present images for diagnostic use, and those metrics do not

always reflect the quality of reconstructed images in terms of lesion conspicuity. Instead, the effectiveness of human observers (radiologists) in detecting and/or quantifying lesions is the ultimate evaluation criterion of image quality. However, it is often unrealistic to obtain statistically solid data from radiologists, due to time and cost considerations. Fortunately, model observers have been proposed to solve this issue. Lesion detection is essentially a classification task. In a nutshell, model observers produce a scalar result, known as the decision variable, for each detection task after being trained with known positive (lesion present) and negative (lesion absent) cases,. Classification is then achieved through thresholding.

3.4.1 Channelized Hotelling observer

Channelized Hotelling observer (CHO) [59-61] has been shown to correlate well with human observer performance in numerous studies [62-65] by simulating the response of the human visual system at various spatial frequencies. The rationale for non-uniform spatial frequency channels is that human visual perception system have different responses to different spatial frequencies [66, 67].

We define the channel vector elements as integrated values of the two-dimensional Fourier-transformed reconstructed images of the signal-absent and signal-present classes within predefined rotationally symmetric band-pass filters (channels). The total number of channels is K , typically between 3 and 16. We define the channeling operator (U) as:

$$\mathbf{c} = \mathbf{U}f, \quad (3.8)$$

and the output \mathbf{c} is vector with components corresponding to various spatial-frequency channels.

Applying the channel model involves taking the Fourier transform of the image, multiplying by each frequency channel, and computing the power. Let \mathbf{c}_0 and \mathbf{c}_1 be the channel vectors of the known signal-absent and signal-present classes, respectively. Then we have:

$$\begin{aligned}\mathbf{c}_0 &= [c_1^0, c_2^0, \dots, c_K^0]^T \\ \mathbf{c}_1 &= [c_1^1, c_2^1, \dots, c_K^1]^T.\end{aligned}\tag{3.9}$$

All channels are designed to have positive values on an $L \times L$ pixel window centered at the lesion location and are normalized. The zero-frequency component of the resulting spatial domain template is explicitly zeroed by subtracting the mean pixel value. The decision variable of the CHO is the prewhitened inner product of a channel vector \mathbf{c} and an observer vector \mathbf{o}_{CHO}^T .

$$\begin{aligned}\mathbf{o}_{CHO} &= (\langle \mathbf{c}_0 \rangle - \langle \mathbf{c}_1 \rangle)^T \mathbf{S}_c^{-1} \\ \lambda(\mathbf{c}) &= \mathbf{o}_{CHO}^T \cdot \mathbf{c} = (\langle \mathbf{c}_0 \rangle - \langle \mathbf{c}_1 \rangle)^T \mathbf{S}_c^{-1} \mathbf{c}\end{aligned}\tag{3.10}$$

where $\langle \bullet \rangle$ denotes the ensemble mean across all realizations in one class.

Prewhitening is performed using the inverse of the average of the intra-class channel covariance matrix \mathbf{S}_c :

$$\mathbf{S}_c = \frac{1}{2}(\mathbf{S}_{c_0} + \mathbf{S}_{c_1}) = \frac{1}{2}(\langle \mathbf{c}_0 - \langle \mathbf{c}_0 \rangle \rangle \langle \mathbf{c}_0 - \langle \mathbf{c}_0 \rangle \rangle^T + \langle \mathbf{c}_1 - \langle \mathbf{c}_1 \rangle \rangle \langle \mathbf{c}_1 - \langle \mathbf{c}_1 \rangle \rangle^T),\tag{3.11}$$

where $\langle \bullet \rangle$ is the ensemble average and μ_0 is mean value of channel vector over ensemble,

N is the number of noise realizations of channel vectors. In our studies, sub-images in the

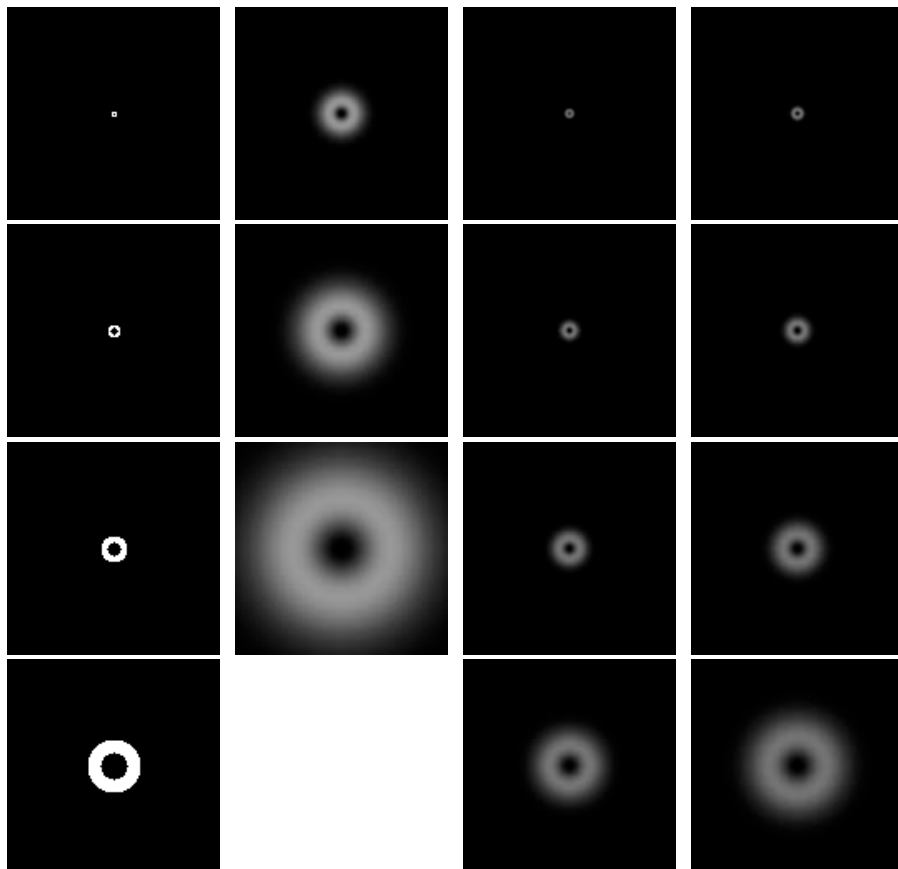
location of possible lesions were chosen, and assessed using CHO for lesion detectability

analysis. Due to the limitations of computational load, our ensemble size was set to 100, *i.e.* we

reconstructed images from 100 noisy projection data sets for each class (lesion-present and lesion-absent).

3.4.2 Channel selection

Various channel selections were used in our studies, as shown in Fig.4.3, including square response (SQR), sparse difference of Gaussians (S-DOG), and dense difference of Gaussians (D-DOG). We implemented three channel selection models in a similar fashion to the study by Abbey and Barrett [61].



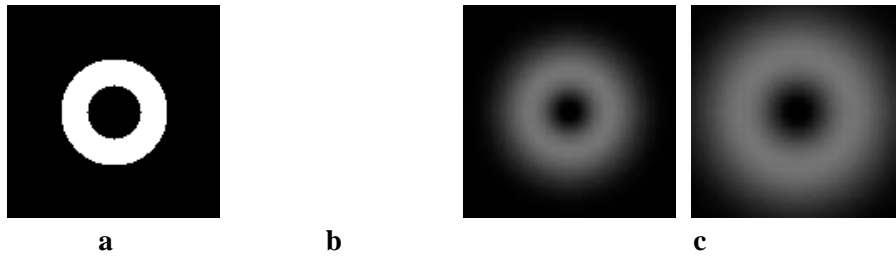


Fig. 3.3. CHO bands in frequency domain: (a) SQR (b) S-DOG (c) D-DOG.

See text for frequency selections.

Square channels (Fig.3.3a) are rotationally symmetrical, non-overlapping band-pass filters, described by:

$$C_k(\rho) = \begin{cases} 1 & \rho \in (\rho_0 \alpha^{k-1}, \rho_0 \alpha^k] \\ 0 & \text{otherwise} \end{cases} \quad (3.12)$$

where ρ is the spatial frequency, $\alpha > 1$ defines the channel width, $k \in [1, K]$ represents the channel index, and K is the total number of channels.

Difference-of-Gaussian (DOG) channel selection (Fig. 3.3b,c) is another commonly used model. It incorporates overlapping, radially symmetric functions into channel response functions. The k^{th} DOG channel is characterized by:

$$C_k(\rho) = \exp\left[-\frac{1}{2}\left(\frac{\rho}{Q\rho_0\alpha^k}\right)^2\right] - \exp\left[-\frac{1}{2}\left(\frac{\rho}{\rho_0\alpha^k}\right)^2\right], \quad k \in [1, K] \quad (3.13)$$

where ρ , α , and k are spatial frequency, channel width, and index of this channel. $Q > 1$ denotes the bandwidth of the channel. We used the same configuration for these parameters as in [61].

We implemented a sparse difference-of-Gaussian (S-DOG) model and a dense difference-of-

Gaussian (D-DOG) model. Specifically, for S-DOG, $\rho_0 = 0.015$, $\alpha = 2.0$, $Q = 2.0$, and $K = 3$; and for D-DOG, $\rho_0 = 0.005$, $\alpha = 1.4$, $Q = 1.67$, and $K = 10$.

3.4.3 Internal noise

The responses of CHO to lesions are usually more accurate than those of well-trained radiologists, resulting in high lesion detectability results. Therefore, internal noise was introduced to model the other factors involved in evaluating images. When tuned properly, it allows quantitative comparison between human observer and CHO. It has also been pointed out that although internal noise is only one term, it is an approximate model for all the factors that may contribute to the fluctuation of human observer outputs. There are several ways to introduce internal noise to model observers. It can be introduced to channel output or added directly to decision variables.

When the CHO is used for evaluating performance of different regularization methods, the addition of internal noise usually does not change the ranking; it only changes the relative scale of lesion detectability to approximate human observer output.

3.4.4 CHO lesion detectability

The image quality metric of CHO is called CHO detectability d_A , and if $\lambda(c_1)$ and $\lambda(c_0)$ are independent and Gaussian distributed, then d_A is simply the SNR of CHO decision variables $\lambda(c_1)$ and $\lambda(c_0)$. The CHO lesion detectability index d_A is thus calculated as

$$d_A = \frac{|\langle \lambda(c_1) \rangle - \langle \lambda(c_0) \rangle|}{\sqrt{\frac{1}{2}(\sigma^2(\lambda(c_1)) + \sigma^2(\lambda(c_0)))}} \quad (3.14)$$

where σ^2 denotes sample variance across all noise realizations. Note that in this scenario, only a fraction of the data are used to train the observer, and the rest are used for decision-variable calculations. Alternatively, if no decision variable output is necessary, the SNR of CHO observer can also be calculated using the whole dataset:

$$d_A = (\langle c_1 \rangle - \langle c_0 \rangle)^T \cdot S_c^{-1} \cdot (\langle c_1 \rangle - \langle c_0 \rangle), \quad (3.15)$$

where $\langle c_1 \rangle$ and $\langle c_0 \rangle$ are the mean channel output of known positive cases and known negative cases, respectively. S_c , as defined in equation (4.5), is the intra-class covariance matrix.

The standard error estimation for the lesion detectability is given by Abbey *et al* [68] in the following form:

$$\sigma_{d_A}^2 = \frac{2}{\sigma^2(\lambda(c_1)) + \sigma^2(\lambda(c_0))} \left[\frac{\sigma^2(\lambda(c_1))}{N_1} + \frac{\sigma^2(\lambda(c_0))}{N_0} + \frac{\left(\frac{d_A}{2}\right)^2}{\sigma^2(\lambda(c_1)) + \sigma^2(\lambda(c_0))} \left(\frac{\sigma^4(\lambda(c_1))}{N_1 - 1} + \frac{\sigma^4(\lambda(c_0))}{N_0 - 1} \right) \right] \quad (3.16)$$

where N_1 and N_0 are the number of realizations for the positive and negative cases, respectively.

Chapter 4. Implementation and evaluation of various regularization methods for iterative reconstruction

4.1 Post filtering

A convenient way of resolving the problem of increased noise caused by the EM algorithm is to apply post-reconstruction low-pass filters, such as Butterworth and Gaussian filters. In effect, reduction of spatial variability in reconstructed images is achieved by taking weighted averages in the spatial domain. The filtered results can be interpreted intuitively—the larger the filter size, the smoother the image. Another key advantage of this method is its flexibility: the post-filtering process does not require much computation time, and one can vary filter parameters to get optimal results within reasonable time. However, this method fails to take advantage of prior knowledge of the image smoothness in the iterative reconstruction process. As a result, this method does not have the best noise-spatial resolution tradeoff.

4.2 Iterative regularization methods

As discussed in Chapter 2, maximum *a posteriori* (MAP), (or penalized maximum likelihood, equivalently), reconstruction criterion relies on penalizing unlikely solutions to the reconstruction problem by imposing prior knowledge of radiotracer distribution. Various regularizers deal with each voxel independent of neighboring voxels. The advantage of this approach is that algorithms can be easily derived in closed form based on the EM algorithm. It

has been shown that these methods can perform better than a pure EM algorithm in terms of convergence speed and stability.

A Gaussian regularizer is proposed on the assumption that the radiotracer distribution obeys Gaussian statistics and the mean value of every voxel is known [69, 70]. The regularizer has the form:

$$U(f) = \frac{1}{2} \langle f - f^*, \mathbf{H}(f - f^*) \rangle, \quad (4)$$

where \mathbf{H} is a diagonal matrix with its non-zero elements representing relative weighting factor for individual voxels. Gamma prior [44] and maximum entropy [71-73] have also been proposed to achieve similar goals.

While these spatially independent regularization methods demonstrate better noise-resolution tradeoff, compared with post-reconstruction filters, their uses are limited by two key disadvantages. First, prior knowledge of the image is required, which is often unfeasible. Second, penalizing individual voxels with an inaccurate estimate often results in increased image bias. Therefore, spatially dependent regularizers are now more commonly used instead.

4.3 Total variation-based regularization methods

Total variation (TV), introduced by Rudin, Osher and Fatemi [74] for noise removal, shows great properties as a regularizer, by providing strong noise suppression while preserving edges. It has been established as a popular choice for regularizing ill-posed inverse problems in general.

4.3.1 Total variation

TV regularization was introduced to SPECT reconstruction by Panin *et al* [32]. The TV regularizer can be written as:

$$\lambda \int_{\Omega} |\nabla f| dx \quad (4.1)$$

where ∇ denotes the discrete spatial gradient, and the integral is actually a simple summation.

TV can also be denoted as $\varphi(z)$, as in equation (2.27) with

$$\varphi(z) = \sum_{i=1}^d \left\| [z_i, z_{d+i}, z_{2d+i}]^T \right\| \quad (4.2)$$

and

$$B = \begin{bmatrix} I_q \otimes I_p \otimes D_p \\ I_q \otimes D_p \otimes I_p \\ D_q \otimes I_p \otimes I_p \end{bmatrix}, \quad (4.3)$$

where $d = p \times p \times q$ is the total number of voxels in the reconstruction domain.

$$D_\alpha = \begin{bmatrix} 0 & & & & \\ -1 & 1 & & & \\ & & \ddots & \ddots & \\ & & & -1 & 1 \end{bmatrix} \quad (4.4)$$

The components of the vector $y = \text{prox}_{\mu^{-1}\varphi}(z)$ can then be calculated by:

$$\left\| [y_i, y_{d+i}, y_{2d+i}]^T \right\| = \max \left\{ \left\| [z_i, z_{d+i}, z_{2d+i}]^T \right\| - \frac{1}{\mu}, 0 \right\} \frac{\left\| [z_i, z_{d+i}, z_{2d+i}]^T \right\|}{\left\| [z_i, z_{d+i}, z_{2d+i}]^T \right\|} \quad (4.5)$$

The proximity operator of the indicator function also has closed form expression:

$$\left(\text{prox}_Y(x) \right)_i = \max \{ x_i, 0 \} . \quad (4.6)$$

Besides TV, there are two other commonly used regularization terms in SPECT reconstruction: quadratic and Huber function. Quadratic regularization, as first proposed by Tikhonov, is a classic regularization methods, with the form of:

$$\varphi(z) = \sqrt{\sum_{i=1}^d \left\| \begin{bmatrix} z_i \\ z_{d+i} \\ z_{2d+i} \end{bmatrix} \right\|^2} . \quad (4.7)$$

The Huber function was proposed to solve a spatial resolution problem of the quadratic regularizer [75]. This function, represented by equation (5.8), is quadratic when the differences between neighboring voxels are lower than a given threshold.

$$\varphi(z) = \begin{cases} \frac{1}{2} \sqrt{\sum_{i=1}^d \left\| \begin{bmatrix} z_i \\ z_{d+i} \\ z_{2d+i} \end{bmatrix} \right\|^2}, & |z| \leq \delta \\ \delta \sum_{i=1}^d \left\| \begin{bmatrix} z_i \\ z_{d+i} \\ z_{2d+i} \end{bmatrix} \right\| - \frac{\delta^2}{2}, & |z| > \delta \end{cases} . \quad (4.8)$$

Huber function-regularized ML reconstruction images demonstrate some improvements over a quadratic function in terms of avoiding loss of spatial resolution near edges. However, both of these functions have been shown to be inferior in terms of noise suppression capability, compared with TV [76].

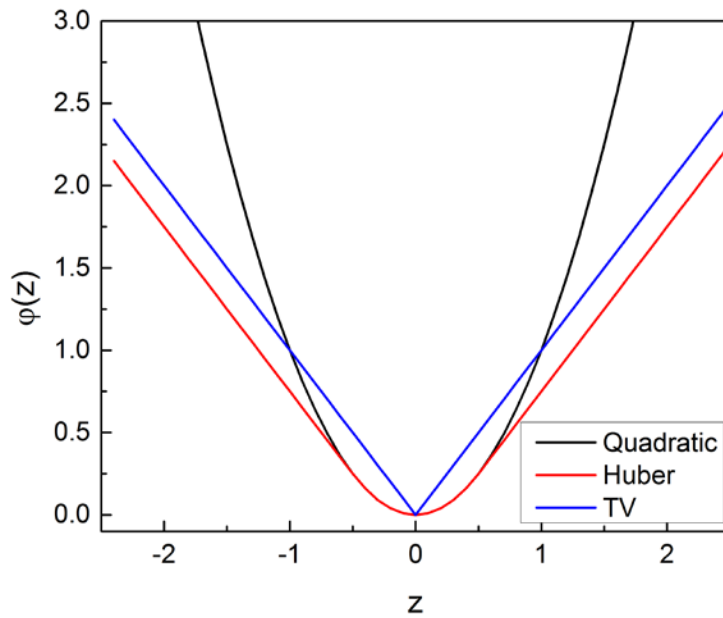


Fig. 4.1. Comparison of TV regularization term with Huber and quadratic regularization functions.

The reason for the desirable properties of TV can be explained by looking at the function $\varphi(z)$. In the objective function (2.27), we minimize KL divergence and $\varphi(z)$ at the same time. The slope of $\varphi(z)$ at z reflects the strength of the regularization at a certain neighborhood difference values. Fig. 4.1 shows that the quadratic regularizer penalizes heavily when z is large, or when the difference between neighboring voxels is large. Therefore, sharp edges, corresponding to large z values are strongly discouraged. In contrast, the TV regularizer penalizes edges much less than quadratic regularizer does. Huber regularization is a compromise between TV and quadratic regularizers. It is capable of retaining the edge-preserving properties of TV but unlike TV, it is differentiable. However, the threshold value δ needs to be optimized for

each image to achieve a good balance between TV and quadratic. Moreover, the relatively steep slope near zero for TV, although it contributes to staircase artifacts, is effective in reducing small noise fluctuations.

4.3.2 High order total variation

The potential disadvantage for TV is that it tends to force smooth images into piecewise constant images with edges, resulting in cartoon-like image features commonly known in image processing field as “staircase” artifacts. High-order regularization terms have been introduced to reduce that artifact.

The straight forward way is to directly add a high-order term into the regularization function. This approach will be referred to as HOTV in the rest of the dissertation. HOTV has been proved effective in various image processing tasks, for example in studies of Benning *et al* [77], and Chan *et al* [78].

$$\lambda_1 \int_{\Omega} |\nabla f| dx + \lambda_2 \int_{\Omega} |\nabla \cdot (\nabla f)| dx \quad (4.9)$$

We used HOTV as a regularizer, and thoroughly evaluated its performance in terms of noise suppression, artifact reduction, and lesion detectability [79].

In the case of the HOTV regularizer, minimization of both first- and second-order derivatives of an image forces a compromise between piecewise-constant and piecewise-linear solutions. Consequently, it results in solutions with substantially reduced staircase artifacts, compared with the first order TV regularizer alone.

For the ICTV functional, the philosophy is different. The first term is small if f_1 is piecewise constant, while the second term is small when f_2 is piecewise linear. Thus, f_1 images

have the appearance of TV-regularized reconstructions, with sharp edges and piecewise-constant regions, while f_2 images resemble HOTV reconstructed images, with smoother estimated radiotracer distribution. Accordingly, the application of infimal convolution to the ECT inverse problem regularization is equivalent to the decomposition of the solution image f into a linear combination $f = \alpha f_1 + (1-\alpha)f_2$ of two images, where image f_1 captures the piecewise-constant components with sharp edges, and image f_2 captures smoother, piecewise-linear regions. Further, both f_1 and f_2 are non-negative.

In the present study, for the purpose of simplification of the evaluation process, we fixed the ratio of penalty weights, $\lambda_1/\lambda_2 = 1$.

4.3.3 Infimal-convolution total variation

Another approach of reducing staircase artifacts due to TV regularization is to combine first order TV with higher order TV via infimal convolution. This approach, which we denote by ICTV, was first introduced as a regularizer in [80]. We introduced and evaluated its performance [81] in SPECT image reconstruction.

In the case of the HOTV regularizer, minimization of both first- and second-order derivatives of an image forces a compromise between piecewise-constant and piecewise-linear solutions. Consequently, it results in solutions with substantially reduced staircase artifacts, compared with the first-order TV regularizer only.

Table 4.1. Regularizers TV, HOTV, and ICTV.Here ∇ represents first-order difference matrix.

	φ	B	f
TV	ℓ_1 norm	∇	f
HOTV	ℓ_1 norm	$\begin{pmatrix} \nabla \\ -\nabla^T \nabla \end{pmatrix}$	f
ICTV	ℓ_1 norm	$\begin{pmatrix} \nabla & \\ & -\nabla^T \nabla \end{pmatrix}$	$\begin{pmatrix} f_1 \\ f_2 \end{pmatrix}$

For the ICTV functional, the philosophy is different. The first term has a small value if f_1 is piecewise constant, while second term is small when f_2 is piecewise linear. Thus, f_1 images have the appearance of TV-regularized reconstructions, with sharp edges and piecewise-constant regions, while f_2 images resemble HOTV reconstructed images, with smoother estimated radiotracer distribution. Accordingly, the application of infimal convolution to the emission CT (ECT) inverse problem regularization is equivalent to the decomposition of the solution image f into a linear combination $f = \alpha f_1 + (1-\alpha)f_2$ of two images, where image f_1 captures the piecewise-

constant components with sharp edges, and image f_2 captures smoother, piecewise-linear regions. Further, both f_1 and f_2 are non-negative.

The main justification for using ICTV functional as a regularizer for SPECT reconstruction is its flexibility and adaptiveness. ICTV allows an image to have both piecewise linear components and piecewise constant components. Instead of enforcing a single penalty criterion, *e.g.* piecewise constant, on the whole image f , only a fraction of the f that fits the piecewise constant criterion better is subject to this penalty term, and the other component of the image is penalized by a criterion that requires smoothness. The decomposition of activity distribution estimate f into f_1 and f_2 is decided locally. Hence, in theory, this regularization works better in images with regions of very different characteristics, *e.g.* parts of the image are very smooth while other parts of the image have sharp edges. Moreover, the ICTV functional is convex, so the uniqueness of the solution is preserved.

4.3.4 Experimental design

In this study, we used numerous Monte Carlo-simulated projection sets to evaluate the performance of these regularization methods. We also tested our reconstruction algorithms using anonymized clinical data.

4.3.4.1 Numerical phantom

We created a numerical cylinder (Fig. 4.2a,c,e) with diameter 20.8 cm and length 14.1 cm, containing two sets of Gaussian spheres with standard deviation varying from 4 to 9 mm (FWHM ranging from 9.4 to 21.15 mm). The six Gaussian spheres in the same set share the

same maximum activity. One set of spheres has more activity than the other set (1.5:1). The background of the cylinder is produced by Gaussian-blurring point sources generated by random vector generator (Fig. 4.2b,d,f), as described in [79]. In addition, we created a reference cylinder with the same lumpy background activity, but without any spheres or point sources.

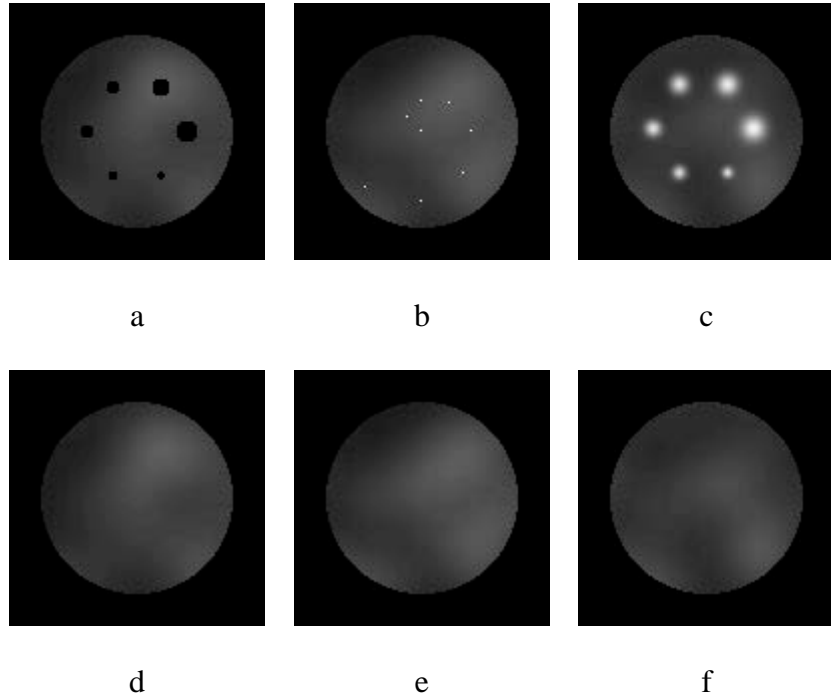


Fig. 4.2. Trans-axial cross-sections of a phantom with: (a) 6 cold (no activity) piecewise-constant spheres with radii of 4, 5, 6, 7, 8, and 9 mm, (b) 8 point sources with maximum-activity-to-mean-background ratio of 100:1 at different radial distances from the central axis of the phantom, (c) 6 hot Gaussian blobs with radii (FWHM) of 4, 5, 6, 7, 8, and 9 mm with maximum-activity-to-mean-background ratio of 3:1 and (d), (e), (f) reference phantom containing warm Gaussian blobs only. Both phantoms were of the size $128 \times 128 \times 128$ voxels, with voxel size set to $2.2 \times 2.2 \times 2.2$ mm³.

4.3.4.2 Simulated SPECT data

We simulated fan-beam SPECT data using SIMIND Monte Carlo simulation package [50]. The focal length of the collimator is set to 43.1 cm. A total of 120 projection views are simulated, each with 128 by 64 detector elements. The detector element size is $2.2 \times 2.2 \text{ mm}^2$. The radius of rotation is set to be 13.0 cm. We use an 18% energy window centered at 140 keV. In the Monte Carlo simulation, only primary photons and first order scattered photons within this energy window are considered. We simulated a total of 9.8×10^8 photon histories to avoid Poisson noise. The Monte Carlo simulated projection images so obtained are multiplied by appropriate constants to reach the total number of counts in 120 views equal to 8.4×10^6 . Based on these data, we use a Poisson random number generator to create 100 different noise realizations for each numerical phantom.

4.3.4.3 Patient data

To test the performance of the reconstruction methods in real clinical applications, we reconstructed anonymized patient projection data. The data consisted of 128 projection views in a 128×100 -dimensional detector matrix with $3.9 \times 3.9 \text{ mm}^2$ pixels. The imaging was performed on a Siemens e.cam SPECT gamma camera with LEHR collimators. Imaging time was set at 20 s per view. A total number of 2.2×10^8 photons were recorded within the selected (20%) energy window. Reconstruction space voxel size was set to $3.9 \times 3.9 \times 3.9 \text{ mm}^3$.

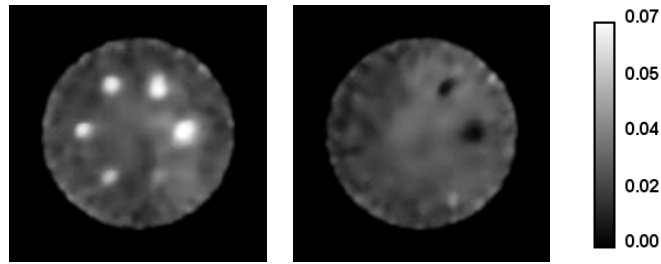
4.3.4.4 Parameter selection

The optimal penalty weight value is obtained by performing sets of trial reconstructions with λ ranging from 10^{-4} to 1 and by analyzing the dependence of spatial resolution and image noise on λ . Spatial resolution can be quantified at the slice with point sources, where the FWHM of the point spread function (PSF) can be easily obtained. We first determine the EMTV hyperparameter λ to be 0.018 by balancing the tradeoff between resolution and image noise. Then we use the same hyperparameter for PAPA, since both methods share very similar objective functions. For PAPA with high-order TV, we keep the λ_1 the same as λ used in first-order TV, and select 0.007 for λ_2 . We also run EM reconstruction with Gaussian post filter as a reference; we select the standard deviation of the Gaussian to be 2.5 mm to achieve similar spatial resolution as in PAPA reconstruction.

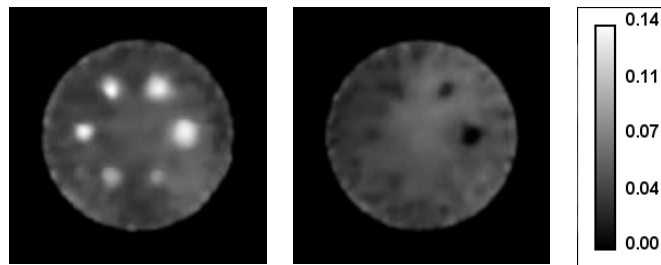
4.3.5 Results and discussion

4.3.5.1 Reconstructed images

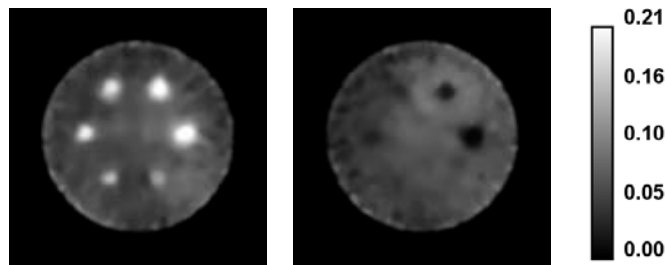
Figure 2 shows images reconstructed for Monte Carlo-simulated SPECT projection data described in Section III.A. All four algorithms were used to reconstruct the simulated 120,000 counts/view (120 kc/view) SPECT projection data. Additionally, the ICTV-PAPA algorithm was used to reconstruct the simulated 40 and 80 kc/view SPECT projection sets.



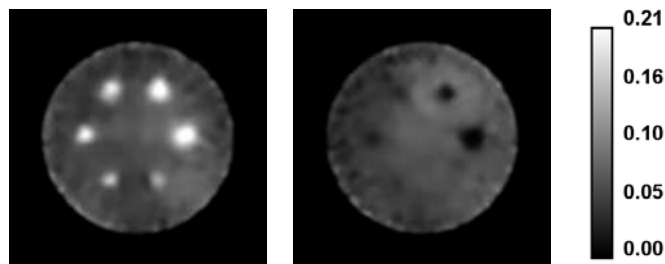
(a) ICTV-PAPA, 40 kc/view, $\lambda_1 = 0.4$, $\lambda_2 = 0.4$



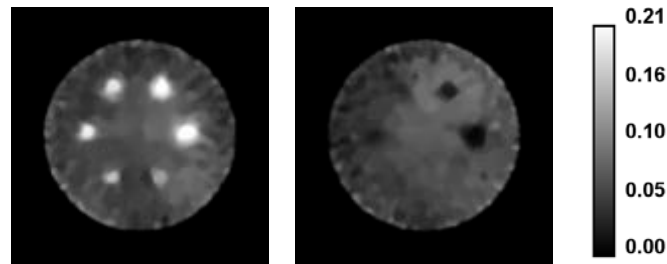
(b) ICTV-PAPA, 80 kc/view, $\lambda_1 = 0.3$, $\lambda_2 = 0.3$



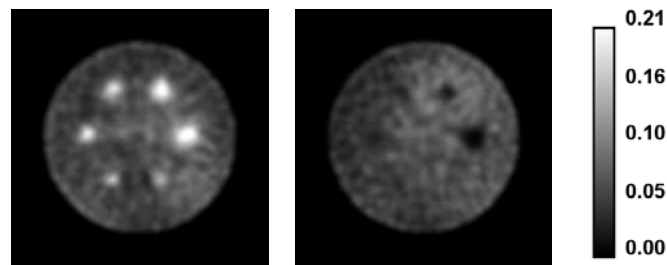
(c) ICTV-PAPA, 120 kc/view, $\lambda_1 = 0.2$, $\lambda_2 = 0.2$



(d) HOTV-PAPA, 120 kc/view, $\lambda_1 = 0.1$ $\lambda_2 = 0.1$



(e) TV-PAPA, 120 kc/view, $\lambda = 0.2$



(f) GPF-MLEM, 120 kc/view, FWHM = 7.3 mm

Fig. 4.3. Transaxial cross-sections of images for Monte Carlo-simulated SPECT data for phantom shown in Fig. 4.2, reconstructed by: (a) ICTV-PAPA for 40 kc/view data, $\lambda_1 = 0.4$, $\lambda_2 = 0.4$; (b) ICTV-PAPA for 80 kc/view data, $\lambda_1 = 0.3$, $\lambda_2 = 0.3$; (c) ICTV-PAPA for 120 kc/view data, $\lambda_1 = 0.2$, $\lambda_2 = 0.2$; (d) HOTV-PAPA for 120 kc/view data, $\lambda_1 = 0.1$, $\lambda_2 = 0.1$; (e) TV-PAPA for 120 kc/view data, $\lambda = 0.2$; and (f) GPF-MLEM using 120 kc/view data, FWHM = 7.3 mm. For all images, the reconstruction was stopped at 100 iterations. Left column: hot spheres with Gaussian activity distribution (see text). Right column: cold spheres with zero activity.

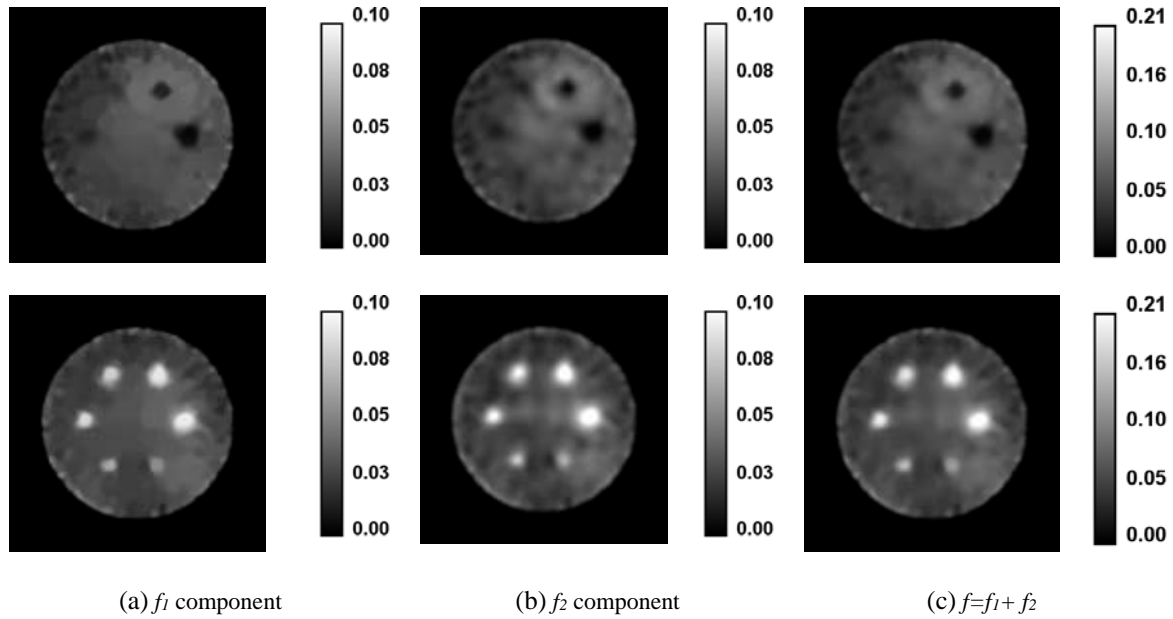
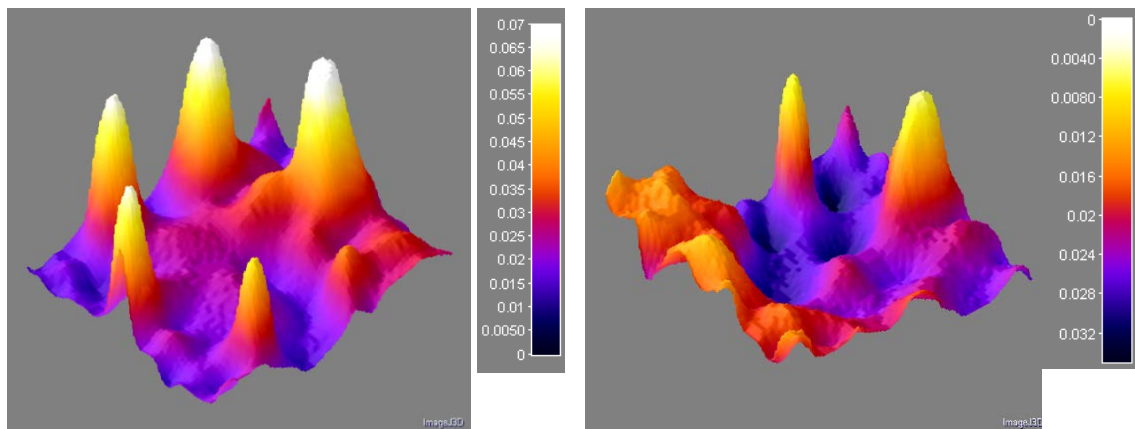
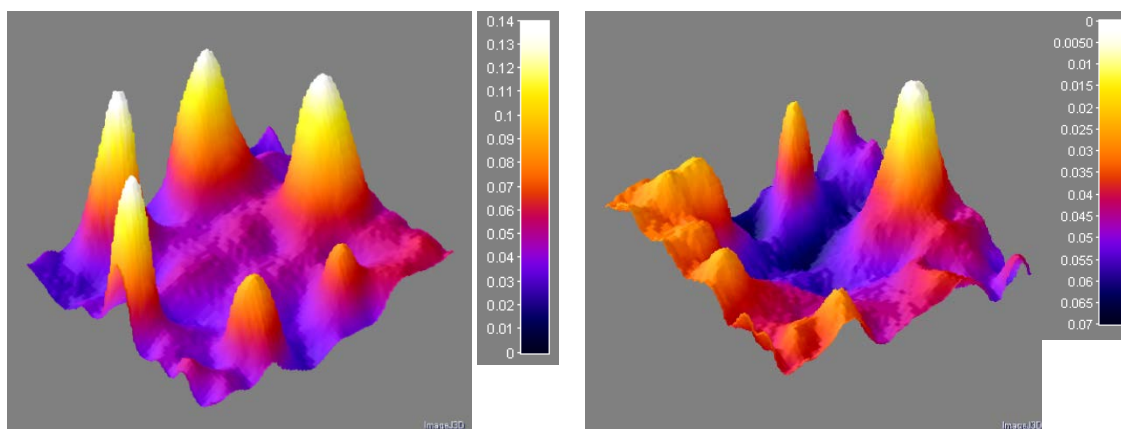


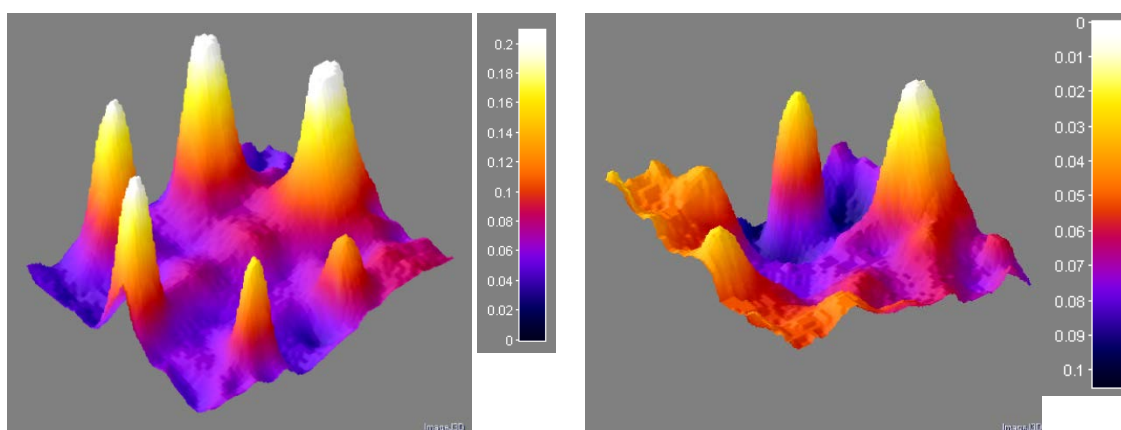
Fig. 4.4. Components of ICTV-PAPA reconstructed images obtained at 100 iterations for simulated SPECT data with 120 kc/view, $\lambda_1 = 0.2$, and $\lambda_2 = 0.2$: (a) f_1 component, (b) f_2 component, and (c) final combined image ($f=f_1+f_2$). Top row: cold spheres with zero activity. Bottom row: hot spheres with Gaussian activity distribution (see Fig. 4.2 and text).



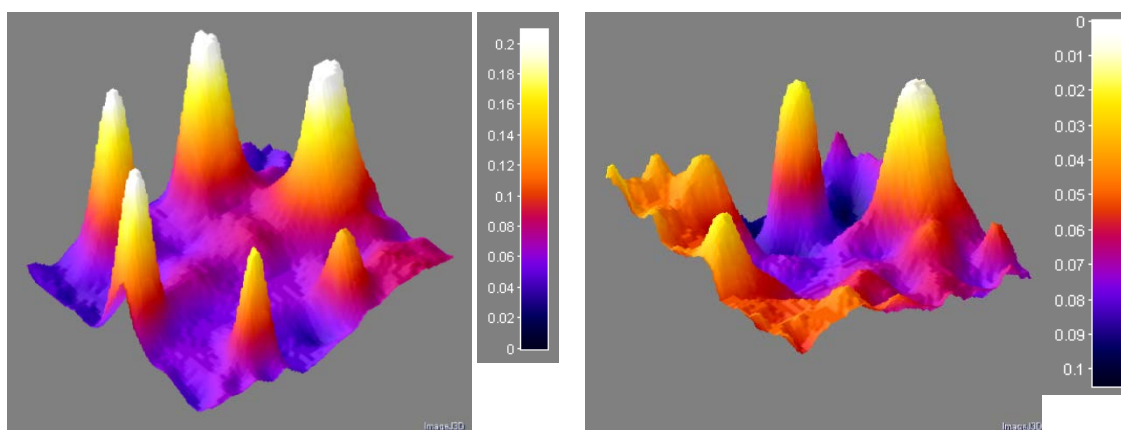
(a) ICTV-PAPA, 40kc/view, $\lambda_1 = 0.4$ $\lambda_2 = 0.4$



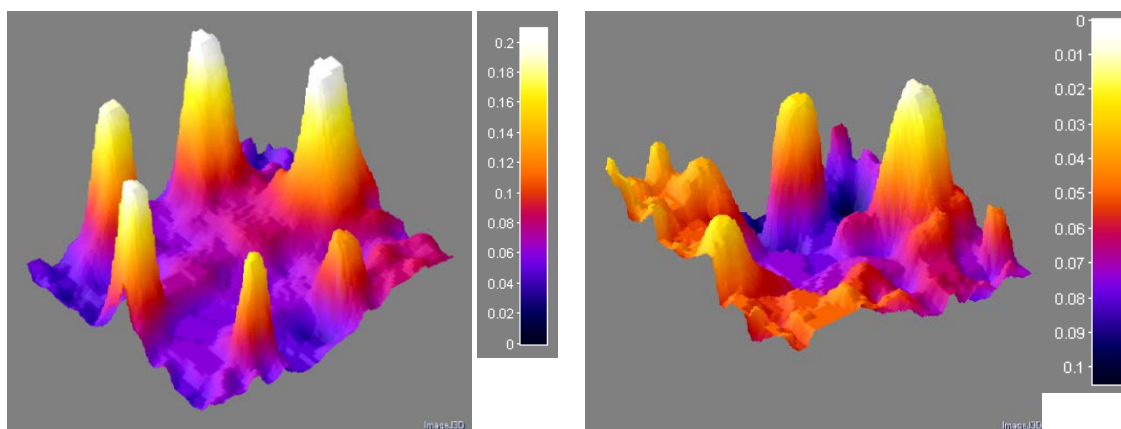
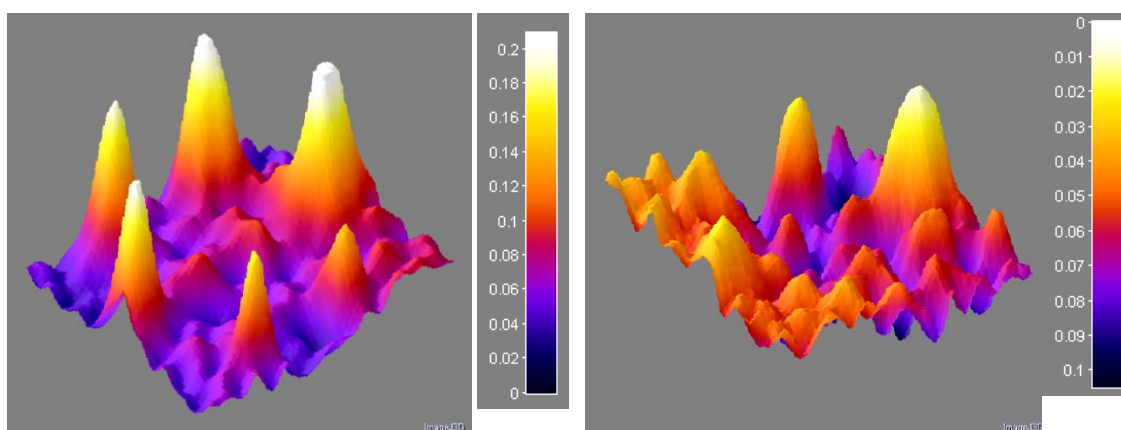
(b) ICTV-PAPA, 80 kc/view, $\lambda_1 = 0.3$ $\lambda_2 = 0.3$



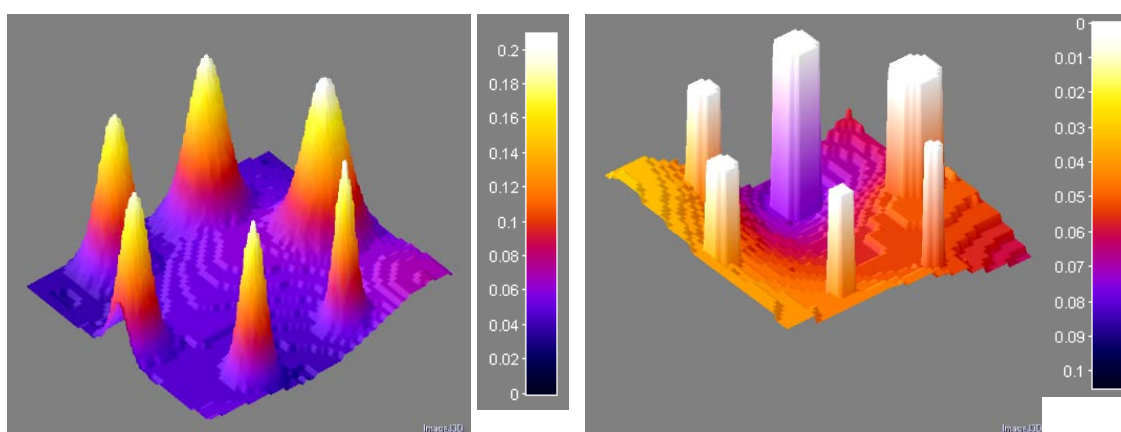
(c) ICTV-PAPA, 120 kc/view, $\lambda_1 = 0.2$ $\lambda_2 = 0.2$



(d) HOTV-PAPA, 120 kc/view, $\lambda_1 = 0.1$ $\lambda_2 = 0.1$

(e) TV-PAPA, 120 kc/view, $\lambda = 0.2$ 

(f) GPF-MLEM, 120 kc/view, FWHM = 7.3 mm



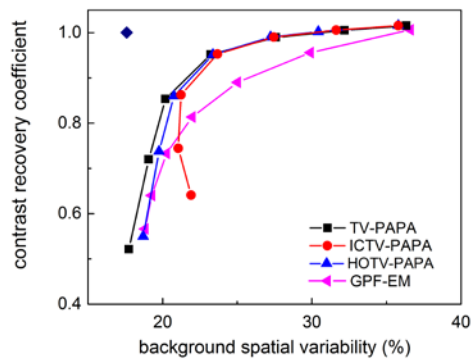
(g) ground truth

Fig. 4.5. Surface plots of: (a) ICTV-PAPA for 40k/view, $\lambda_1 = 0.4$ $\lambda_2 = 0.4$; (b) ICTV-PAPA for 80k/view, $\lambda_1 = 0.3$ $\lambda_2 = 0.3$; (c) ICTV-PAPA for 120k/view, $\lambda_1 = 0.2$ $\lambda_2 = 0.2$; (d) HOTV-PAPA for 120k/view, $\lambda_1 = 0.1$ $\lambda_2 = 0.1$; (e) TV-PAPA for 120k/view, $\lambda = 0.2$; (f) GPF-MLEM for 120k/view, FWHM = 7.3 mm; and (g) ground truth. Left column: hot spheres with Gaussian activity distribution (see text). Right column: cold spheres with zero activity shown in inverted scale.

4.3.5.2 Contrast recovery coefficient (CRC), background variability and bias

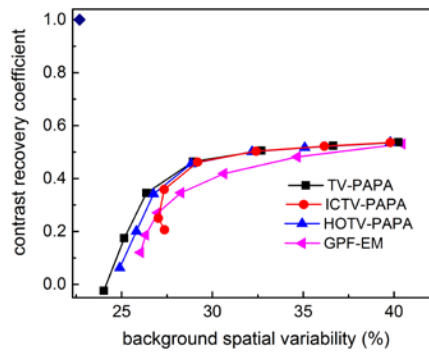
Reconstructions of 10 noise realizations for 120 kc/view simulated SPECT data were performed. Six hot-sphere ROIs and the four largest cold-sphere ROIs were used to estimate mean values of CRC, background variability, and bias (Fig. 4.6). Each point on the curves was calculated for penalty parameters selected in the 0.01–200 range for TV-based algorithms and Gaussian post-filter radii in the 1.1–7.1 mm range for GPF-EM. Only parameters that resulted in reasonable images were selected.

hot spheres

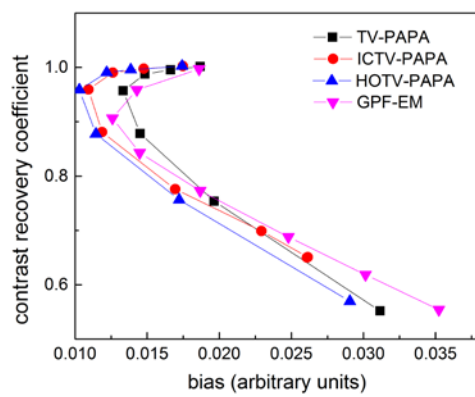


a

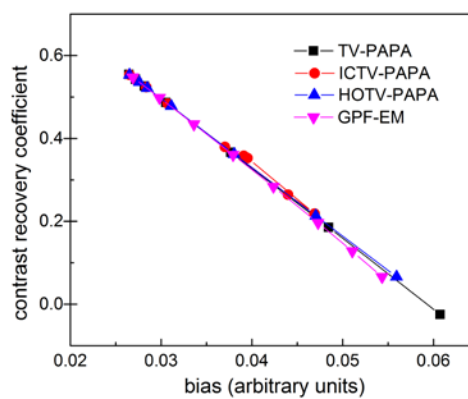
cold spheres



b



c



d

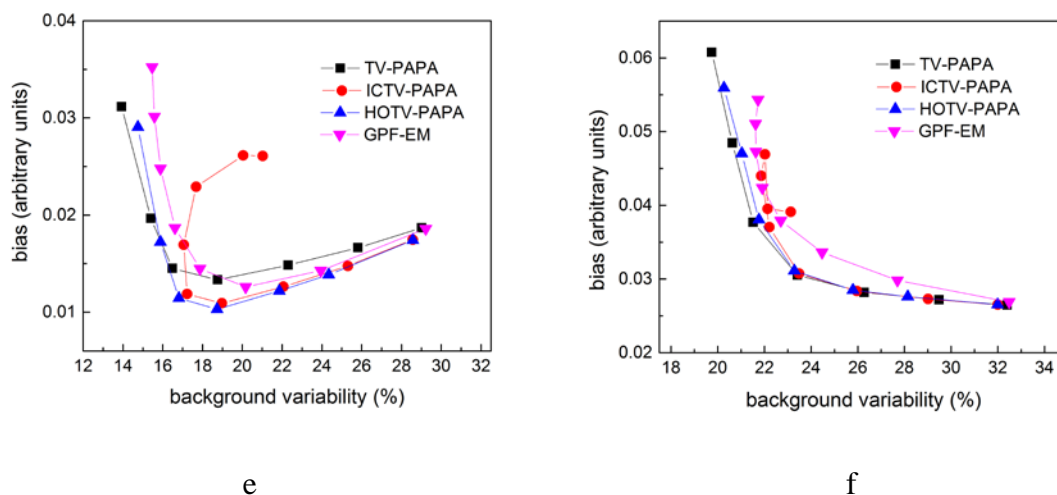


Fig. 4.6. (a) Mean CRC vs. background variability for hot spheres; (b) Mean CRC vs. background variability for cold spheres; (c) Mean CRC vs. bias for hot spheres; (d) Mean CRC vs. bias for cold spheres; (e) Bias vs. background variability for hot spheres; (f) Bias vs. background variability for cold spheres. Each point on the curves was calculated for penalty parameters selected in the 0.01-200 range for TV-based algorithms and Gaussian post-filter radii in the 1.1-7.1 mm range for GPF-EM. Only the four largest spheres were considered among cold spheres. The limiting background spatial variability for selected ROIs is 17.6% for the background in the cross-section with hot spheres, and 22.7% for the cross-section with cold spheres due to the lumpy background. The ideal values of background spatial variability are indicated by solid diamonds and dashed lines.

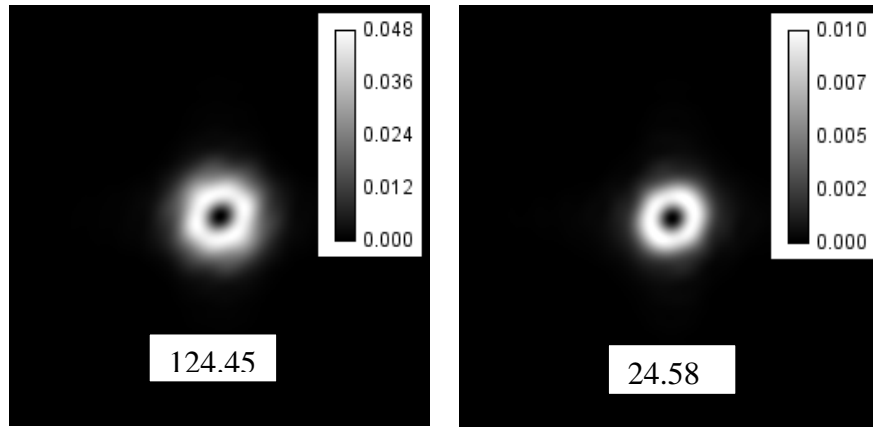
Spatial variability is estimated as the standard deviation of reconstructed activity in the selected background regions averaged over the whole ensemble reconstructions. For the phantoms investigated, the lowest values for spatial variability were 0.0110 (22.7%) and 0.0087 (17.6%) for cold (hot) lesion and background, respectively. The non-zero lowest values of spatial variability were due to background lumpiness. Analysis of Fig. 4.6 shows that all TV-based methods outperform the GPF-EM algorithm in terms of (i) preserving contrast recovery coefficient while reducing the background spatial variability (Fig. 4.6a,b), and (ii) bias-

background variability tradeoff (Fig. 4.6c,d). When penalty parameters or post-filter sizes are reduced to zero, all methods are equivalent to the MLEM algorithm. Therefore, all curves converge to the same points in the plots. Note that ICTV-PAPA-reconstructed images exhibit somewhat anomalous behavior for larger penalty parameters. They never reach the background spatial variability below a particular threshold (17% for hot and 21% for cold spheres, respectively), even when a large smoothing parameter is used and the CRC is decreasing. Further, they never cross certain maximum levels of bias (0.027 for hot and 0.048 for cold spheres, respectively). In contrast, CRC (bias) of TV-PAPA, HOTV-PAPA and GPF-EM decreases (increases) when the background spatial variability decreases.

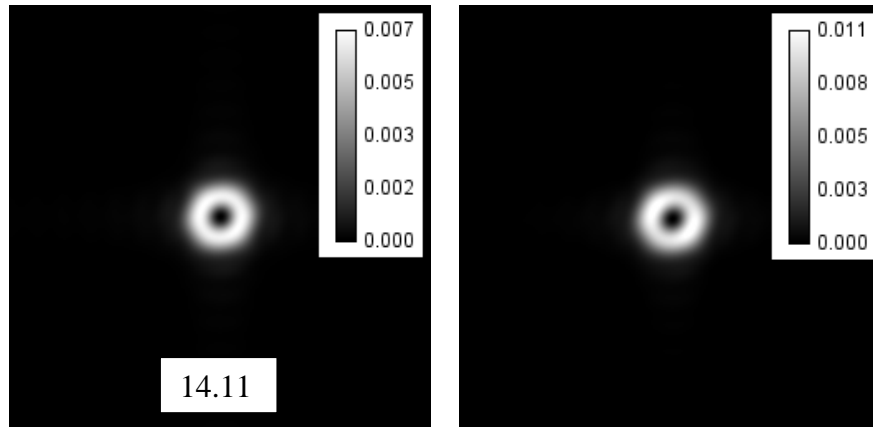
4.3.5.3 Local noise power spectra (LNPS)

We analyzed LNPS using a small ROI located at the isocenter for simulated SPECT data with 120 kc/view. Examples of LNPS are shown in Fig. 4.7 We observe similar “donut” shapes of LNPS for all investigated algorithms. However, the corresponding maximum and sum values are an order of magnitude higher for GPF-MLEM, compared to TV-based algorithms. Examples of average radial profiles though LNPS are shown in Fig. 4.8.

ICTV-PAPA performs somewhat worse than HOTV-PAPA and better than TV-PAPA. The differences can probably be explained by the choice of penalty parameters (Table 1). The full width at half maximum (FWHM) of LNPS for GPF-EM is larger than the FWHM for TV-based algorithms, and does not depend on radial location.



(a) GPF-EM (FWHM=7.3 mm) (b) TV-PAPA ($\lambda = 0.2$)



(c) HOTV-PAPA ($\lambda_1 = 0.1, \lambda_2 = 0.1$) (d) ICTV-PAPA ($\lambda_1 = 0.2, \lambda_2 = 0.2$)

Fig. 4.7. Local noise power spectra (LNPS) obtained for the central location of small ROI: (a) GPF-EM; (b) TV-PAPA; (c) HOTV-PAPA; and (d) ICTV-PAPA all obtained for simulated SPECT data with 120 kc/view. Noise variance values of the selected ROI and penalty parameters are displayed at the bottom of each image.

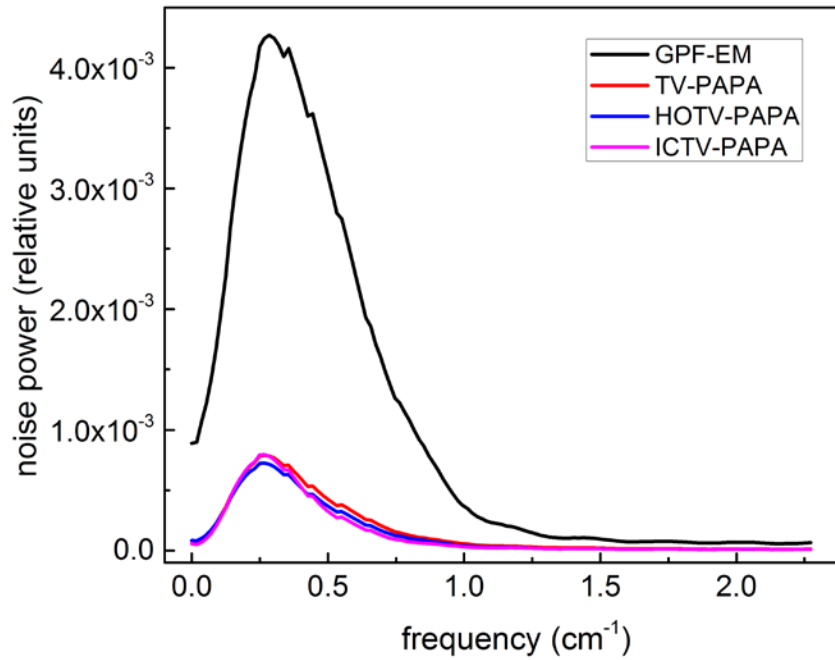


Fig. 4.8. Average radial profiles for local noise power spectra shown in Fig. 4.7. The profiles were obtained by averaging the data every 10° .

Table 4.2. Mean and maximum amplitudes of LNPS obtained for the simulated SPECT data with 120 kc/view

	Mean value of LNPS	Maximum value of LNPS	FWHM
GPF-EM	1.90×10^{-3}	0.0557 at 0.28 cm^{-1}	0.48 cm^{-1}
TV-PAPA	3.75×10^{-4}	0.0182 at 0.27 cm^{-1}	0.37 cm^{-1}
HOTV-PAPA	2.15×10^{-4}	0.0144 at 0.27 cm^{-1}	0.37 cm^{-1}
ICTV-PAPA	3.07×10^{-4}	0.0192 at 0.27 cm^{-1}	0.32 cm^{-1}

4.3.5.4 Channelized Hotelling observer

CHO detectability indices, shown in Figs.4.9 and 4.10, indicate that ICTV-PAPA is capable of providing images with higher conspicuity of hot and cold “lesions,” compared to the GPF-EM algorithm. The CHO signal-to-noise ratio (SNR) obtained for simulated “lesions” at 80 kc/view using ICTV-PAPA is better than CHO SNR obtained for 120 kc/view data using GPF-EM.

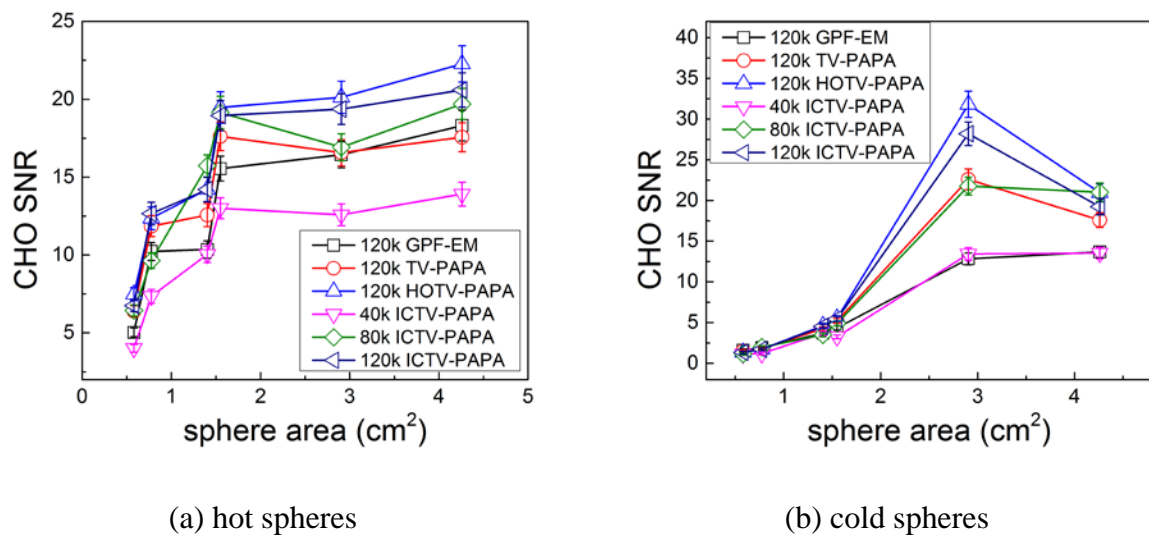


Fig. 4.9. CHO detectability indices of: (a) hot; and (b) cold spheres vs. cross-sectional area of the spheres and vs. number of counts per view in the simulated SPECT data. ICTV-PAPA for 40 kc/view data, $\lambda_1 = 0.4$, $\lambda_2 = 0.4$; ICTV-PAPA for 80kc/view data, $\lambda_1 = 0.3$, $\lambda_2 = 0.3$; ICTV-PAPA for 120kc/view data, $\lambda_1 = 0.2$, $\lambda_2 = 0.2$; HOTV-PAPA for 120kc/view data, $\lambda_1 = 0.1$, $\lambda_2 = 0.1$; TV-PAPA for 120kc/view data, $\lambda = 0.2$; and GPF-MLEM using 120kc/view data, FWHM = 7.3 mm. The reconstructions were stopped at 100 iterations. The solid lines connecting the data points are provided as a visual guide only.

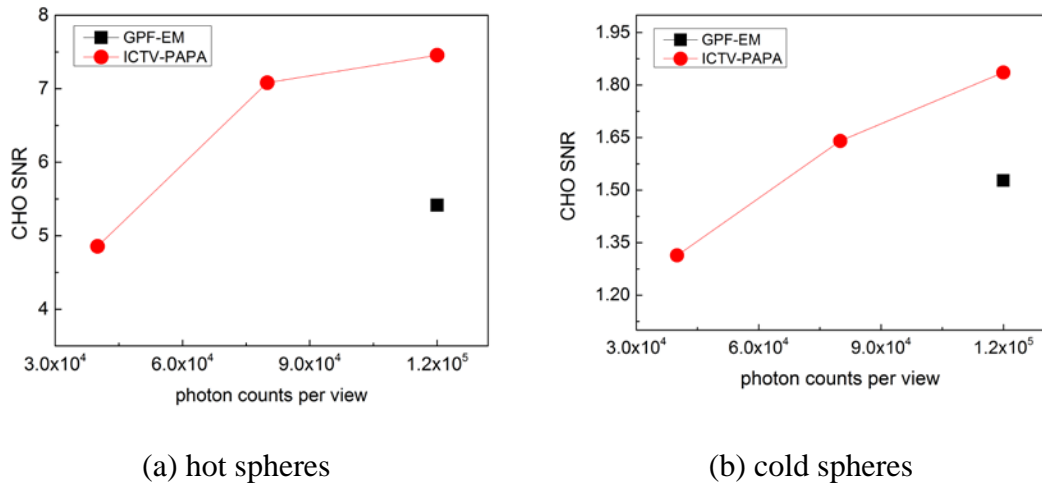


Fig. 4.10. CHO detectability estimated (solid circles) for the fourth largest sphere (1.4 cm² cross-sectional area) for images reconstructed with three photon levels (40, 80 and 120 kc/view) using ICTV-PAPA and GPF-EM (solid squares) at 120 kc/view level.

4.3.5.5 Local point spread function

Plots of local PSF components vs. radial distance are shown in Fig 4.11. The transaxial local spatial resolution improves approximately monotonically with increasing radial distance from the center of the cylindrical phantom towards the edges. The GPF-EM reconstructed images have better spatial resolution near the center of the phantom, while images reconstructed using TV-based methods have better spatial resolution near the edge of the phantom. GPF-EM reconstructed images have more uniform (less steep slope) local spatial resolution throughout the reconstruction space, compared with TV-based algorithms. The tangential LPSF is better than radial LPSF. The actual LPSF strongly depends on selected penalty parameters.

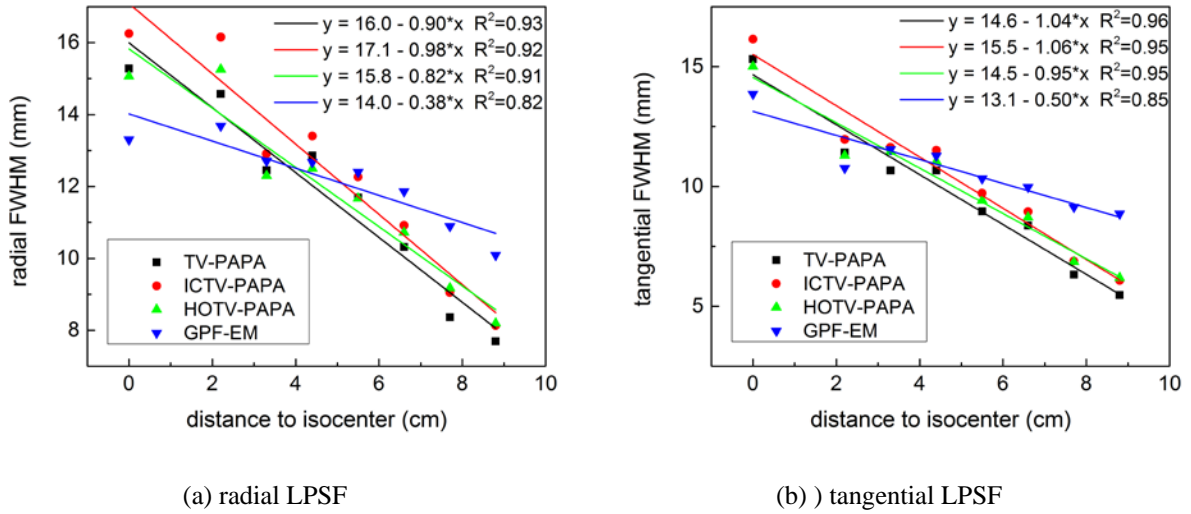
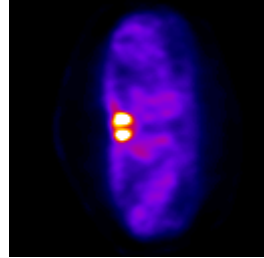


Fig. 4.11. (a) Radial (r) full width at half maximum (FWHM) and (b) tangential (t) FWHM of trans-axial local point spread function (LPSF) as function of radial positions of point sources. The SPECT data were simulated for 120 kc/view. Reconstructions were performed with the following penalty parameters: ICTV-PAPA for 40 kc/view data, $\lambda_1 = 0.4$, $\lambda_2 = 0.4$; ICTV-PAPA for 80kc/view data, $\lambda_1 = 0.3$, $\lambda_2 = 0.3$; ICTV-PAPA for 120kc/view data, $\lambda_1 = 0.2$, $\lambda_2 = 0.2$; HOTV-PAPA for 120kc/view data, $\lambda_1 = 0.1$, $\lambda_2 = 0.1$; TV-PAPA for 120kc/view data, $\lambda = 0.2$; and GPF-EM using 120kc/view data, FWHM = 7.3 mm. Reconstructions were stopped at 100 iterations. The solid lines are linear regression fits.

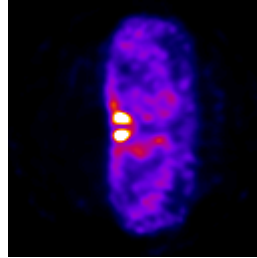
4.3.5.6 Reconstruction of clinical data

To evaluate the performance of the algorithms in a realistic setting, a projection set for a SPECT Tc-99m clinical parathyroid study [82] was reconstructed using all the methods. Analysis of Fig. 4.12 and Fig. 4.13 shows that images reconstructed using TV-PAPA, HOTV-PAPA, and ICTV-PAPA algorithms with optimized penalty parameters all have better local spatial resolution and lower background variability, compared with GPF-EM and clinical OSEM

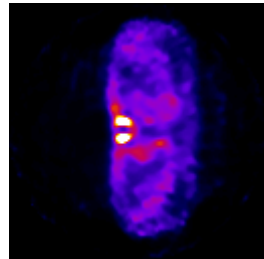
method (HOSEM, by Hermes [83, 84]). Both HOTV-PAPA and ICTV-PAPA reduce staircase artifacts, compared with TV-PAPA.



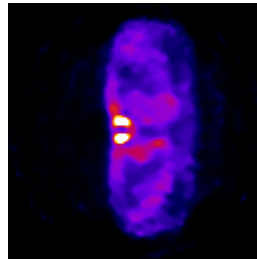
(a) Hermes OS-EM,
16 OS, 5 iterations



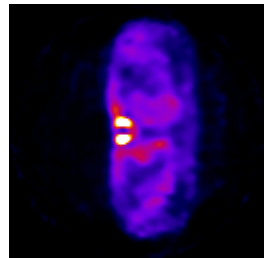
(b) GPF -EM: Gaussian
radius: 3.9mm



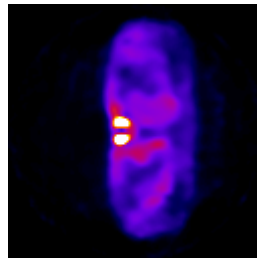
(c) TV-PAPA $\lambda = 0.1$



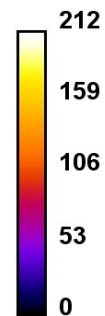
(d) TV-PAPA $\lambda = 0.2$

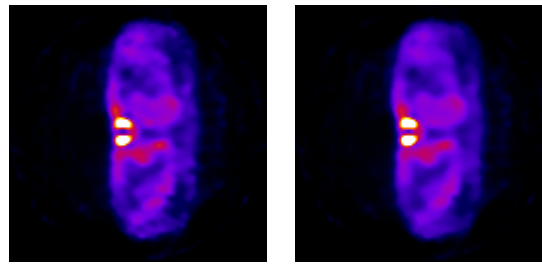


(e) HOTV-PAPA
 $\lambda_1 = 1, \lambda_2 = 1$



(f) HOTV-PAPA
 $\lambda_1 = 2, \lambda_2 = 2$





(g) ICTV-PAPA

(h) ICTV-PAPA

$$\lambda_1 = 2, \lambda_2 = 2$$

$$\lambda_1 = 4, \lambda_2 = 4$$

Fig. 4.12. Trans-axial views of reconstructed images obtained for clinical Tc-99m Sestamibi SPECT parathyroid, late-phase study: Clinical Hermes HOSEM algorithm (a); EM-GPF (b); TV (c, d); HOTV-PAPA (e, f); and ICTV-PAPA (g, h), each with two sets of penalty parameters.

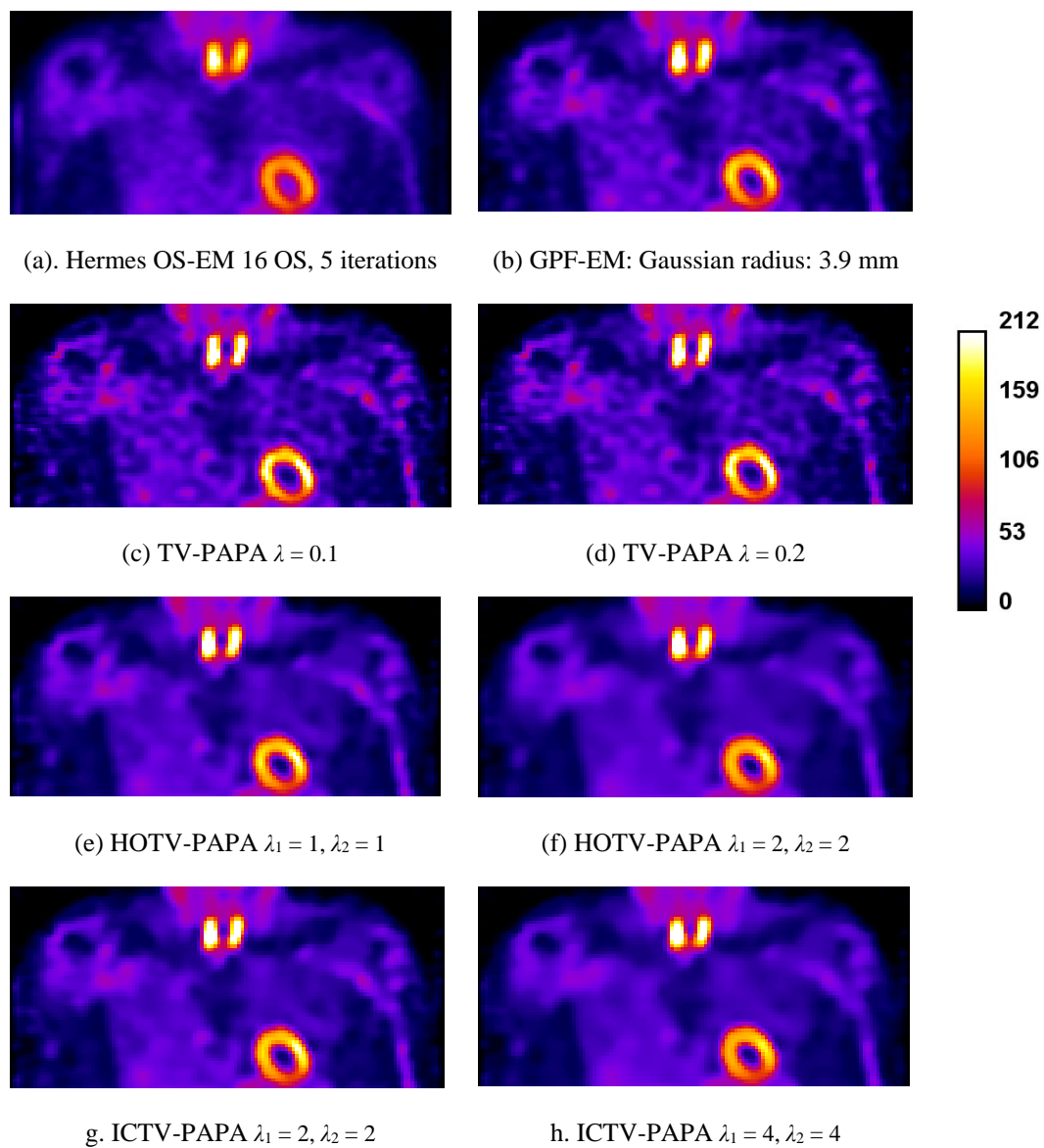


Fig. 4.13. Coronal views of reconstructed images obtained for clinical Tc-99m Sestamibi SPECT parathyroid late-phase study: Clinical Hermes HOSEM algorithm (a); EM-GPF (b); TV (c, d); HOTV-PAPA (e, f); and ICTV-PAPA (g, h), each with two sets of penalty parameters.

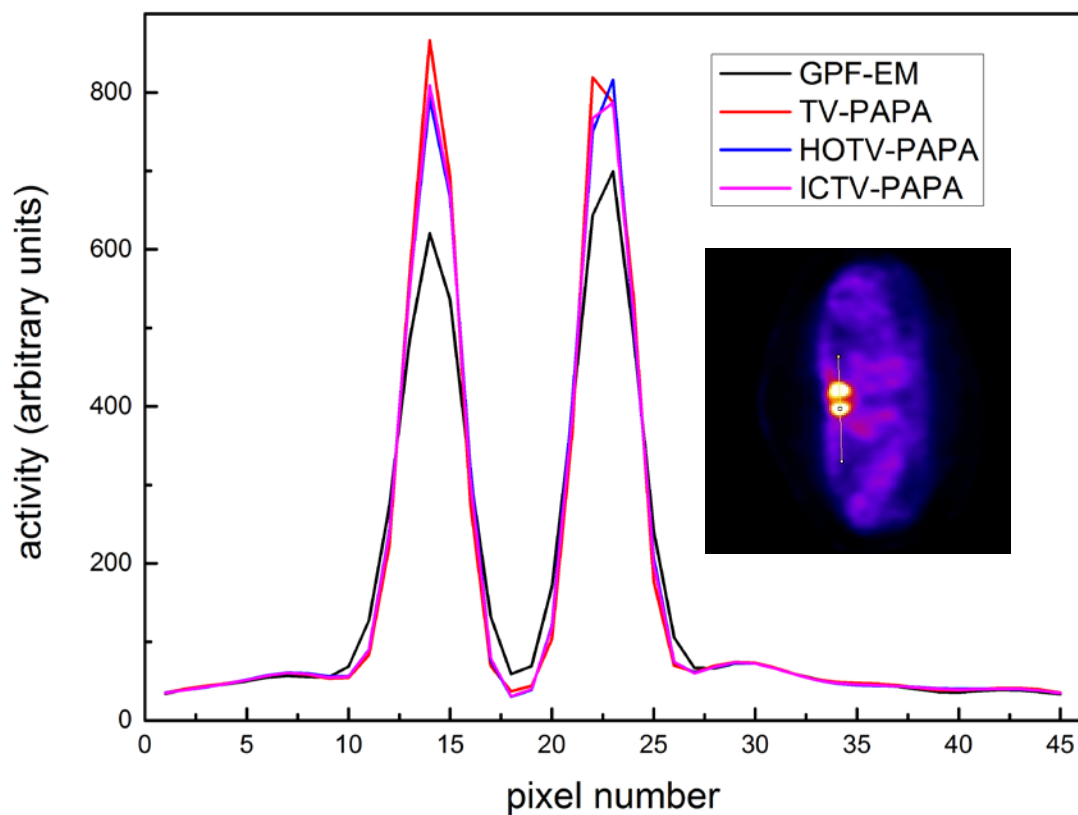


Fig. 4.14. One-channel-wide line profiles through reconstructed transaxial images from the clinical Tc-99m Sestamibi parathyroid scan image shown in Fig. 4.12. The location of the profile is shown in the inset. Penalty weights were set as: TV-PAPA $\lambda = 2$, HOTV-PAPA $\lambda_1 = 1$ $\lambda_2 = 1$, ICTV-PAPA: $\lambda_1 = 2$ $\lambda_2 = 2$.

4.3.6 Conclusions

In our pursuit for a superior regularizer for ECT image reconstruction, we implemented infimal convolution of the first- and second-order gradient TV (ICTV) regularization, using our PAPA algorithm. We investigated the quality of SPECT images reconstructed using ICTV-

PAPA and compared it with quality of images reconstructed with HOTV-PAPA, TV-PAPA, and conventional EM with GPF.

Numerical experiments and initial clinical data reconstructions and analyses indicate that HOTV-PAPA and our new ICTV-PAPA algorithm attained very similar reconstruction performance. Most of the small differences can be explained by the strong dependence of both algorithms on the penalty parameters. Comparing the local noise power spectra (LNPS) showed that both algorithms efficiently suppress the noise, while preserving edges without creating staircase artifacts. The maximum and mean amplitudes of LNPS for TV-based methods for 120 kc/view SPECT data are 5–8 times lower than for GPF-EM. Both HOTV-PAPA and ICTV-PAPA algorithms permit better tradeoff of contrast recovery vs. background variability. Thus, with properly selected parameters, ICTV-PAPA and HOTV-PAPA reconstructed images can simultaneously achieve higher contrast and lower noise (without creating staircase artifacts), compared with GPF-EM or clinical HOSEM. We also found that TV-based methods exhibit better CHO detectability for hot and cold simulated “lesions” of various sizes, compared with GPF-EM. These findings are also confirmed by quantitative analysis of the reconstructed clinical images.

Imaging performance of simulated lower count (higher noise) SPECT data reconstruction using ICTV-PAPA was also investigated. Even with only 67% of the number of photons used in GPF-EM reconstruction, the hot and cold “lesions” CHO detectability in ICTV-PAPA reconstructed images still surpassed GPF-EM CHO detectability, indicating that a 33% radiation dose reduction per patient might be possible.

We conclude that ICTV-PAPA with optimized penalty parameters exhibits noise suppression, local spatial resolution, contrast recovery and lesion detectability comparable to that of HOTV-PAPA and better than that of GPF-EM and clinical OSEM. Consequently, replacing clinical standard reconstruction methods with ICTV-PAPA or HOTV-PAPA could allow reduction of the radiation dose to patients in clinical SPECT studies.

4.4 DCT-induced framelet regularization

Wavelet transforms have been successfully applied to many fields of image processing. Yet, to our knowledge, they have never been directly incorporated in the objective function in emission computed tomography (ECT) image reconstruction before. Our aim was to investigate if the ℓ_1 norm of discrete cosine transform (DCT) wavelet frame transform of the estimated radiotracer distribution could be effectively used as the regularization term in the penalized-likelihood (PL) reconstruction, where a regularizer is used to enforce the smoothness of reconstructed images. In our initial studies, the ℓ_1 norm of 2D DCT wavelet decompositions was used as a regularization term. Our preconditioned alternating projection algorithm (PAPA), proposed in earlier work to solve PL reconstruction with non-differentiable regularizers, was used to solve the optimization problem. The DCT wavelet decompositions were performed on the transaxial reconstructed images and the auxiliary vector \mathbf{b} . We reconstructed Monte Carlo-simulated SPECT data obtained for a phantom with Gaussian blobs as hot lesions and with warm random lumpy background. DCT-induced tight framelet

Framelets have been applied in image deblurring, inpainting, among others [85-88]. Li *et al* first introduced DCT-induced framelets [89] in the context of image deblurring. Here we implemented it as a regularization term in SPECT reconstruction and evaluated its performance [90].

DCT-2 [91, 92] filters were used in this work. Two-dimensional DCT decompositions were calculated on transaxial cross-sections to obtain the regularization term. The elements of the DCT-2 matrix are defined as:

$$\begin{aligned} C_{1,n} &= \frac{1}{\sqrt{N}}, & n &= 1, 2, \dots, N \\ C_{m,n} &= \sqrt{\frac{2}{N}} \left[\cos \frac{(m-1)(2n-1)\pi}{2N} \right], & m &= 2, 3, \dots, N, n = 1, 2, \dots, N. \end{aligned} \quad (4.10)$$

D_m is the matrix representation of the m^{th} row of DCT-2 matrix C_m under the Dirichlet boundary condition. The DCT induced tight framelet transform matrix is formed as:

$$\begin{aligned} B &= [B_1, B_2, \dots, B_{N \times N}]^T, \\ B_{i \times N+j} &= D_i \otimes D_j \otimes I, \quad i, j = 1, 2, \dots, N \end{aligned} \quad (4.11)$$

The regularization term is then formed as:

$$U(\mathbf{f}) = \|\mathbf{Bf}\|_1 \quad (4.12)$$

The PAPA algorithm is subsequently used to solve the optimization problem with the DCT regularization term (DCT-PAPA) [90].

4.4.1 Numerical experiment results and discussion

The ℓ_1 norm of DCT-based wavelet frame transform used as penalty term in (1) is promising as a regularizer in PAPA algorithm. A critical and difficult aspect this method is selection of optimal parameters. As shown in Fig. 4.16, different parameter selections result in very different reconstructed images.

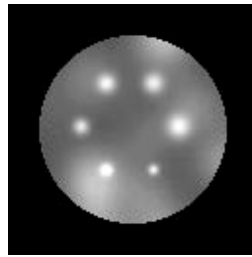
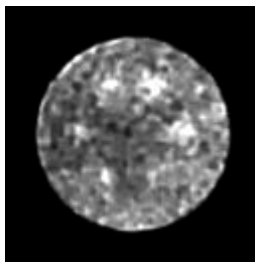
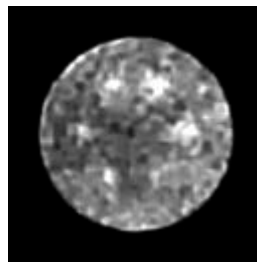


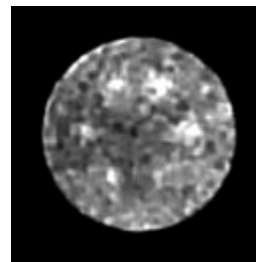
Fig. 4.15. Transaxial cross-section through the synthetic phantom with warm lumpy background and Gaussian blobs as hot lesions ($\sigma = 4, 5, 6, 7, 8,$ and 9 mm; 4:1 activity ratio).



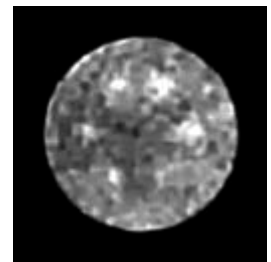
$N=3, \lambda = 0.25$



$N=3, \lambda = 0.30$



$N=3, \lambda = 0.35$



$N=3, \lambda = 0.40$

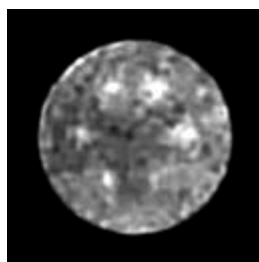
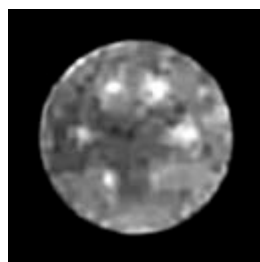
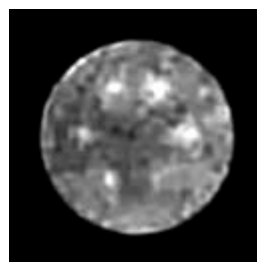
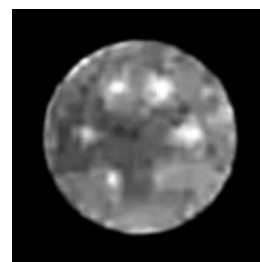
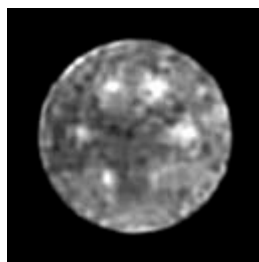
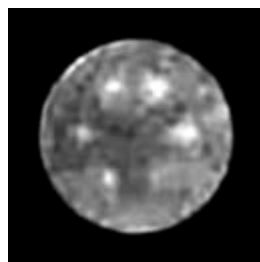
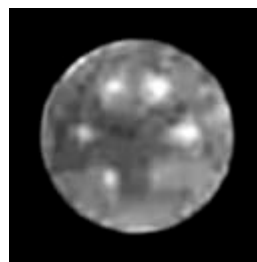
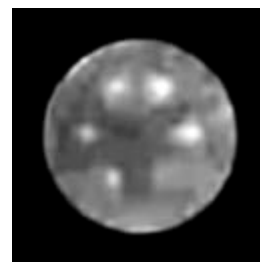
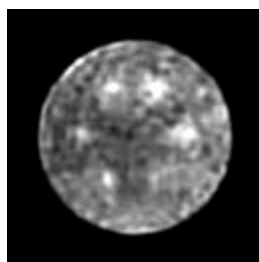
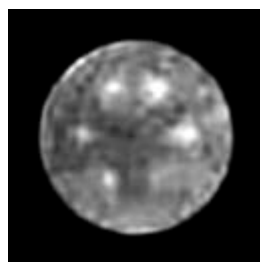
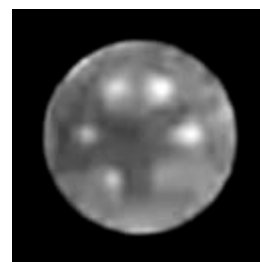
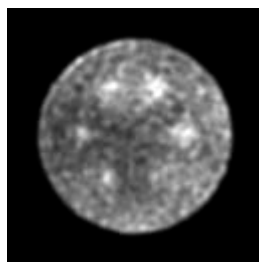
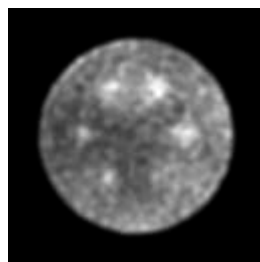
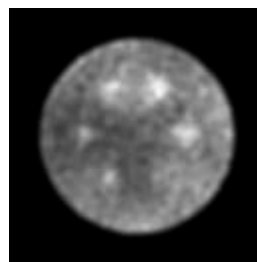
 $N=5, \lambda = 0.20$  $N=5, \lambda = 0.25$  $N=5, \lambda = 0.30$  $N=5, \lambda = 0.35$  $N=7, \lambda = 0.15$  $N=7, \lambda = 0.20$  $N=7, \lambda = 0.25$  $N=7, \lambda = 0.30$  $N=9, \lambda = 0.10$  $N=9, \lambda = 0.15$  $N=9, \lambda = 0.20$  $N=9, \lambda = 0.25$  $\sigma = 2.1 \text{ mm}$  $\sigma = 2.7 \text{ mm}$  $\sigma = 3.3 \text{ mm}$  $\sigma = 3.9 \text{ mm}$

Fig. 4.16. Transaxial cross-section through the reconstructed images with various parameters obtained at 100 iterations. Top four rows are images reconstructed using PAPA-DCT; bottom row are images reconstructed using EM with Gaussian post-filters.

We evaluated the performance of the proposed reconstruction algorithm in comparison with the expectation-maximization (EM) algorithm with Gaussian post-reconstruction filters (EM-GPF). The mean squared error (MSE) values of images reconstructed with these two methods are obtained for various penalty weights.

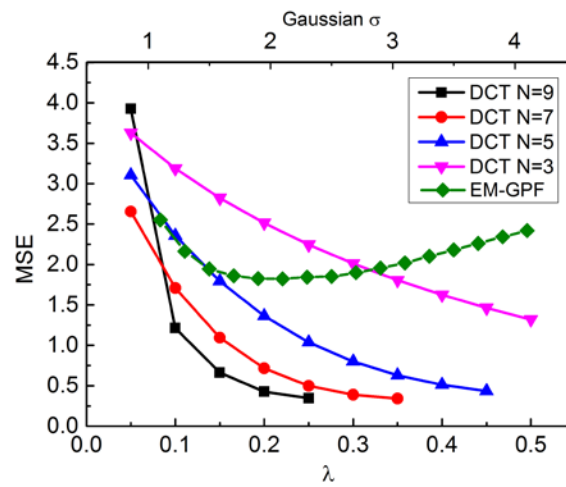


Fig. 4.17. Mean squared error (MSE) curves obtained for images reconstructed using proposed DCT-PAPA method and EM Gaussian post filter (GPF-EM).

4.4.2 Conclusions

Reconstructed images using the proposed method exhibited better noise suppression and improved lesion conspicuity, compared with images reconstructed using expectation maximization (EM) algorithm with Gaussian post filter (GPF). Also the mean squared error (MSE) was smaller than for EM-GPF. A critical but difficult aspect this method is selection of optimal parameters. In summary, our numerical experiments demonstrated that the ℓ_1 norm of discrete cosine transform (DCT) wavelet frame transform DCT regularizer shows promise for SPECT image reconstruction using the PAPA method. To fully exploit the potential of PAPA-DCT method, we are working on improvements of this regularization term, including changing the relative weights of different frequency components, and incorporating 3D instead of 2D regularization.

4.5 Fractional norm

In this dissertation, we also implemented and studied fractional norm-regularized SPECT reconstruction. The algorithm for solving this new optimization problem was closely based on PAPA, with only minor changes to the proximity operators. The fractional norm regularization method was implemented in a 2D MATLAB reconstruction program. Preliminary numerical experiments were conducted for this regularization methods.

4.5.1 Motivation

The ℓ_1 norm regularizer (TV) penalizes the absolute value of the intensity difference between neighbor voxels. At “bright” regions, even when the neighboring voxels have low percentage difference, the absolute difference can still be large and thus will be heavily penalized. In comparison, the ℓ_0 norm does not take into account the absolute value of the difference, and penalizes equally any differences between neighboring pixels. In Fig. 4.18, it is clear that for the ℓ_p norm where $0 < p < 1$, the regularization functions are expected to behave as a compromise between ℓ_0 norm and ℓ_1 norm.

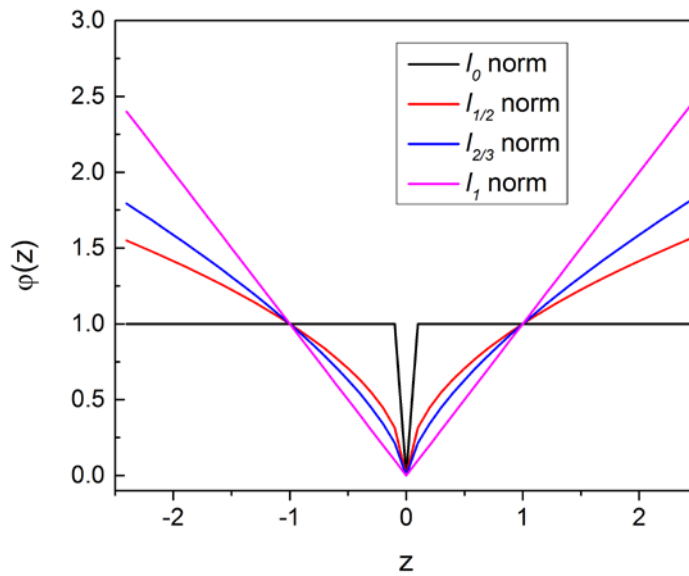


Fig. 4.18. Comparison of $\varphi(z)$ for ℓ_0 , $\ell_{1/2}$, $\ell_{2/3}$, and ℓ_1 norm (TV).

4.5.2 Implementation of fractional norm regularized SPECT reconstruction

The closed forms of proximity operator for $\ell_{1/2}$ norm and $\ell_{2/3}$ norm, as given in [93], are:

$$\text{prox}_{\mu^{-1}\|\cdot\|_{1/2}}(z) = \begin{cases} \{0\}, & \text{if } |z| < \frac{3}{2}\mu^{2/3} \\ \{0, \text{sign}(z) \cdot \mu^{2/3}\}, & \text{if } |z| = \frac{3}{2}\mu^{2/3} \\ \left\{ \frac{2}{3}z \left(1 + \cos \left(\frac{2}{3} \cos^{-1} \left(-\frac{3^{3/2}}{4} \mu |z|^{-3/2} \right) \right) \right) \right\}, & \text{otherwise.} \end{cases} \quad (4.13)$$

$$\text{prox}_{\mu^{-1}\|\cdot\|_{2/3}}(z) = \begin{cases} \{0\}, & \text{if } |z| < 2\left(\frac{2}{3}\mu\right)^{3/4} \\ \{0, \text{sign}(z) \cdot \left(\frac{2}{3}\mu\right)^{3/4}\}, & \text{if } |z| = 2\left(\frac{2}{3}\mu\right)^{3/4} \\ \left\{ \text{sign}(z) \cdot \frac{1}{8} \left(\sqrt{2t} + \sqrt{\frac{2|z|}{\sqrt{2t}} - 2t} \right)^3 \right\}, & \text{otherwise,} \end{cases} \quad (4.14)$$

where

$$t = \left(\frac{1}{16}z^2 + \sqrt{\frac{z^4}{256} - \frac{8\mu^3}{729}} \right)^{1/3} + \left(\frac{1}{16}z^2 - \sqrt{\frac{z^4}{256} - \frac{8\mu^3}{729}} \right)^{1/3}. \quad (4.15)$$

The PAPA algorithm can then be modified accordingly by replacing the proximity operator of ℓ_1 -norm with the proximity operators above. Note that the objective function is no longer necessarily convex. Therefore, the results are not guaranteed to converge to a global maximum. However, when the penalty weight is selected properly, we have observed good consistency in reconstructed images in numerical experiments.

4.5.3 Experimental design

Two numerical phantoms were used to assess the performance of the proposed reconstruction method in comparison to TV-PAPA. The first one, known as Hoffman brain phantom (Fig. 4.19a), is widely used in PET and SPECT studies. The activity ratios of the simulated white/gray matter, ventricles, and background regions in the phantom are 4:1:0. The second phantom is cylindrical with hot spherical “lesions” and lumpy background (Fig. 4.19b). The lumpy background was generated using Gaussian convolved, randomly placed point sources. The hot spheres were also created using Gaussian functions. The peak activities of the hot spheres were the same, and the ratio of peak activity in the spheres to the mean background activity is 2:1.

Both acquisition of projection data and image reconstruction were done using a MATLAB 2D reconstruction program. For both we simulated projections at 128 angles, and the count levels were set to 180,000, corresponding to around 90,000 counts per view in the clinical 128×64 detector elements setting for a 3D phantom.

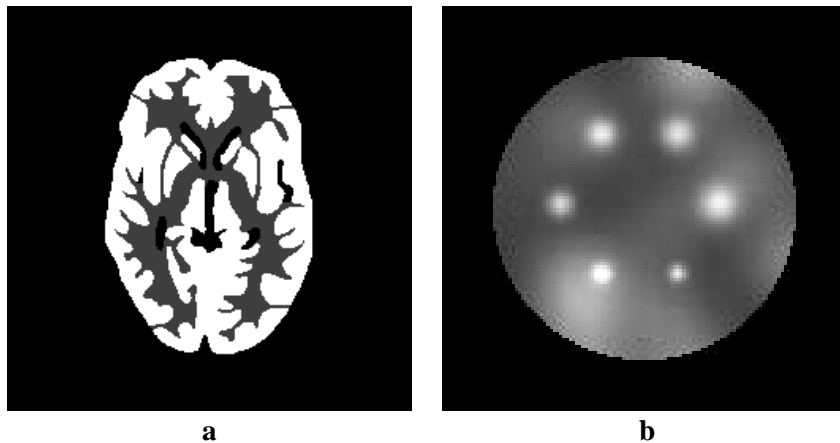
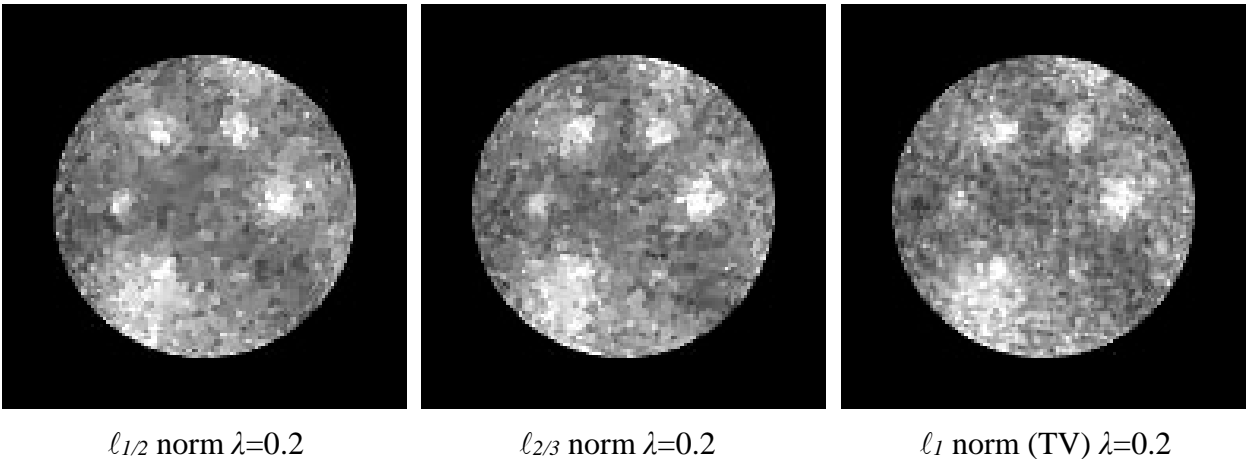
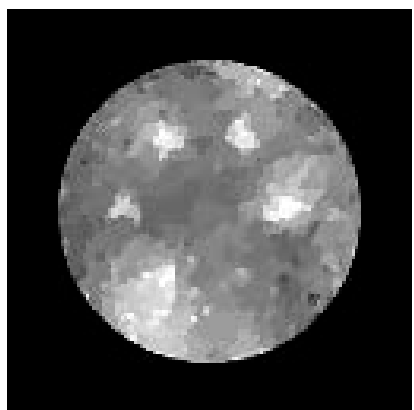
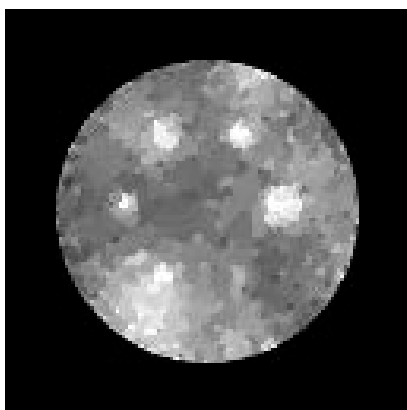
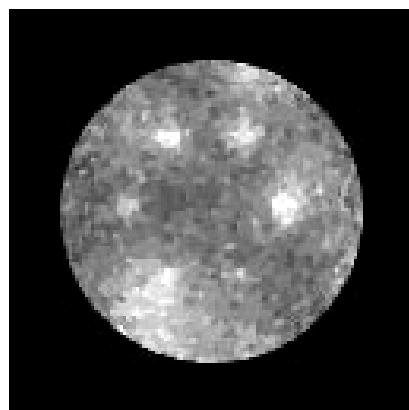
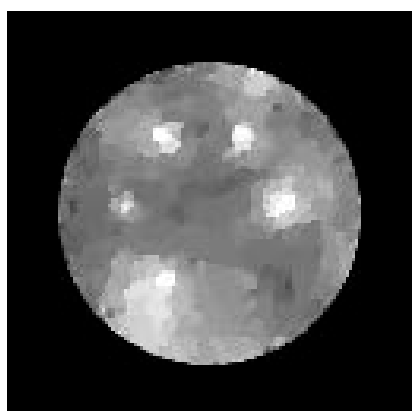
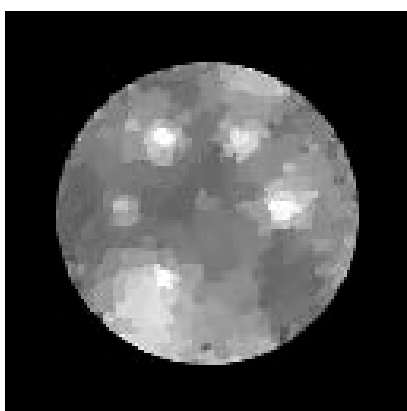
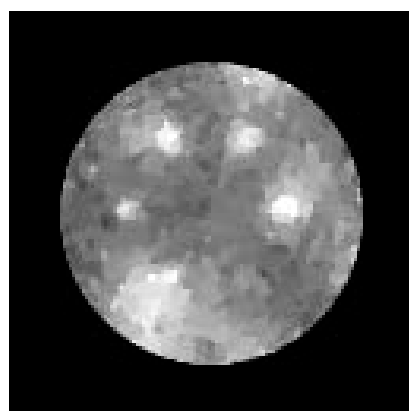
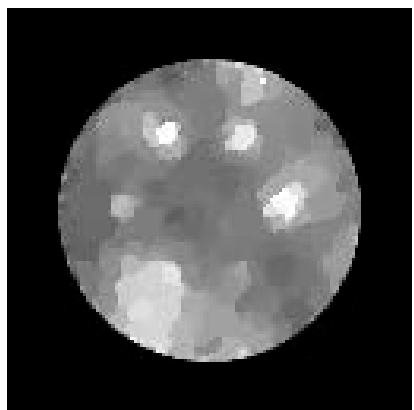
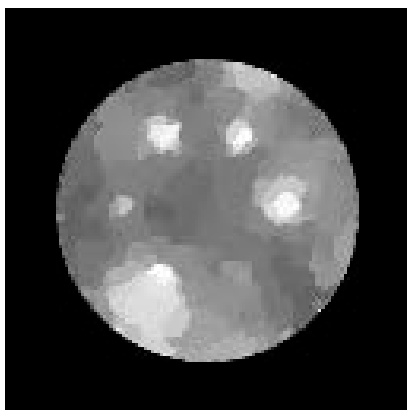
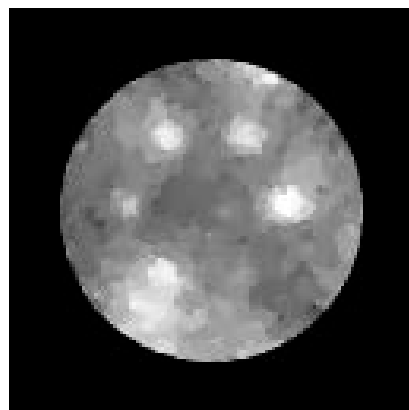


Fig. 4.19. 2D Phantoms used for evaluation of fractional norm-regularized SPECT reconstruction methods: (a) Hoffman brain phantom, (b) Cylindrical phantom with lumpy background and hot spherical “lesions”.

4.5.4 Results and discussion

The reconstructed images from a projection set obtained using the lumpy phantom are shown in Fig. 4.20. Based on the number of visible hot lesions. We selected the optimal penalty weights for $\ell_{1/2}$, $\ell_{2/3}$, and ℓ_1 norm (TV) to be 0.6, 0.8, and 1.0, respectively. It is evident that both $\ell_{1/2}$ norm and $\ell_{2/3}$ norm regularized reconstructions exhibit similar performance to TV in terms of noise suppression and edge preservation. As expected, both fractional norm-regularized reconstruction methods created more pronounced staircase artifacts, (see image profile in Fig. 4.21). Staircase artifacts start to show up in fractional norm-regularized images at lower penalty weight, and the artifacts show up in smaller regions, compared with TV-regularized images.



 $\ell_{1/2}$ norm $\lambda=0.4$  $\ell_{2/3}$ norm $\lambda=0.4$  ℓ_1 norm (TV) $\lambda=0.4$  $\ell_{1/2}$ norm $\lambda=0.6$  $\ell_{2/3}$ norm $\lambda=0.6$  ℓ_1 norm (TV) $\lambda=0.6$  $\ell_{1/2}$ norm $\lambda=0.8$  $\ell_{2/3}$ norm $\lambda=0.8$  ℓ_1 norm (TV) $\lambda=0.8$

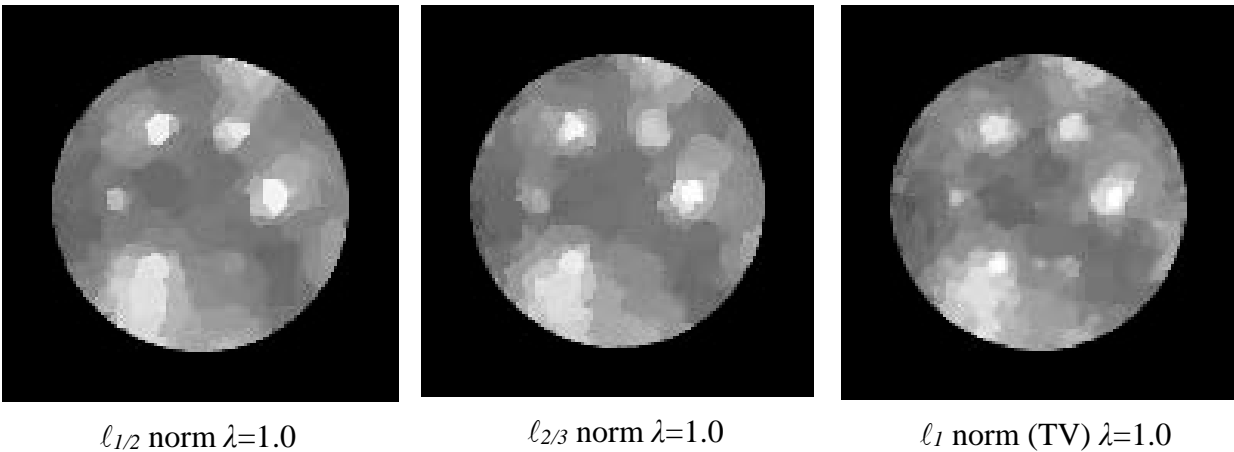


Fig. 4.20. Transaxial cross-section of Hoffman phantom reconstructed by PAPA with $\ell_{1/2}$ norm, $\ell_{2/3}$ norm, and ℓ_1 -norm (TV).

We selected the penalty weights based on the visibility of the hot spheres in reconstructed images. With optimal penalty weights, we observed best image contrast in $\ell_{1/2}$ norm regularized images, followed by $\ell_{2/3}$ norm regularized images (Fig. 4.21). As shown in Fig. 4.22 and Fig. 4.23, $\ell_{2/3}$ norm performed better than $\ell_{1/2}$ norm and TV in terms of RMSE, bias, and $\ell_{1/2}$ norm produces the best contrast recovery coefficient. However, the quality measures depend on penalty-weight selection. Further studies are necessary to take into account the noise-contrast tradeoff with varying penalty weights.

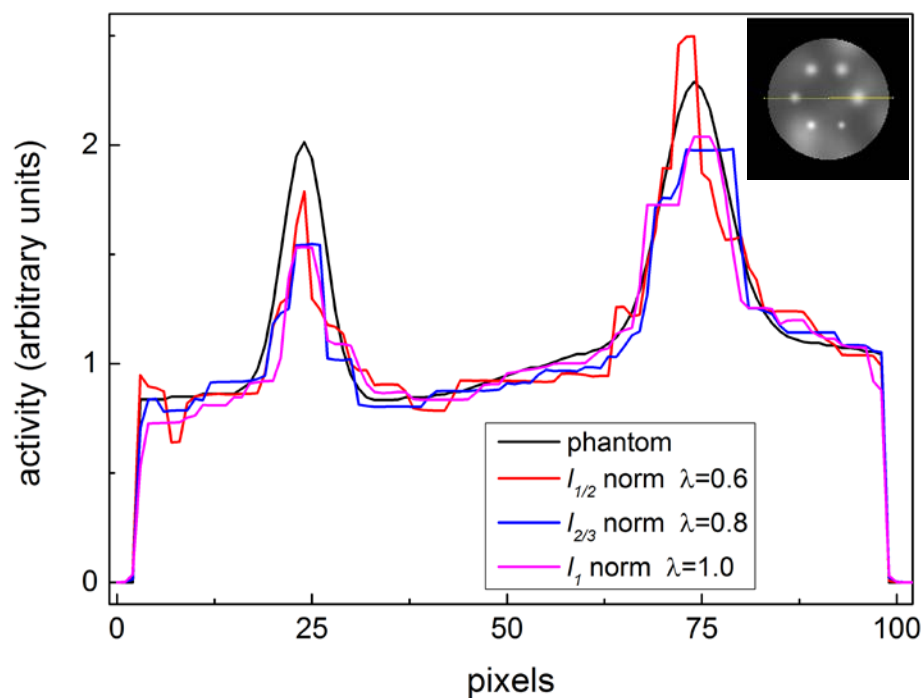


Fig. 4.21. Image profiles of the phantom and reconstructed images with optimal penalty weights. The image profiles were taken horizontally through the center of the image, as indicated by the yellow line in the figure.

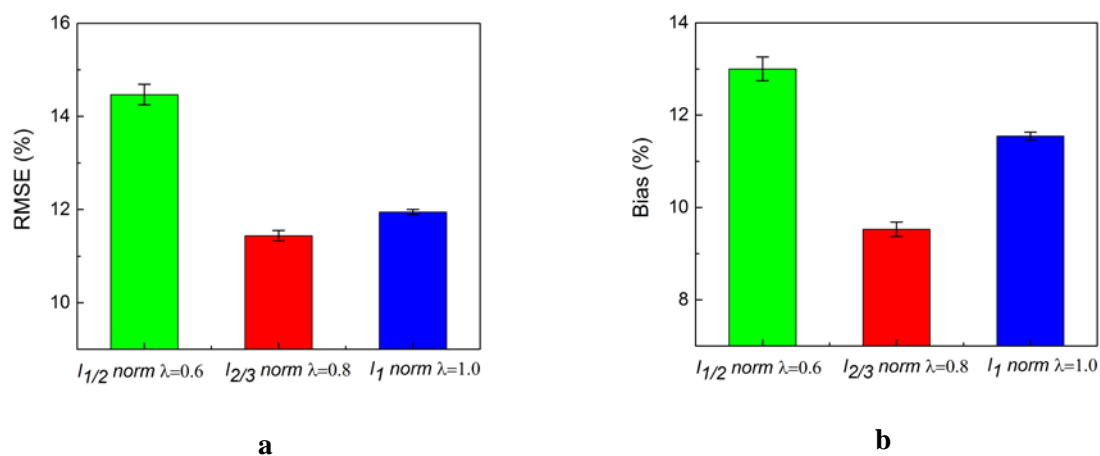


Fig. 4.22. (a) RMSE and (b) bias of reconstructed images of the lumpy phantom with optimal penalty weights selected for each reconstruction methods.

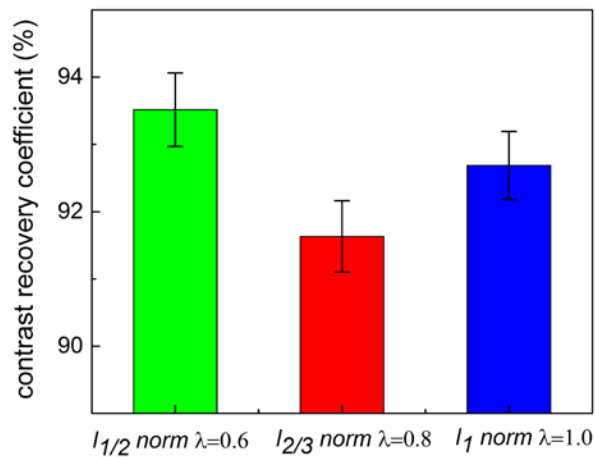
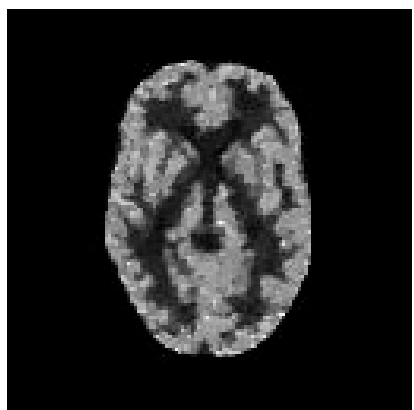
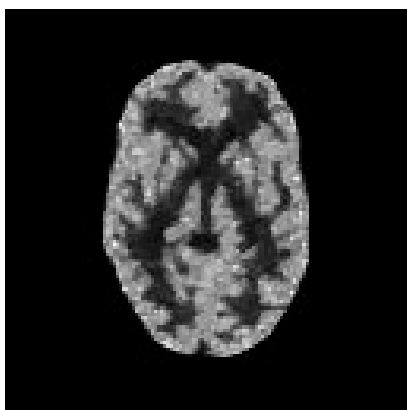
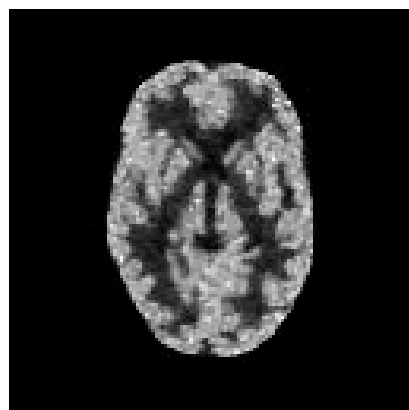
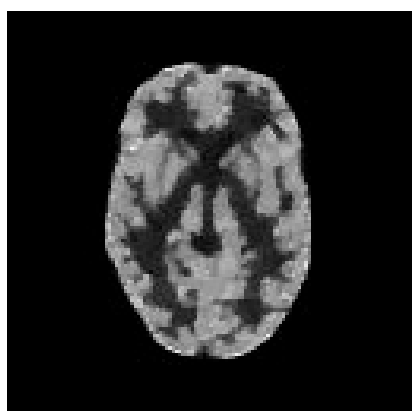
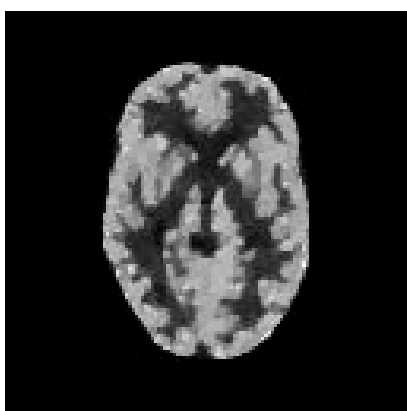
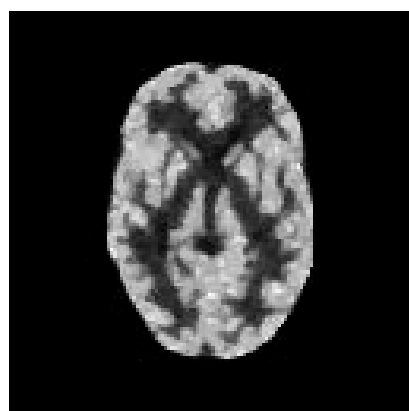
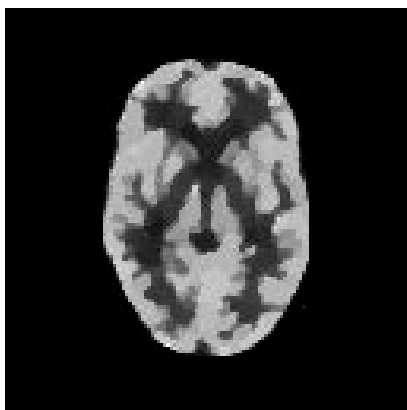
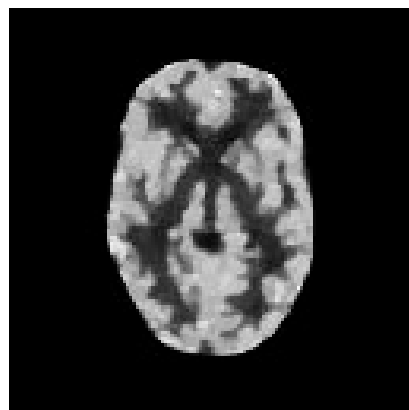


Fig. 4.23. Contrast recovery coefficients of reconstructed hot spheres in the lumpy phantom with optimal penalty weights selected for each reconstruction methods.

To evaluate the performance of these regularization methods in more realistic situations, we performed simulation and reconstruction using the Hoffman brain phantom. Fig. 4.24 shows that reconstructions done with these three methods share similar characteristics. Fractional-norm regularizers require lower penalty weights to reduce the amount of noise variance in reconstructed images, compared with TV.

 $\ell_{1/2}$ norm $\lambda=0.2$  $\ell_{2/3}$ norm $\lambda=0.2$  ℓ_1 norm (TV) $\lambda=0.2$  $\ell_{1/2}$ norm $\lambda=0.4$  $\ell_{2/3}$ norm $\lambda=0.4$  ℓ_1 norm (TV) $\lambda=0.4$  $\ell_{1/2}$ norm $\lambda=0.6$  $\ell_{2/3}$ norm $\lambda=0.6$  ℓ_1 norm (TV) $\lambda=0.6$

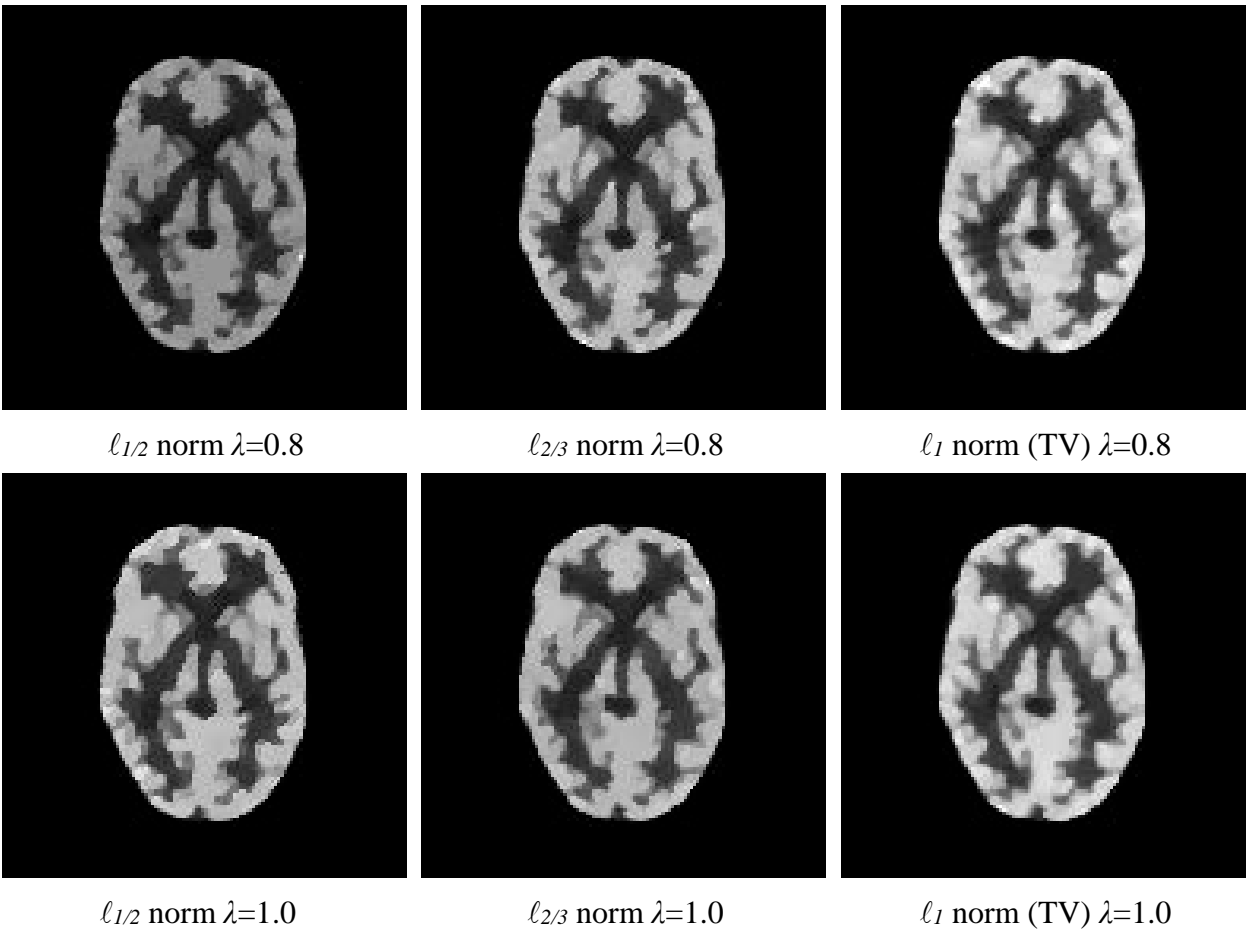


Fig. 4.24. Transaxial cross-section of Hoffman phantom reconstructed by PAPA with $\ell_{1/2}$ norm, $\ell_{2/3}$ norm, and ℓ_1 norm (TV).

4.5.5 Conclusions

Our preliminary experiments indicate that both fractional-norm regularizers perform similarly to TV in many respects. They suppress local spatial fluctuation very well, while maintaining good image contrast and sharp edges. However, the staircase artifacts are even more pronounced than TV-regularized reconstructions, and are more likely to show up as small piecewise-constant regions.

A potential application for fractional-norm regularization is in studies involving regions known, or likely to be piecewise constant.

Chapter 5. Conclusions and future work

In SPECT projection data, noise variance correlates negatively with patient dose and with imaging time. In order for lower patient dose with a given image acquisition time to be viable without sacrificing lesion detectability, we need to effectively suppress image noise during image reconstruction. Therefore, we have proposed and developed various novel regularization methods. To study the performance of the proposed methods, we used Monte Carlo simulations, and anonymized clinical data. Reconstructed images were analyzed with standard image quality measures including contrast-recovery coefficient, background variability, image bias, root-mean-squared error, and noise power spectra. In addition, we assessed the lesion conspicuity of reconstructed images with the signal-to-noise ratio of a channelized Hotelling observer. Several proposed regularizers are shown to be capable of suppressing noise while maintaining good spatial resolution and image contrast. Briefly, the main contributions of this dissertation are as follows:

- We introduced a high-order gradient into the regularization term in SPECT image reconstruction. While TV-PAPA outperformed GPF-EM, the clinical-standard image reconstruction method, in terms of contrast-noise tradeoff, spatial resolution, and CHO lesion detectability, it produced piecewise-constant artifacts, resulting in cartoon-like reconstructed images. Both proposed reconstruction methods—ICTV-PAPA and HOTV-PAPA—were shown to have the same noise-suppression, spatial resolution-preserving capability of TV-PAPA. Further, the

introduction of a high-order gradient in both methods greatly diminished staircase artifacts. The performance of ICTV-PAPA and HOTV-PAPA were very similar, even though the methodologies are very different.

- A DCT-induced framelet was proposed as a regularization term (DCT-PAPA), motivated by the sparsity of the framelet transform of natural smooth images. In our preliminary assessment, the reconstructed images had lower optimal MSE values compared with GPF-EM reconstructed images, meaning that, when penalty weight is selected properly, DCT-PAPA reconstructed images were closer to ground truth. Also, unlike a lot of penalized maximum likelihood reconstruction methods, the reconstructed images have minimal artifacts.
- We incorporated fractional norms of the first-order spatial gradient into the objective function of SPECT image reconstruction. Fractional-norm regularizers penalize low spatial-gradient values more than ℓ_1 norm (TV) does, and they penalize high spatial-gradient value less. Fractional norm-regularized reconstructions exhibit similarities to TV-regularized reconstructions.

Future work could be done in the following areas:

- Penalty-weight selection has great impact on image quality. It determines the spatial variation, spatial resolution, and contrast of the reconstructed images. Currently, there is no practical parameter-selection strategy other than trial-and-error. It should be possible to develop an adaptive parameter-selection strategy, based on certain image measures of the current image iteration.

- Infimal convolution of other types of convex functions could be implemented as regularization methods. The flexibility of fitting in image components with various features is important for avoiding image artifacts. A possible choice for the functions within the infimal convolution is the DCT-induced framelet decomposition of radiotracer-density estimation.
- Our current DCT-framelet regularization is done on transaxial cross-sections. To fully exploit the sparsity of high spatial-frequency components in the 3D reconstruction space, it may be possible to obtain better reconstructed images by expanding this regularization term to a 3D “volumelet.”
- One challenge for implementing DCT-framelet regularization is selection of penalty weights associated with various spatial-frequency components. It should be possible to select parameters locally, based on the current estimation of radiotracer density, in a similar fashion to [89].

Appendix A. Iteration scheme of TV-PAPA, HOTV-PAPA, and ICTV-PAPA

Table A.1 Pseudo-code of TV-PAPA

1. Set maximum iteration number N and regularization hyperparameter λ ;
2. Allocate memory for vectors: $f^{(0)}$, $h^{(0)}$, and $b^{(0)}$. Initialize $f^{(0)}=1$, $b^{(0)}=0$ (Note that b has 3 times the size of f), and set $\gamma=0.000001$, $K=10$;
3. Backproject 1 to reconstruction space, get $A^T I$;
4. **for** $n=0$ to $N-1$, **do**
 - EM step:
 5. calculate preconditioner $S=f^{(n)}/(A^T I)$
 6. backproject $g./(A f^{(n)} + \gamma)$ and get update $U=A^T[g./(A f^{(n)} + \gamma)]$
 7. $f^{(n+1/2)} = S.*U$
 - TV step
 8. update reconstruction parameters: $\beta=16* \lambda*max(S_i)$
 9. **for** $k = 1$ to K , **do**
 10. $h = f^{(n+1/2)} - \lambda/\beta\|B^T b\|_1.* S$;
 11. update b : $b = b + B h$

$$b = b - \max(b - \lambda\beta, 0)*b/\|b\|,$$
 12. $f^{(n+1)} = h - \lambda/\beta\|B^T b\|_1.* S$;
13. Return image estimate $f^{(N)}$.

Table A.2 Pseudo-code of HOTV-PAPA

1. Set maximum iteration number N and regularization hyperparameter λ ;
2. Allocate memory for four vectors: $f^{(0)}$, $h^{(0)}$, $b_1^{(0)}$, and $b_2^{(0)}$. Initialize $f^{(0)}=1$, $b_1^{(0)}=0$, $b_2^{(0)}=0$ (Note that b_1 has 3 times the size of f , and b_2 has 9 times the size of f), and set $\gamma=0.000001$, $K=10$;
3. Backproject 1 to reconstruction space, get $A^T I$;
4. **for** $n=0$ to $N-1$, **do**
 - EM step:
 5. calculate preconditioner $S=f^{(n)}/(A^T I)$
 6. backproject $g./(A f^{(n)} + \gamma)$ and get update $U=A^T[g./(A f^{(n)} + \gamma)]$
 7. $f^{(n+1/2)}=S.*U$
 - TV step
 8. update reconstruction parameters: $\beta_1=16*\lambda_1*\max(S_i)$, $\beta_2=64*\lambda_2*\max(S_i)$
 9. **for** $k=1$ to K , **do**
 10. $h=f^{(n+1/2)} - (\lambda_1/\beta_1\|B^T b_1\|_1 + \lambda_2/\beta_2\|B^T B b_2\|_1) .* S$;
 11. update b_1, b_2 : $b_1 = b_1 + B h$, $b_2 = b_2 - B^T B h$;

$$b_1 = b_1 - \max(b_1 - \lambda_1 \beta_1, 0) * b_1 / \|b_1\|,$$

$$b_2 = b_2 - \max(b_2 - \lambda_2 \beta_2, 0) * b_2 / \|b_2\|;$$
 12. $f^{(n+1)} = h - (\lambda_1/\beta_1\|B^T b_1\|_1 + \lambda_2/\beta_2\|B^T B b_2\|_1) .* S$;
13. Return image estimate $f^{(N)}$.

In ICTV, the regularizer can be formularized as:

$$\Phi(z) := \min(\lambda_1 \varphi_1(B_1 f_1) + \lambda_2 \varphi_2(B_2 f_2))$$

(A1)

where B_1 and B_2 denote first order TV, and second order discrete derivative, respectively.

$$\hat{f} = \operatorname{argmin}_{f \geq 0} \left\{ \langle Af, 1 \rangle - \langle \ln(Af + \gamma), g \rangle + \min(\lambda_1 \varphi_1(B_1 f_1) + \lambda_2 \varphi_2(B_2 f_2)) \right\} \quad (\text{A2})$$

Assuming both f_1 and f_2 are non-negative components of f , (17) becomes:

$$[\hat{f}_1, \hat{f}_2] = \operatorname{argmin}_{f_1 \geq 0, f_2 \geq 0} \left\{ \langle A(f_1 + f_2), 1 \rangle - \langle \ln(A(f_1 + f_2) + \gamma), g \rangle + \lambda_1 \varphi_1(B_1 f_1) + \lambda_2 \varphi_2(B_2 f_2) \right\} \quad (\text{A3})$$

Table A.3 Pseudo-code of ICTV-PAPA

1. Set maximum iteration number N and regularization

hyperparameter λ ;

2. Allocate memory for six vectors: $f_1^{(0)}, f_2^{(0)}, h_1^{(0)}, h_2^{(0)}, b_1^{(0)}$, and $b_2^{(0)}$. Initialize $f^{(0)}=1, b_1^{(0)}=0, b_2^{(0)}=0$ (Note that b_1 has 3 times the size of f , and b_2 has 9 times the size of f), and set $\gamma=0.000001, K=10$;

3. Backproject 1 to reconstruction space, get $A^T I$;

4. **for** $n=0$ to $N-1$, **do**

EM step:

5. calculate preconditioner $S_1=f_1^{(n)}/(A^T I), S_2=f_2^{(n)}/(A^T I)$;

6. backproject $g./(A f^{(n)} + \gamma)$ and get update $U=A^T [g./(A(f_1^{(n)} + f_2^{(n)}) + \gamma)]$;

7. $f_1^{(n+1/2)} = S_1.*U, f_2^{(n+1/2)} = S_2.*U$;

TV step

8. update reconstruction parameters: $\beta_1=16* \lambda_1*max(S_1)$,
 $\beta_2=64* \lambda_2*max(S_2)$
9. **for** $k = 1$ to K , **do**
10. $h_1 = f_1^{(n+1/2)} - \lambda_1/\beta_1\|B^T b_1\|_1 .* S_1$;
 $h_2 = f_2^{(n+1/2)} - \lambda_2/\beta_2\|B^T b_1\|_1 .* S_2$;
11. update b_1, b_2 : $b_1 = b_1 + B h$, $b_2 = b_2 - B^T B h$;
 $b_1 = b_1 - \max(b_1 - \lambda_1 \beta_1, 0) * b_1 / \|b_1\|$;
 $b_2 = b_2 - \max(b_2 - \lambda_2 \beta_2, 0) * b_2 / \|b_2\|$;
12. $f_1^{(n+1)} = h_1 - \lambda_1/\beta_1\|B^T b_1\|_1 .* S_1$,
 $f_2^{(n+1)} = h_2 - \lambda_2/\beta_2\|B^T B b_2\|_1 .* S_2$;
13. Return image estimate $f^{(N)} = f_1^{(N)} + f_2^{(N)}$.

Appendix B. Protocol for CDRF-modelling experiments

B.1. Preparation

14 line sources (10 cm length each): Fill 14 x 40 μ L micropipettes with with~300 μ Ci each of Tc-99m such that liquid fills 10 cm length of each. Record the time and exact activity of each of them. Place them in slots #1-7 and 15–21 of the phantom.

7 point sources (5 mm length each):Prepare 7 x 0.5” 40 μ L micropipettes and fill them with a ~300 μ Ci each of Tc-99m such that liquid fills 1 mm length of each. Record the time and exact activity of each of them. Place them in slots #8-14 of the phantom.

B.2. Experiment 1

Use e.cam LEHR parallel-hole (e.cam1).

Place the phantom directly on the collimator.

Align it with the center of the phantom.

Verify positioning using persistence scope.

Acquire planar image using head #1 in 512x512 matrix for 5 min.

Record start time, count rate and total number of counts.

Use clinical energy window size.

Save the image.

Repeat at 3 cm increments of the collimator-face-phantom-distance until you reach 40 cm. $d=0, 3, 6, 9, \dots, 40$ cm

B.3. Experiment 2

Use Triad LEUR fan-beam collimator.

Place the phantom directly on the collimator.

Align it with the center of the phantom.

Verify positioning using persistence scope.

Acquire planar image using head #1 in 512x512 matrix for 10 min.

Record start time, count rate and total number of counts.

Use clinical energy window size.

Save the image with ID: Krol triad 0 cm.

Repeat at 2 cm increments of the collimator-face-phantom-distance until you reach 40 cm. $d=0, 2, 4, 6, \dots, 40$ cm.

If 2 cm is not possible then start from the shortest possible distance.

Save the image with ID: Krol triad LEUR fan 2 cm, Krol triad LEUR fan 4 cm, etc.

Transfer images from both experiments to Hermes workstation.

Reference

- [1] G. Mariani, L. Bruselli, T. Kuwert, E. E. Kim, A. Flotats, O. Israel, *et al.*, "A review on the clinical uses of SPECT/CT," *European Journal of Nuclear Medicine and Molecular Imaging*, vol. 37, pp. 1959-1985, 2010// 2010.
- [2] M. Wernick and J. Aarsvold., "Emission Tomography: the Fundamentals of PET and SPECT," 2004.
- [3] H. O. Anger, "Scintillation Camera," *Review of Scientific Instruments*, vol. 29, pp. 27-33, 1958.
- [4] T. E. Peterson and L. R. Furenlid, "SPECT detectors: the Anger Camera and beyond," *Physics in Medicine and Biology*, vol. 56, p. R145, 2011.
- [5] K. Imagawa. (2005). *NaI Scintillation Detector*. Available: <http://www.horiba.com/us/en/publications/readout/article/nai-scintillation-detector-169/>
- [6] *Collimators for Nuclear Medicine*. Available: <http://www.nuclearfields.com/collimators-nuclear-medicine.htm>
- [7] G. T. Gullberg, G. L. Zeng, F. L. Datz, P. E. Christian, C. H. Tung, and H. T. Morgan, "Review of convergent beam tomography in single photon emission computed tomography," *Physics in Medicine and Biology*, vol. 37, p. 507, 1992.
- [8] J. Li, R. J. Jaszczak, T. G. Turkington, C. E. Metz, D. R. Gilland, K. L. Greer, *et al.*, "An evaluation of lesion detectability with cone-beam, fanbeam and parallel-beam collimation in SPECT by continuous ROC study," *J Nucl Med*, vol. 35, pp. 135-40, Jan 1994.
- [9] H. H. Barrett and K. J. Myers, *Foundations of Image Science*: Wiley-Interscience, 2004.
- [10] *Health Risks from Exposure to Low Levels of Ionizing Radiation: BEIR VII Phase 2*. Washington, DC: The National Academies Press, 2006.

- [11] *NCRP Report No. 160: Ionizing radiation exposure of the population of the United States.* Bethesda, MD: NCRP, 2009.
- [12] J. T. Bushberg, *The Essential Physics of Medical Imaging*: Lippincott Williams & Wilkins, 2002.
- [13] B. Hutton, I. Buvat, and F. J. Beekman, "Review and current status of SPECT scatter correction," *Physics in Medicine and Biology*, vol. 56, p. R85, 2011.
- [14] K. Ogawa, Y. Harata, T. Ichihara, A. Kubo, and S. Hashimoto, "A practical method for position-dependent Compton-scatter correction in single photon emission CT," *Medical Imaging, IEEE Transactions on*, vol. 10, pp. 408-412, 1991.
- [15] M. A. King, D. J. deVries, T. S. Pan, P. H. Pretorius, and J. A. Case, "An investigation of the filtering of TEW scatter estimates used to compensate for scatter with ordered subset reconstructions," *Nuclear Science, IEEE Transactions on*, vol. 44, pp. 1140-1145, 1997.
- [16] S. R. Meikle, B. F. Hutton, and D. L. Bailey, "A transmission-dependent method for scatter correction in SPECT," *J Nucl Med*, vol. 35, pp. 360-7, Feb 1994.
- [17] E. C. Frey and B. M. W. Tsui, "A new method for modeling the spatially-variant, object-dependent scatter response function in SPECT," in *Nuclear Science Symposium, 1996. Conference Record., 1996 IEEE*, 1996, pp. 1082-1086 vol.2.
- [18] J. W. Beck, R. J. Jaszczak, R. E. Coleman, C. F. Starmer, and L. W. Nolte, "Analysis of SPECT including Scatter and Attenuation Using Sophisticated Monte Carlo Modeling Methods," *Nuclear Science, IEEE Transactions on*, vol. 29, pp. 506-511, 1982.
- [19] F. J. Beekman, J. M. d. Harder, M. A. Viergever, and P. P. v. Rijk, "SPECT scatter modelling in non-uniform attenuating objects," *Physics in Medicine and Biology*, vol. 42, p. 1133, 1997.
- [20] H. R. Khosravi, S. Sarkar, A. Takavar, M. Saghari, and M. Shahriari, "Planar and SPECT Monte Carlo acceleration using a variance reduction technique in I131 imaging," *Internatuinal Journal of Radiation Research*, vol. 4, pp. 175-182, 2007.

- [21] A. C. Kak, M. Slaney, I. E. i. Medicine, and S. Biology, *Principles of computerized tomographic imaging*. New York: IEEE Press, 1988.
- [22] L. A. Shepp and Y. Vardi, "Maximum likelihood reconstruction for emission tomography," *IEEE Trans Med Imaging*, vol. 1, pp. 113-22, 1982.
- [23] K. Lange and R. Carson, "EM reconstruction algorithms for emission and transmission tomography," *J Comput Assist Tomogr*, vol. 8, pp. 306-16, Apr 1984.
- [24] A. P. Dempster, N. M. Laird, and D. B. Rubin, "Maximum Likelihood from Incomplete Data via the EM Algorithm," *Journal of the Royal Statistical Society. Series B (Methodological)*, vol. 39, pp. 1-38, 1977.
- [25] K. Lange, D. R. Hunter, and I. Yang, "Optimization Transfer Using Surrogate Objective Functions," *Journal of Computational and Graphical Statistics*, vol. 9, pp. 1-20, 2000.
- [26] H. M. Hudson and R. S. Larkin, "Accelerated image reconstruction using ordered subsets of projection data," *IEEE Trans Med Imaging*, vol. 13, pp. 601-9, 1994.
- [27] C. L. Byrne, "Accelerating the EMLL algorithm and related iterative algorithms by rescaled block-iterative methods," *Image Processing, IEEE Transactions on*, vol. 7, pp. 100-109, 1998.
- [28] S. Geman and D. Geman, "Stochastic Relaxation, Gibbs Distributions, and the Bayesian Restoration of Images," *Pattern Analysis and Machine Intelligence, IEEE Transactions on*, vol. PAMI-6, pp. 721-741, 1984.
- [29] S. Geman and D. MacClure, *Bayesian image analysis: an application to single photon emission tomography*. Alexandria, VA: American Statistical Association, 1985.
- [30] S. Kullback and R. A. Leibler, "On Information and Sufficiency," pp. 79-86, 1951/03 1951.
- [31] J. A. Fessler and W. L. Rogers, "Spatial resolution properties of penalized-likelihood image reconstruction: space-invariant tomographs," *IEEE Transactions on Image Processing*, vol. 5, pp. 1346-1358, 1996.

- [32] V. Y. Panin, G. L. Zeng, and G. T. Gullberg, "Total variation regulated EM algorithm [SPECT reconstruction]," *Nuclear Science, IEEE Transactions on*, vol. 46, pp. 2202-2210, 1999.
- [33] A. Sawatzky, C. Brune, F. Wubbeling, T. Kusters, K. Schafers, and M. Burger, "Accurate EM-TV algorithm in PET with low SNR," in *Nuclear Science Symposium Conference Record, 2008. NSS '08. IEEE*, 2008, pp. 5133-5137.
- [34] E. Jonsson, S.-c. Huang, and T. Chan, "Total-Variation Regularization in Positron Emission Tomography," *CAM Report 98-48, University of California, Los Angeles, CA, USA*, 1998.
- [35] J. M. Bardsley, "An efficient computational method for total variation-penalized Poisson likelihood estimation," *Inverse Problems and Imaging*, vol. 2, pp. 167-185, 2008.
- [36] J. M. Bardsley and J. Goldes, "Regularization parameter selection and an efficient algorithm for total variation-regularized positron emission tomography," *Numerical Algorithms*, vol. 57, pp. 255-271, 2011.
- [37] J. M. Bardsley and A. Luttmann, "Total variation-penalized Poisson likelihood estimation for ill-posed problems," *Advances in Computational Mathematics*, vol. 31, pp. 35-59, 2009.
- [38] S. Bonettini and V. Ruggiero, "An alternating extragradient method for total variation-based image restoration from Poisson data," *Inverse Problems*, vol. 27, p. 095001, 2011.
- [39] C. Chau, J.-C. Pesquet, and N. Pustelnik, "Nested iterative algorithms for convex constrained image recovery problems," *SIAM Journal on Imaging Sciences*, vol. 2, pp. 730-762, 2009.
- [40] E. Y. Sidky, J. H. Jørgensen, and X. Pan, "Convex optimization problem prototyping for image reconstruction in computed tomography with the Chambolle–Pock algorithm," *Physics in medicine and biology*, vol. 57, p. 3065, 2012.
- [41] A. Krol, S. Li, L. Shen, and Y. Xu, "Preconditioned Alternating Projection Algorithms for Maximum a Posteriori ECT Reconstruction," *Inverse Probl*, vol. 28, p. 115005, Nov 2012.

- [42] A. Krol, S. Li, Y. Xu, J. Zhang, L. O. Vogelsang, L. Shen, *et al.*, "Semi-dynamic preconditioned alternating projection MAP ECT reconstruction from low-dose ECT," 2013, pp. 86685F-86685F-6.
- [43] C. A. Micchelli, L. Shen, and Y. Xu, "Proximity algorithms for image models: denoising," *Inverse Problems*, vol. 27, p. 045009, 2011.
- [44] K. Lange, M. Bahn, and R. Little, "A Theoretical Study of Some Maximum Likelihood Algorithms for Emission and Transmission Tomography," *Medical Imaging, IEEE Transactions on*, vol. 6, pp. 106-114, 1987.
- [45] N. H. Clinthorne, T. S. Pan, P. C. Chiao, W. L. Rogers, and J. A. Stamos, "Preconditioning methods for improved convergence rates in iterative reconstructions," *Medical Imaging, IEEE Transactions on*, vol. 12, pp. 78-83, 1993.
- [46] P. J. Green, "Bayesian reconstructions from emission tomography data using a modified EM algorithm," *Medical Imaging, IEEE Transactions on*, vol. 9, pp. 84-93, 1990.
- [47] T. Lewellen, R. Harrison, and S. Vannoy, "The SimSET program," in *Monte Carlo Calculations in Nuclear Medicine*, ed Philadelphia: Institute of Physics Publishing, 1998, pp. 77-92.
- [48] M. Ljungberg, "SIMIND Monte Carlo based image reconstruction," *Journal of Nuclear Medicine*, vol. 56, p. 43, May 1, 2015 2015.
- [49] S. Jan, G. Santin, D. Strul, S. Staelens, K. Assié, D. Autret, *et al.*, "GATE: a simulation toolkit for PET and SPECT," *Physics in Medicine and Biology*, vol. 49, p. 4543, 2004.
- [50] M. Ljungberg, *The SIMIND Monte Carlo program*. Bristol and Philadelphia: IOP Publishing, 1998.
- [51] *ICRU Report 54: Medical imaging-the assessment of image quality*. Maryland, 1996.

- [52] D. W. Wilson, "Noise and resolution properties of FB and ML-EM reconstructed SPECT images," PhD, Department of Biomedical Engineering, University of North Carolina, 1994.
- [53] B. M. W. Tsui and E. C. Frey, *Collimator-Detector Response Compensation in SPECT. Quantitative Analysis in Nuclear Medicine Imaging*, New York: Springer, 2006.
- [54] A. Rahmim and J. Tang, "Noise propagation in resolution modeled PET imaging and its impact on detectability," *Physics in medicine & biology*, vol. 58, pp. 6945-68, 10/07 2013.
- [55] J. Baek and N. J. Pelc, "The noise power spectrum in CT with direct fan beam reconstruction," *Med Phys*, vol. 37, pp. 2074-81, May 2010.
- [56] J. Choi, "Measurement of noise power spectra for CT images reconstructed with different kernels," *Journal of Convergence Information Technology*, vol. 8, pp. 70-82, 2013.
- [57] S. Tong, A. M. Alessio, and P. E. Kinahan, "Noise and signal properties in PSF-based fully 3D PET image reconstruction: an experimental evaluation," *Physics in Medicine and Biology*, vol. 55, p. 1453, 2010.
- [58] Y. K. Dewaraja, M. Ljungberg, and J. A. Fessler, "3-D Monte Carlo-based scatter compensation in quantitative I-131 SPECT reconstruction," *Nuclear Science, IEEE Transactions on*, vol. 53, pp. 181-188, 2006.
- [59] H. B. Harrison, J. Yao, J. P. Rolland, and K. J. Myers, "Model Observers for Assessment of Image Quality," *Proceedings of the National Academy of Sciences of the United States of America*, vol. 90, pp. 9758-9765, 1993.
- [60] H. H. Barrett, J. L. Denny, R. F. Wagner, and K. J. Myers, "Objective assessment of image quality. II. Fisher information, Fourier crosstalk, and figures of merit for task performance," *Journal of the Optical Society of America A*, vol. 12, pp. 834-852, 1995/05/01 1995.
- [61] C. K. Abbey and H. H. Barrett, "Human- and model-observer performance in ramp-spectrum noise: effects of regularization and object variability," *Journal of the Optical Society of America A*, vol. 18, pp. 473-488, 2001/03/01 2001.

- [62] H. C. Gifford, M. A. King, D. J. de Vries, and E. J. Soares, "Channelized hotelling and human observer correlation for lesion detection in hepatic SPECT imaging," *J Nucl Med*, vol. 41, pp. 514-21, Mar 2000.
- [63] M. Shidahara, K. Inoue, M. Maruyama, H. Watabe, Y. Taki, R. Goto, *et al.*, "Predicting human performance by channelized Hotelling observer in discriminating between Alzheimer's dementia and controls using statistically processed brain perfusion SPECT," *Ann Nucl Med*, vol. 20, pp. 605-13, Nov 2006.
- [64] S. Leng, L. Yu, Y. Zhang, R. Carter, A. Y. Toledano, and C. H. McCollough, "Correlation between model observer and human observer performance in CT imaging when lesion location is uncertain," *Med Phys*, vol. 40, p. 081908, Aug 2013.
- [65] K. Li, J. Garrett, and G. H. Chen, "Correlation between human observer performance and model observer performance in differential phase contrast CT," *Med Phys*, vol. 40, p. 111905, Nov 2013.
- [66] H. R. Wilson and J. R. Bergen, "A four mechanism model for threshold spatial vision," *Vision Research*, vol. 19, pp. 19-32, 1979/01/01 1979.
- [67] H. R. Wilson and S. C. Giese, "Threshold visibility of frequency gradient patterns," *Vision Research*, vol. 17, pp. 1177-1190, // 1977.
- [68] C. K. Abbey, H. H. Barrett, and M. P. Eckstein, "Practical issues and methodology in assessment of image quality using model observers," 1997, pp. 182-194.
- [69] E. Levitan and G. T. Herman, "A Maximum a Posteriori Probability Expectation Maximization Algorithm for Image Reconstruction in Emission Tomography," *Medical Imaging, IEEE Transactions on*, vol. 6, pp. 185-192, 1987.
- [70] R. H. Huesman, G. J. Klein, W. W. Moses, Q. Jinyi, B. W. Reutter, and P. R. G. Virador, "List-mode maximum-likelihood reconstruction applied to positron emission mammography (PEM) with irregular sampling," *Medical Imaging, IEEE Transactions on*, vol. 19, pp. 532-537, 2000.

- [71] G. T. Gullberg, "Entropy and transverse section reconstruction," *International Journal of Nuclear Medicine and Biology*, vol. 3, pp. 170-171, 10// 1976.
- [72] N. V. Denisova, "Bayesian reconstruction in SPECT with entropy prior and iterative statistical regularization," *Nuclear Science, IEEE Transactions on*, vol. 51, pp. 136-141, 2004.
- [73] D. S. Lalush, E. C. Frey, and B. M. W. Tsui, "Fast maximum entropy approximation in SPECT using the RBI-MAP algorithm," in *Nuclear Science Symposium, 1998. Conference Record. 1998 IEEE*, 1998, pp. 1157-1164 vol.2.
- [74] L. I. Rudin, S. Osher, and E. Fatemi, "Nonlinear total variation based noise removal algorithms," *Physica D: Nonlinear Phenomena*, vol. 60, pp. 259-268, 11/1/ 1992.
- [75] J. A. Fessler: SPIE-The International Society for Optical Engineering, 1997.
- [76] Y. Lu, A. Krol, L. Vogelsang, B. Yu, Y. Xu, and D. Feiglin, "Total variation and Huber prior regularization for OSEM SPECT reconstruction in mesh domain," *J NUCL MED MEETING ABSTRACTS*, vol. 50, pp. 403-, May 1, 2009 2009.
- [77] M. Benning, C. Brune, M. Burger, and J. Müller, "Higher-Order TV Methods—Enhancement via Bregman Iteration," *Journal of Scientific Computing*, vol. 54, pp. 269-310, 2013/02/01 2013.
- [78] T. Chan, A. Marquina, and P. Mulet, "High-Order Total Variation-Based Image Restoration," *SIAM Journal on Scientific Computing*, vol. 22, pp. 503-14, 2000 2012-06-29 2000.
- [79] S. Li, J. Zhang, A. Krol, C. R. Schmidlein, L. Vogelsang, L. Shen, *et al.*, "Effective noise-suppressed and artifact-reduced reconstruction of SPECT data using a preconditioned alternating projection algorithm," *Medical Physics*, vol. 42, pp. 4872-4887, 2015.
- [80] A. Chambolle and P.-L. Lions, "Image recovery via total variation minimization and related problems," *Numerische Mathematik*, vol. 76, pp. 167-188, 1997/04/01 1997.

- [81] J. Zhang, S. Li, E. Lipson, C. R. Schmidtlein, D. Feiglin, Y. Xu, *et al.*, "Image Quality Comparison of Reconstruction Using Total Variation-Based Regularizers," in *IEEE Nuclear Science Symposium & Medical Imaging Conference*, Seattle, 2014.
- [82] B. S. Greenspan, G. Dillehay, C. Intenzo, W. C. Lavelly, M. O'Doherty, C. J. Palestro, *et al.*, "SNM Practice Guideline for Parathyroid Scintigraphy 4.0," *Journal of Nuclear Medicine Technology*, vol. 40, pp. 111-118, June 1, 2012 2012.
- [83] D. Dey, P. J. Slomka, L. J. Hahn, and R. Kloiber, "Comparison of ordered subsets expectation maximization and Chang's attenuation correction method in quantitative cardiac SPET: a phantom study," *Nucl Med Commun*, vol. 19, pp. 1149-57, Dec 1998.
- [84] T. Kauppinen, M. O. Koskinen, S. Alenius, E. Vanninen, and J. T. Kuikka, "Improvement of brain perfusion SPET using iterative reconstruction with scatter and non-uniform attenuation correction," *Eur J Nucl Med*, vol. 27, pp. 1380-6, Sep 2000.
- [85] R. H. Chan, S. D. Riemenschneider, L. Shen, and Z. Shen, "Tight frame: an efficient way for high-resolution image reconstruction," *Applied and Computational Harmonic Analysis*, vol. 17, pp. 91-115, 7// 2004.
- [86] J.-F. Cai, R. H. Chan, and Z. Shen, "A framelet-based image inpainting algorithm," *Applied and Computational Harmonic Analysis*, vol. 24, pp. 131-149, 3// 2008.
- [87] R. H. Chan, Z. Shen, and T. Xia, "A framelet algorithm for enhancing video stills," *Applied and Computational Harmonic Analysis*, vol. 23, pp. 153-170, 9// 2007.
- [88] L. Yan-Ran, S. Lixin, D. Dao-Qing, and B. W. Suter, "Framelet Algorithms for De-Blurring Images Corrupted by Impulse Plus Gaussian Noise," *Image Processing, IEEE Transactions on*, vol. 20, pp. 1822-1837, 2011.
- [89] Y. R. Li, L. Shen, and B. W. Suter, "Adaptive inpainting algorithm based on DCT induced wavelet regularization," *IEEE Trans Image Process*, vol. 22, pp. 752-63, Feb 2013.
- [90] J. Zhang, S. Li, Y. Xu, C. R. Schmidtlein, E. D. Lipson, D. H. Feiglin, *et al.*, "SPECT reconstruction using DCT-induced tight framelet regularization," 2015, pp. 94123H-94123H-6.

- [91] N. Ahmed, T. Natarajan, and K. R. Rao, "Discrete Cosine Transform," *Computers, IEEE Transactions on*, vol. C-23, pp. 90-93, 1974.
- [92] N. Ahmed and K. R. Rao, *Orthogonal Transforms for Digital Signal Processing*. New York: Springer-Verlag, 1975.
- [93] W. Cao, J. Sun, and Z. Xu, "Fast image deconvolution using closed-form thresholding formulas of regularization," *Journal of visual communication and image representation*, vol. 24, pp. 31-41, 01/2013.

VITA

NAME OF AUTHOR: Jiahan Zhang

PLACE OF BIRTH: Daxing'anling, Heilongjiang, China

DATE OF BIRTH: August 24, 1988

GRADUATE AND UNDERGRADUATE SCHOOLS ATTENDED:

Syracuse University, Syracuse, NY, USA

Nankai University, Tianjin, China

DEGREE AWARDED:

Bachelor of Science in Physics, 2011, Nankai University

AWARDS:

Syracuse University Fellowship 2013-2014, 2011-2012

Henry Levinstein Fellowship 2013, 2012

National Scholarship for Encouragement (China) 2010

PROFESSIONAL EXPERIENCE:

Teaching Assistant, Department of Physics, Syracuse University, 2012-2013, 2014-2016